MAX PLANCK INSTITUTE FOR POLYMER RESEARCH
JOHANNES GUTENBERG-UNIVERSITÄT MAINZ

Optimizing organic light-emitting diode performance through molecular engineering

Dissertation
Zur Erlangung des Grades
“Doktor der Naturwissenschaften”
am Fachbereich Chemie, Pharmazie und Geowissenschaften der
Johannes Gutenberg-Universität
in Kooperation mit dem
Max-Planck-Institut für Polymerforschung
in Mainz

Oskar Sachnik

Geboren in Schongau, Deutschland
Mainz, 2024

1. Berichterstatter: Prof. Dr. Paul Blom, Max Planck Institut für Polymerforschung, Mainz

2. Berichterstatterin: Prof. Dr. Katja Heinze, Johannes Gutenberg-Universität Mainz

3. Berichterstatter: Prof. Dr. Wolfgang Brütting, Universität Augsburg

Tag der mündlichen Prüfung: 17.12.2024

Die vorliegende Arbeit wurde in der Zeit von Dezember 2019 bis November 2023 am Max-Planck-Institut für Polymerforschung in Mainz unter der Betreuung von Prof. Dr. Paul W.M. Blom durchgeführt.

Affidavit

I hereby declare that I completed the dissertation independently and without any external support. Except for the places mentioned and referenced in the thesis, no external sources were used.

Furthermore, I confirm that this thesis has not yet been submitted as part of another examination process neither in identical nor in similar form.

Ort, Datum: Unterschrift:

Abstract

Organic light-emitting diodes (OLEDs) represent an important display technology, which offer clear advantages over established display technologies such as reduced energy consumption, easy fabrication, fast response times and perfect blacks. Nevertheless, state-of-the-art OLEDs can be still optimized in terms of lifetime, efficiency and simplicity. Most commercial products require a multi-layer device architecture to enable efficient light-generation. One of the most crucial factors for efficient light-generation is efficient charge-transport within the employed organic emissive layer. This often overlooked factor can have tremendous influence on the resulting efficiency. Most organic semiconductors experience unipolar charge transport, being either hole- or electron-transport dominated. This unipolarity in charge-transport is caused due to charge trapping of either electrons or holes. Especially blue light-emitting organic semiconductors suffer from this phenomenon.

This thesis addresses this issue in chapter 2, by presenting a novel molecular strategy where the HOMO and LUMO are spatially separated within the molecule. By carefully tuning the chemical structure and molecular stacking, the electron-transporting LUMO is protected from extrinsic impurities, thereby enhancing electron current by orders of magnitude and enabling trap-free hole and electron transport at the same time. This advancement opens a pathway toward developing large band gap organic semiconductors with balanced charge transport for efficient blue OLEDs.

In general, commercial OLEDs consist of a multilayer stack incorporating several charge-transport and exciton-blocking layers to confine excitons within the emissive layer. With this device architecture, usually external quantum efficiencies of ~30% are achieved. However, in chapter 3 it is demonstrated that a simplified and highly efficient single-layer blue-emitting OLED based on thermally activated delayed fluorescence (TADF) is possible, rivalling current multilayer structures. The key to this achievement is the balanced charge transport within the emissive layer and the use of an ohmic polymeric anode. The polymeric anode, based on PEDOT:PSS, is modified to create a hole-contact with a high work function of up to 5.9 eV, rendering it practically barrier-free for various organic semiconductors.

In chapter 2, the organic semiconductor 3CzTRZ is identified as a promising candidate for single-layer blue OLEDs due to its large band gap (~3.0 eV) and TADF properties. Despite these advantages, neat films of 3CzTRZ exhibit a low photoluminescence quantum yield (PLQY) of only 40%, attributed to a fast intersystem crossing rate and slow reverse intersystem crossing. Time-resolved photoluminescence measurements reveal that incorporating 3CzTRZ into a large band gap host material significantly increases the triplet lifetime, enhancing the PLQY and boosting the external quantum efficiency (EQE) to 15%. These results demonstrate, that despite having excellent charge-transport properties and TADF properties, a limited device performance is achieved. Enhancing the triplet-lifetime by doping the emissive material in a suitable host-material can be a viable solution for higher efficiencies.

Further studies show that 3CzTRZ, due to its superior charge-transport properties, can be used as a large band gap host for other organic emitters. For instance, when used in combination with the green-

emitting DMAC-BP, which has a strongly trap-limited electron current, 3CzTRZ assists in electron transport, improving it by several orders of magnitude. This results in balanced charge transport within a single semiconducting layer, yielding an EQE of 19.6% in a simplified single-layer architecture. Additionally, the resulting OLED demonstrates almost 40% higher power efficiency and longer lifetimes compared to other reported devices, thus offering a viable alternative to conventional multilayer structures. This research contributes to the development of efficient, simplified, and long-lasting organic light-emitting diodes.

Zusammenfassung

Organische Leuchtdioden (OLEDs) stellen eine bedeutende Displaytechnologie dar, die klare Vorteile gegenüber etablierten Displaytechnologien bietet, wie z. B. einen geringeren Energieverbrauch, einfache Herstellung, schnelle Reaktionszeiten und perfekte Schwarzwerte. Dennoch können moderne OLEDs in Bezug auf Lebensdauer, Effizienz und Einfachheit weiter optimiert werden. Die meisten kommerziellen Produkte erfordern eine Mehrschicht-Architektur, um eine effiziente Lichtemission zu ermöglichen. Einer der wichtigsten Faktoren für eine effiziente Lichtemission ist der effiziente Ladungstransport innerhalb der verwendeten organischen Emitterschicht. Dieser oft übersehene Faktor kann einen enormen Einfluss auf die resultierende Effizienz haben. Die meisten organischen Halbleiter weisen einen unipolaren Ladungstransport auf, der entweder von Loch- oder Elektronentransport dominiert wird. Diese Unipolarität im Ladungstransport wird durch das Einfangen (*charge-trapping*) von Elektronen oder Löchern verursacht. Besonders blaue lichtemittierende organische Halbleiter leiden unter diesem Phänomen.

Dieses Problem wird in Kapitel 2 dieser Arbeit behandelt, indem eine neuartige molekulare Strategie vorgestellt wird, bei der HOMO und LUMO räumlich innerhalb des Moleküls getrennt sind. Durch sorgfältige Abstimmung der chemischen Struktur und des molekularen *Stackings* wird das elektronentransportierende LUMO vor äußeren Verunreinigungen geschützt. Hierdurch kann der Elektronenstrom um mehrere Größenordnungen verbessert und ein fallenfreier (*trap-free*) Loch- und Elektronentransport ermöglicht werden. Diese Weiterentwicklung eröffnet den Weg zur Entwicklung organischer Halbleiter mit großer Bandlücke und ausgeglichenem Ladungstransport für effiziente blaue OLEDs.

Kommerzielle OLEDs basieren im Allgemeinen auf einer Mehrschicht-Architektur, welche mehrere Ladungstransport- und Exziton-Blockierungsschichten integriert, um Exzitonen innerhalb der Emitterschicht zu halten. Mit dieser Architektur werden üblicherweise externe Quantenausbeuten von ~30% erreicht. In Kapitel 3 wird jedoch gezeigt, dass eine vereinfachte und hocheffiziente einschichtige (*single-layer*) blaue OLED auf Basis thermisch aktivierter verzögerter Fluoreszenz (TADF) möglich ist, die mit aktuellen OLEDs, welche aus mehreren aufgedampften Schichten bestehen, konkurrieren kann. Der Schlüssel zum Erfolg liegt im ausgeglichenen Ladungstransport innerhalb der Emitterschicht und der Verwendung einer ohmschen polymeren Anode. Die polymere Anode, basierend auf PEDOT:PSS, wird modifiziert, um einen Lochkontakt mit einer hohen Austrittsarbeit von bis zu 5.9 eV zu schaffen, wodurch sie für verschiedene organische Halbleiter praktisch barrierefrei ist.

In Kapitel 2 wird der organische Halbleiter 3CzTRZ als vielversprechender Kandidat für einschichtige blaue OLEDs aufgrund seines großen Bandabstands (~3.0 eV) und seiner TADF-Eigenschaften identifiziert. Trotz dieser Vorteile weisen reine Filme von 3CzTRZ eine niedrige photolumineszente Quantenausbeute (PLQY) von nur 40% auf, was auf eine schnelle Intersystem-Crossing-Rate und langsame Reverse-Intersystem-Crossing-Rate zurückzuführen ist. Diese Ergebnisse zeigen, dass trotz hervorragender Ladungstransport- und TADF-Eigenschaften nur begrenzte Effizienzen in einer OLED

erreicht werden. Zeitaufgelöste Photolumineszenzmessungen in Kaptiel 4 zeigen, dass die Einbindung von 3CzTRZ in ein Host-Material mit größerer Bandlücke die Triplettlebensdauer signifikant erhöht, die PLQY steigert und die externe Quanteneffizienz (EQE) auf 15% verbessert. Die Erhöhung der Triplettlebensdauer durch Dotierung des Emitters in ein geeignetes Host-Material kann daher eine tragfähige Lösung für höhere Effizienzen sein.

Abschließende Untersuchungen in Kapitel 5 zeigen, dass 3CzTRZ aufgrund seiner überlegenen Ladungstransporteigenschaften als Host-Material mit großer Bandlücke für andere organische Emitter mit kleinerer Bandlücke verwendet werden kann. Wenn es beispielsweise in Kombination mit dem grün emittierenden DMAC-BP verwendet wird, das einen *trap*-limitierten Elektronenstrom aufweist, unterstützt 3CzTRZ den Elektronentransport und verbessert ihn um mehrere Größenordnungen. Dies führt zu einem ausgeglichenen Ladungstransport innerhalb einer einzigen Halbleiterschicht und ergibt eine externe Quantenausbeute von 19.6% in einer vereinfachten einschichtigen OLED. Darüber hinaus zeigt die resultierende OLED eine um fast 40% höhere Energieeffizienz und längere Lebensdauer im Vergleich zu anderen berichteten Mehrschicht-OLEDs. Dieses Ergebnis trägt deshalb zur Entwicklung effizienter, vereinfachter und langlebiger organischer Leuchtdioden bei.

Contents

1. Introduction 1
1.1 Organic light emitting diodes 1
1.2 Organic semiconductors 2
1.3 Quantum numbers and radiative transitions 6
1.4 Thermally activated delayed fluorescence 8
1.4.1 Design strategies of TADF materials 8
1.4.2 Quantitative and qualitative measurements of TADF 11
1.5 Light-generating processes in OLEDs 13
1.6 Energetic levels in organic semiconductors 14
1.7 Operation of single carrier devices 15
1.7.1 Device layout of single carrier devices 15
1.7.2 Current-voltage characteristics of single carrier devices during operation 16
1.7.3 Charge-Trapping in organic semiconductors 17
1.8 Operation of organic light-emitting diodes 18
1.8.1 Device layout of organic light-emitting diodes 18
1.8.2 Current-voltage characteristics of OLEDs during operation 20
1.8.3 Performance Characterization of OLEDs 21
1.9 Scope and outline 22

2. Suppression of charge-carrier trapping by molecular design 27
2.1 Introduction 28
2.2 Results and Discussion 29
2.3 Conclusion 36

3. Blue single-layer organic light-emitting diodes with near-unity internal efficiency 39
3.1 Introduction 40
3.2 Results and Discussion 42
3.3 Conclusion 47

4. Reduction of non-radiative losses in trap-free organic light-emitting diodes 51
4.1 Introduction 52
4.2 Results and Discussion 54
4.3 Conclusion 62

5. Trap-free host for single-layer organic light-emitting diodes 65
5.1 Introduction 66
5.2 Results and Discussion 68
5.3 Conclusion 74

6. Summary 77

7. Experimental methods **79**
7.1 Device fabrication 79
7.1.1 Device cleaning 79
7.1.2 PEDOT:PSS modification 79
7.1.3 Device fabrication 79
7.1.4 Device measurement 81
7.2 NMR measurements 81
7.2.1 Solution NMR 81
7.2.2 Solid-state NMR 81
7.3 Determination of energy levels 81
7.3.1 Photoelectron Spectroscopy 81
7.3.2 Cyclic Voltammetry (CV) 82
7.4 Mass spectrometry 82
7.5 Spectroscopy 82
7.5.1 Photoluminescence spectroscopy 82
7.5.2 UV-Vis absorption spectroscopy 82
7.5.3 Photoluminescence quantum yield (PLQY) 82
7.6 Commercial materials 83
7.7 Synthesis 84
7.7.1 Introduction of carbazole in fluorobenzenes 84
7.8.2 Formation of boronic acid pinacol esters by Suzuki-coupling 86
7.8.3 Formation of triazine-carbazole based compounds by Suzuki-coupling 88
7.8.4 Formation of triazine containing fluorobenzenes 92
7.8.5 Introduction of carbazole in triazine containing fluorobenzenes 93
7.8.6 Preperation of SpiroAc-TRZ 95

Appendix Chapter 2 ..... **96**
Appendix Chapter 3 ..... **104**
Appendix Chapter 4 ..... **113**
Appendix Chapter 5 ..... **116**

List of Publications **119**
Acknowledgements **120**

1. Introduction

This chapter is dedicated to introduce the reader to the working principle of organic light-emitting diodes and the employed organic semiconductors. This chapter will provide knowledge about important properties of organic semiconductors such as charge transport and light-generation and will assist to understand following chapters in this thesis.

1.1 Organic light emitting diodes

Electronic displays are nowadays more important than ever: Personal computers, televisions, smartphones, augmented and virtual reality glasses and various other electronic devices rely on electronic displays. Cathode-Ray displays have been the dominant display type from their development in the 1930s until late 1990s. The rise of mobile applications made light, small-sized and efficient displays a necessity. In recent years, organic light-emitting diodes (OLEDs) have emerged as one of the most promising display technologies, offering perfect blacks with infinite contrast, fast response times and low power consumption. Even though a widespread commercialization of OLEDs was observed in early 2010s, the foundation was laid almost 50 years prior by *Pope et. al.* in 1963 by fabricating the first working OLED based on anthracene as light-emitting material.[1] In 1987, the first working device operating at low voltages was demonstrated by Tang and VanSlyke.[2] Further stability and performance improvements in the following decades lead to OLEDs competing with established display technologies such as Liquid crystal displays (LCDs). LCDs require a white light-emitting back panel, typically based on crystalline inorganic semiconductors such as GaN or InGaN.[3,4] This back panel is used to direct light through the liquid crystals, which are responsible for the final color impression. In comparison to OLED displays, where pixels can be individually switched on and off, the permanently turned on back panel in LCDs renders them less efficient and results in non-perfect blacks. MicroLED is an emerging display technology, which is believed to compete with OLEDs in the coming future. Here, individual pixels are based on inorganic semiconductors. Despite being similar to OLED, fabricating whole display panels based on inorganic semiconductors is tremendously more challenging. Inorganic semiconductors require epitaxial growth on wafers, which need to be cut into individual pixels and subsequently sorted. Thus, for a 1080p RGB resolution display, almost 6.2 million pixels (3×1080×1920) need to be sorted and put together. In contrast, organic materials can be either directly evaporated through shadow masks or inkjet-printed, which demonstrates a significantly less cumbersome production process. Although offering clear advantages over existing technologies,

OLEDs can be still optimized in terms of lifetime and efficiency, which requires to understand their fundamental working principle and which is something discussed in the following chapters.

1.2 Organic semiconductors

In stark contrast to inorganic crystalline semiconductors, where atoms are arranged in an ordered fashion and electrons are delocalized over the entire lattice, organic semiconductors are composed of individual molecules and are held together by weak van der Waals forces.[5,6] Organic semiconductors are typically carbon-based materials, which often incorporate elements such as nitrogen (N), oxygen (O), boron (B) and sulfur (S) into their structures.[7–9] The semiconducting properties of organic materials stem from their electronic conjugation, which involves the overlap of adjacent p-orbitals, allowing electrons to be delocalized within a molecule. Elemental carbon possesses an electronic configuration of $1s^2 2s^2 2p^2$, with two p-orbitals of equal energy. Through hybridization (**Figure 1.1**), where atomic orbitals of similar energies mix (such as 2s and 2p), carbon forms chemical bonds of equal character. Hybridization results in a temporarily higher energy but reduces the overall energy of the resulting chemical bond.

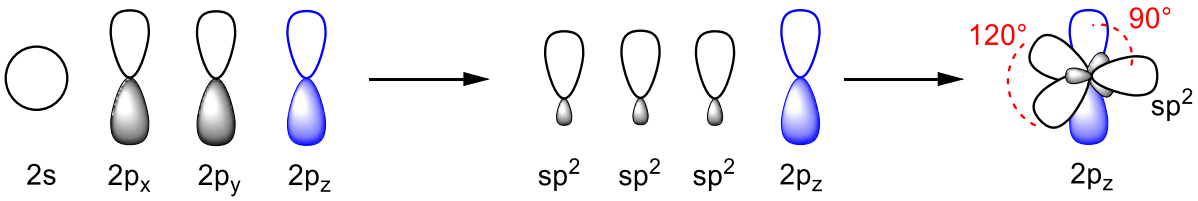

Figure 1.1. sp^2-Hybridization of carbon.

Ethylene represents the most simple conjugated molecular system, comprising two bonded carbon atoms with two hydrogen atoms attached to each carbon. In ethylene, both carbon atoms undergo hybridization, where the 2s-orbital and three 2p-orbitals of each carbon atom mix, resulting in three hybridized sp^2-orbitals and one non-hybridized p_z-orbital. The sp^2-orbitals adopt a trigonal planar geometry with 120° angles, while the remaining p_z-orbital resides perpendicular to the plane formed by the sp^2-orbitals. A σ-bond is created along the internuclear carbon-carbon axis through the head-to-head overlap of two sp^2-orbitals, as depicted in **Figure 1.2**.[10] Additionally a π-bond is formed between the carbon atoms via the side-by-side overlap of their p_z-orbitals, resulting in the familiar carbon-carbon double bond. The remaining sp^2-orbitals of each carbon atom overlap with the 1s-orbitals of the four neighboring hydrogen atoms, leading to the formation of four additional σ-bonds in ethylene.

According to molecular orbital theory, the number of atomic orbitals prior to chemical bond formation has to be equal to the number of molecular orbitals post-bond formation. Therefore, for every bonding

molecular orbital, an anti-bonding counterpart is created. Anti-bonding molecular orbitals have no constructive overlap of the atomic wavefunctions. Occupied by an electron, these orbitals destabilize the chemical bond, which elevates their energy compared to bonding orbitals (**Figure 1.2a**).[10] Anti-bonding σ- and π-orbitals are commonly referred to as σ*- and π*-orbitals, respectively (**Figure 1.2b**).

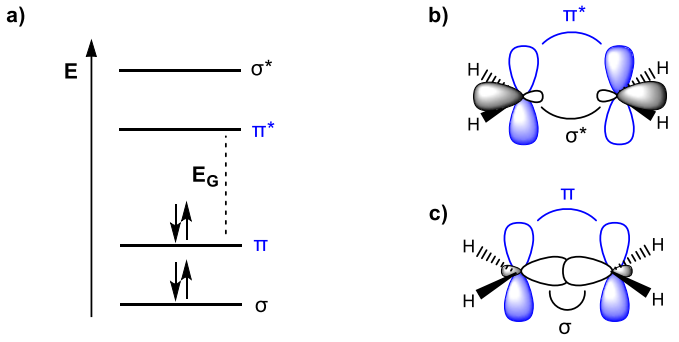

Figure 1.2. Molecular orbitals and energy levels in ethylene. The energetic distribution of molecular levels a), the anti-bonding orbitals b) and bonding orbitals c).[10]

In the ground state, bonding molecular orbitals are occupied, whereas anti-bonding orbitals remain completely empty. As illustrated in **Figure 1.2c**, the overlap of both p_z-orbitals generates a node along the carbon-carbon plane in the ethylene molecule. Consequently, bonding π-orbitals exhibit higher energies than bonding σ-orbitals, making them the highest occupied molecular orbital (HOMO) in conjugated systems. The energetic gap between π-/π*-orbitals is narrower than the splitting between σ-/σ*-orbitals. This discrepancy arises from the more pronounced overlap in σ-bonds compared to π-bonds, resulting in a higher exchange energy of electrons in the overlapping sp^2-orbitals. For this reason, π*-orbitals resemble the lowest unoccupied molecular orbital (LUMO) in conjugated molecules. The HOMO and LUMO are, respectively, comparable to the valence band (VB) and conduction band (CB) in inorganic semiconductors.

Extending the number of connected sp^2-carbon atoms to four, as seen in 1,3-Butadiene (**Figure 1.3**), leads to an extension of the conjugated system. In butadiene, the combination of four p_z-orbitals results in the formation of four molecular orbitals with varying energies. This variance is due to a differing number of nodes, which emerges from overlapping the four p_z-orbitals in different ways. The four electrons are distributed over the two lowest lying states, resulting in two bonding- and two anti-bonding molecular orbitals, where the highest bonding molecular orbital resembles the HOMO and the lowest lying anti-bonding molecular orbital constitutes the LUMO.

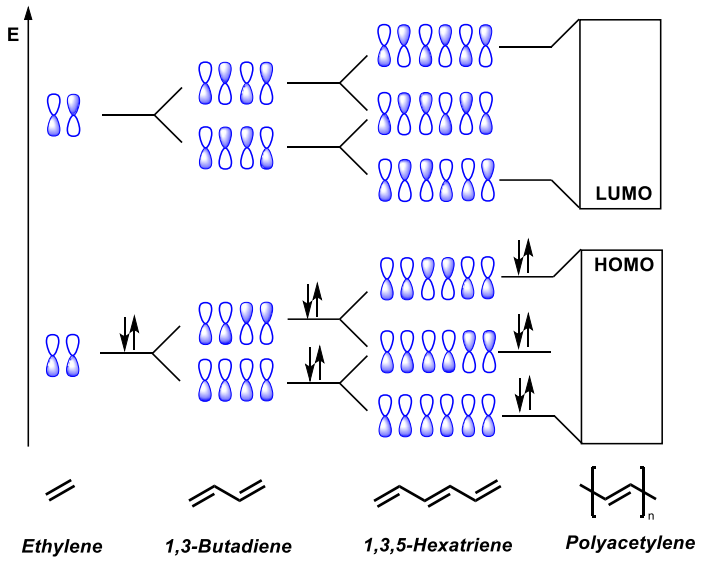

Figure 1.3. Bandgap reduction in organic semiconductors by extension of the π-conjugation.

In 1,3-Butadiene, both bonding molecular orbitals possess in total a lower energy than two individual bonding molecular orbitals from two separate ethylene molecules. This characteristic makes 1,3-Butadiene thermodynamically more stable and results in a smaller energy gap (E_G) between HOMO and LUMO. Expanding the chain of connected carbon atoms, leads to a further elevation of the HOMO level and reduction of the LUMO level. Consequently, the energy gap between HOMO (π) and LUMO (π^*) can be tuned by the size of the conjugated system. The promotion of an electron from π to π^* followed by relaxation resembles the fundamental principle for light generation. By tuning the energetic bandgap, organic semiconductors enable light emission in the visible range, typically in the range 1.5 – 3.0 eV (deep red to blue).

Most organic semiconductors are based on aromatic compounds, which absorb light in the ultraviolet region and produce fluorescence in the visible region. In **Figure 1.4**, a range of exemplary organic semiconductors is displayed, which are accessible through chemical synthesis.[11–13] These materials span from purely carbon based compounds such as Rubrene to those incorporating transition metals such as $Ir(ppy)_3$.[11,12] Both structures belong to the class of so-called *small molecule* organic semiconductors.

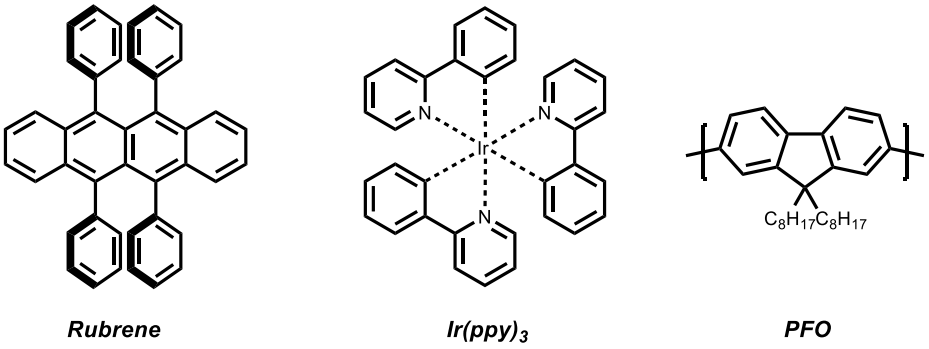

Figure 1.4. Exemplary organic semiconductors. Purely organic (Rubrene, 5,6,11,12-Tetraphenylnaphthacene), with incorporated metals ($Ir(ppy)_3$, Tris(2-phenylpyridine)iridium(III) and polymers (PFO, Poly(9,9-di-*n*-octylfluorenyl-2,7-diyl)).

Another important class of organic semiconductors comprises polymeric structures, known as *semiconducting polymers*, which consist of repeating units with a conjugated backbone. Their flexibility and tunable properties make them attractive for flexible electronics and wearable devices.[14,15] Despite their advantageous characteristics, challenges remain in improving their stability and performance.

Aromatic compounds offer a variety of possibilities for chemical modification, particularly through aromatic substitution and cross-coupling reactions. Aromatic substitution reactions can be generally categorized as electrophilic and nucleophilic type (**Figure 1.5**).[16–18] Electrophilic aromatic substitutions involve the replacement of an atom within an aromatic system by an electrophile, which happens due to the nucleophilic "attack" of the π-electrons of the aromatic system at an electrophile (**Figure 1.5a**). Important examples include the halogenation, sulfonation, nitration, alkylation and acylation of aromatic compounds. Nucleophilic aromatic substitution is a related reaction where the aromatic system is attacked by a nucleophile, displacing a leaving group.

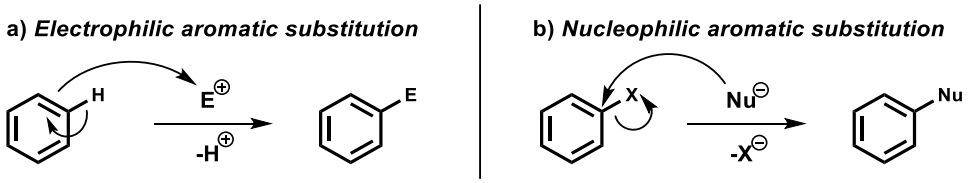

Figure 1.5. Aromatic substitution reactions. Electrophilic (a) and nucleophilic (b) type.

Nucleophilic aromatic substitution (**Figure 1.5b**) is particularly effective when electron withdrawing groups that are attached to the aromatic system enhance its electrophilic character. The leaving group is equally crucial, as the rate-limiting step in nucleophilic aromatic substitution is the nucleophile's

attack and replacement of the leaving group, leading to the restoration of aromaticity.[18] This is particularly true for leaving groups that polarize the carbon-bond, such as fluoride, which represents an excellent leaving group, exhibiting the highest electronegativity and creating a polarized bond.

Cross-coupling reactions represent another important type of reaction for formation of carbon-carbon bonds and carbon-heteroatom bonds. These reactions typically require a transition metal catalyst M, an organic compound with designated leaving group R^1X (X = typically halogen) and an organometallic species R^2-B. Most cross-coupling reactions use Palladium (Pd), Platinum (Pt) or Nickel (Ni) as metal catalyst. Depending on the specific cross-coupling type, different organometallics are utilized, such as R-Zn-X (Negishi), R-SnR_3 (Stille) or R-BOR_2 (Suzuki).[19–21] Cross coupling reactions follow a generally similar mechanism, proceeding via oxidative addition, trans-metalation and reductive elimination steps (**Figure 1.6**). Oxidative addition describes the insertion of the metal catalyst M into the carbon-halogen bond, changing the oxidation state of the catalyst from 0 to +II. Subsequently, the halogen atom is exchanged by the organic group of the organometallic, demonstrating a trans-metalation step. The last step marks the reductive elimination, where the catalyst is transferred into its initial oxidation state of 0. This releases the R^1-R^2 coupling product with a newly formed carbon-carbon bond.

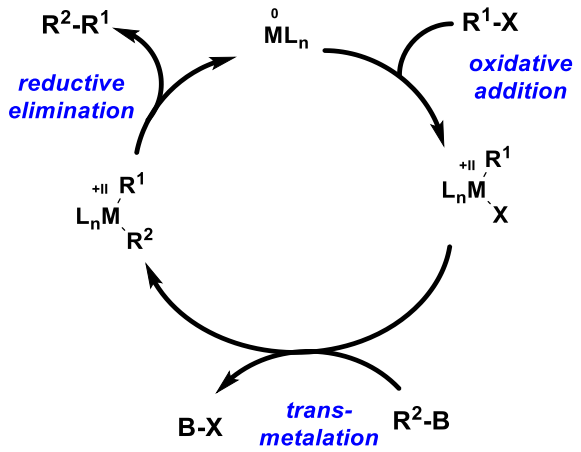

Figure 1.6. Cross coupling cycle for the formation of carbon-carbon bonds.

1.3 Quantum numbers and radiative transitions

Every electron in an atom is uniquely characterized by four so-called quantum numbers. The principal quantum number (n) defines the energy level in which an electron resides. The azimuthal quantum number (l) describes the orbital shape, taking integer values from 0 to n-1 and being denoted as s (l = 0), p (l = 1), d (l = 2) and f (l = 3). The magnetic quantum number (m_l) specifies the orientation of an orbital within its subshell (l), ranging from $-l$ to $+l$, including 0. The s, p, d and f subshell contain therefore sets of 1, 3, 5 and 7 orbitals with different orientations. Thus, the maximum number of

electrons per subshell is 2 (s), 6 (p), 10 (d) and 14 (f). The spin quantum number (m_s) indicates the intrinsic spin angular momentum of an electron, which can be either +1/2 or -1/2, often represented as spin-up (↑) or spin-down (↓). The total spin angular momentum (S) is the sum of all electron spins in an atom or molecule. In a system, where all electrons are paired – usually encountered in molecules – the total spin angular momentum S equals zero. In systems that contain unpaired electrons, S can be of full or half integer. The *multiplicity* in an atom or molecule is given by the formula 2S +1, yielding the number of possible spin orientations of an electron. Most molecules reside in the singlet state, due to fully paired electrons, resulting in S = 0. Due to two unbound electrons (S = 1), molecular oxygen resembles one of the prime examples for a molecule being in the triplet state.

Upon photoexcitation, a molecule or atom can absorb energy in form of a photon, resulting in an excited state, as illustrated in **Figure 1.7**.[22,23] For a molecule in the singlet ground state (S_0), absorption of a photon elevates it to an excited singlet state (S_1). Despite the increase in energy, the electron remains paired with the ground state electron. From there, various decay pathways are possible.

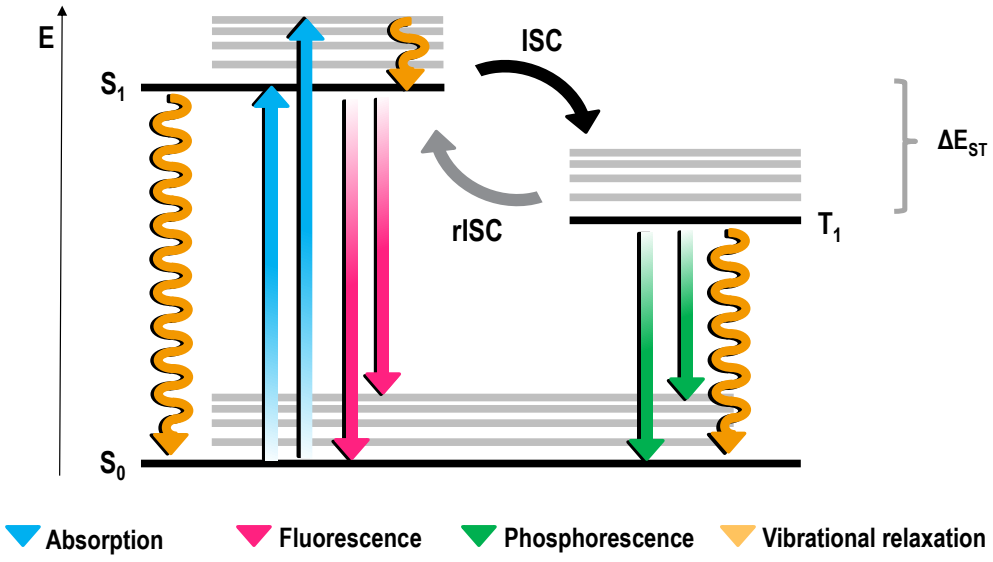

Figure 1.7. Jablonski diagram showing the electronic and vibrational levels as black and grey horizontal lines. Electronic transitions are marked by straight colored arrows and wave-like arrows indicate vibrational transitions. The colors correspond to different processes, which are given in the legend.

A radiative transition back to the ground state results *fluorescence*, typically occurring within nanoseconds (10^{-9} s) to microseconds (10^{-6} s). Alternatively, the molecule may undergo internal conversion (IC) where the excess energy is dissipated through vibrational relaxation and lost as heat. Intersystem crossing (ISC) describes the transition of an electron from an excited singlet (S_1) to a triplet state (T_1) and involves a spin-flip. A change in multiplicity from 1 to 3 is forbidden due to the spin

selection rule. Nevertheless, forbidden transitions are still possible but less frequent and become more probable, when the vibrational levels of S_1 and T_1 overlap. While in the T_1 state, several options are possible. Reverse intersystem crossing (rISC) allows for the back-conversion to the S_1 state, demonstrating again a spin-forbidden transition. Non-radiative decay occurs via IC and radiative decay happens via so-called *phosphorescence*.

The decay to the S_0 ground state by phosphorescence involves a forbidden spin-flip, usually giving rise to a lifetime ranging from milliseconds (10^{-3} s) to seconds. The spin-flip becomes possible due to spin-orbit coupling, which refers to interaction of the spin angular momentum of an electron and its orbital angular momentum. The sum of both gives the total angular momentum, which needs to be preserved during a spin flip event. Spin-orbit coupling opens up a path for a spin-flip by a change in orbital angular momentum.[24] Incorporating heavy atoms into the emissive chromophore enhances spin orbit coupling (scaling with the 4th power of the atomic number) and accelerates phosphorescence rates.[25]

As mentioned, rISC provides a route for the excited triplet state to decay. The only prerequisite is a small gap between T_1 and S_1 state, where the electron can be thermally activated to perform rISC. This process results in both prompt fluorescence (in ns) and delayed fluorescence (up to µs). The big difference to phosphorescence being, that all excited electrons decay via the singlet channel. The involved mechanism is commonly known as *thermally activated delayed fluorescence* or TADF.[26] Regardless of the decay mechanism (fluorescence, phosphorescence and TADF) involved, the number of emitted photons as a fraction of the absorbed photons is an important measure in quantifying the efficiency of emissive materials. This number is defined as the photoluminescence quantum yield (PLQY).

1.4 Thermally activated delayed fluorescence

1.4.1 Design strategies of TADF materials

The energies for the singlet and triplet state are given by equations (1) and (2).[27] E_{LUMO} corresponds to the energy of the LUMO, E_{HOMO} corresponds to the energy of the HOMO and J is the spin exchange energy.

$$E_{\mathrm{T}} = E_{\mathrm{HOMO}} - E_{\mathrm{LUMO}} - J \quad (1)$$

$$E_S = E_{\mathrm{HOMO}} - E_{\mathrm{LUMO}} + J \quad (2)$$

$$\Delta E_{\mathrm{ST}} = E_{\mathrm{S}} - E_{\mathrm{T}} = 2J \quad (3)$$

The singlet-triplet splitting ΔE_{ST} (equation (3)) equals therefore $2J$. A minimization of ΔE_{ST} can be achieved by reducing the spin exchange energy, which relies on the wavefunction overlap of the ground state (HOMO) and excited state (LUMO). On the level of the molecular structure, this can be accomplished by connecting an electron-deficient acceptor with an electron-rich donor in a nearly perpendicular arrangement. This configuration results in a high localization of the LUMO on the acceptor and the HOMO on the donor part (**Figure 1.8**).[26]

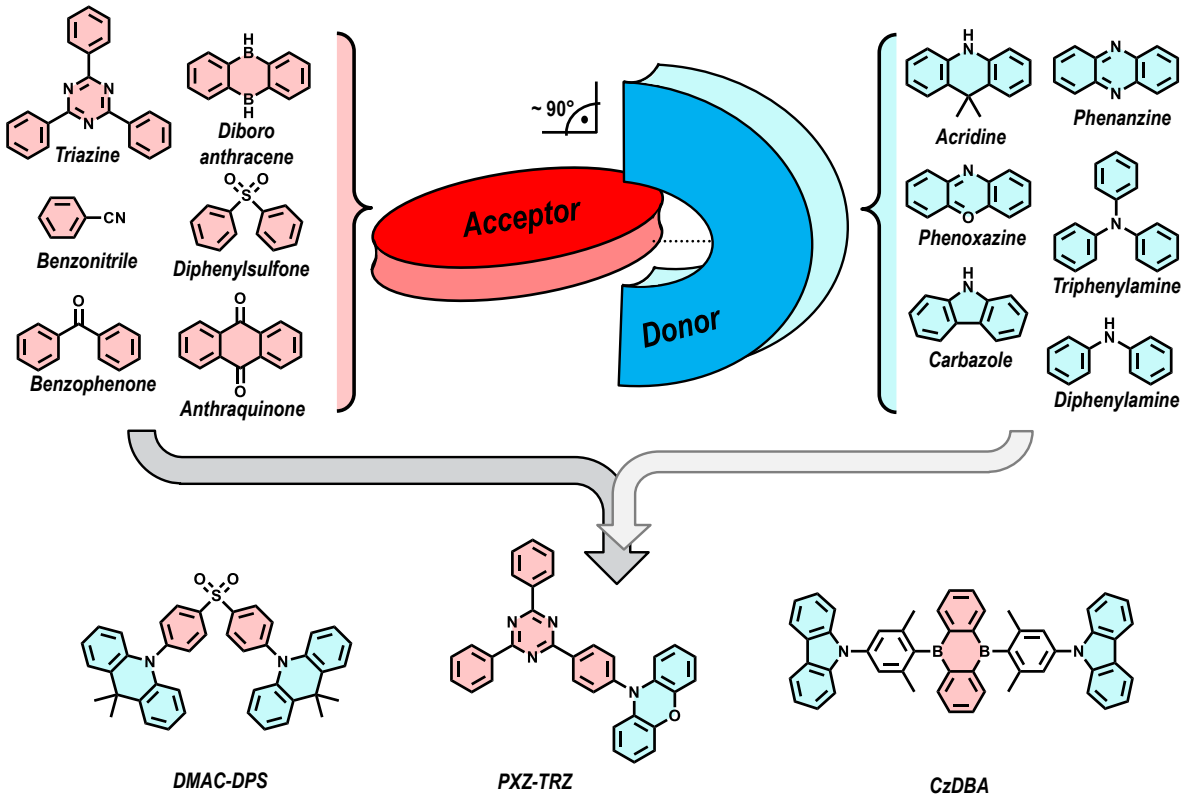

Figure 1.8. Schematic representation of materials utilizing TADF with a close to perpendicular arrangement between acceptor and donor. Commonly incorporated acceptor and donor building blocks and exemplary TADF emitters (DMAC-DPS, PXZ-TRZ and CzDBA) are illustrated.

A separation of HOMO and LUMO onto different molecular parts introduces two distinct excitation pathways. The first being a local excitation (LE) on the donor, based on a π-π* transition, and the second being a charge transfer (CT) excitation which is due to an electronic excitation from the donor to the acceptor.[28] The additional locally excited states play a crucial role for the rISC process, particularly in purely organic TADF materials, which lack heavy metals that mediate rISC. Thus, the direct transition from ^{3}CT to ^{1}CT via rISC is of low probability due to being spin-flip forbidden, as the electrons occupy the same spatial orbitals. This way, a spin flip cannot be compensated by a change in angular orbital momentum. However, a transition from triplet to singlet state can still occur through vibronic coupling

between ^{3}LE and ^{3}CT, where both states states mix characteristics, allowing for a spin flip from ^{3}LE to ^{1}CT due to the different orbital type.[29–31]

From a molecular perspective, three design strategies for TADF emitters have been popularized. The first efficient TADF emitters, reported by Adachi and co-workers, were based on twisted donor-acceptor structures.[26,32,33] Subsequent research led to the development of exciplex systems, where donor and acceptor reside on different molecules, forming an intermolecular CT state.[34] Both strategies utilize similar donor and acceptor units as building blocks. Frequently used donor units include carbazole (Cz), acridine (Ac), diphenylamine (DPA), triphenylamine (TPA), phenoxazine (PO) and their derivatives.[32,35–38] Typical acceptor units incorporate electron-withdrawing groups such as in diphenylsulfone (DPS), triazine (TRZ), benzophenone (BP), benzonitrile (BN) or diboroanthracene (DBA).[8,32,33,35,38]

These so-called first generation TADF emitters usually exhibit broad emission spectra with full width half maximum values (FWHM) of 60 – 100 nm, attributed to structural motions in the excited S_1 state and strong vibronic coupling between S_1 and S_0. However, for display applications, a broad emission is undesirable, which is the reason why a new generation of TADF emitters were developed by Hatakeyama and co-workers.[39] This third design strategy involves multi-resonance TADF emitters, which employ a polycyclic aromatic skeleton, in which the electron-donating atoms are positioned in the para-position of the electron withdrawing atoms.

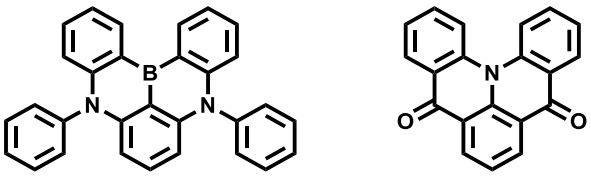

DABNA-1 ***QAO***

Figure 1.9. Multi-resonance TADF emitters DABNA-1 and QAO.

This arrangement results in a localized HOMO and LUMO on adjacent atoms, yielding short-range CT states with a small ΔE_{ST}. The rigidity of these MR-TADF emitters suppresses vibronic relaxations from the S_1 state and weakens the vibronic coupling of S_1 and S_0, resulting in narrow-band emission and improved color purity. Prominent examples are DABNA-1 (5,9-diphenyl-5,9-dihydro-5,9-diaza-13b-boranaphtho[3,2,1-*de*]anthracene) and QAO (quinolino[3,2,1-*de*]acridine-5,9-dione) (**Figure 1.9**), which both offer small FWHM values of 28 nm and 39 nm, respectively.[40,41]

1.4.2 Quantitative and qualitative measurements of TADF

The efficiency of TADF is primarily characterized by the rate of rISC (k_{rISC}), which can be described by equation (4):[42]

$$k_{\mathrm{rISC}} = A\, e^{-\frac{\Delta E_{\mathrm{ST}}}{k_{\mathrm{B}} T}} \tag{4}$$

Here, A represents a prefactor, k_{B} is the Boltzmann constant, T is the temperature and ΔE_{ST} is the energetic difference between singlet and triplet state. The rate of rISC depends therefore on applied temperature and on the intrinsic singlet-triplet splitting (ΔE_{ST}) of the investigated system. An experimental approach to verify TADF is to perform ultrafast optical measurements, such as time-resolved photoluminescence (TRPL). In **Figure 1.10**, both the power (**Figure 1.10a**) and temperature dependence (**Figure 1.10b**) of a typical TADF emitter are displayed.

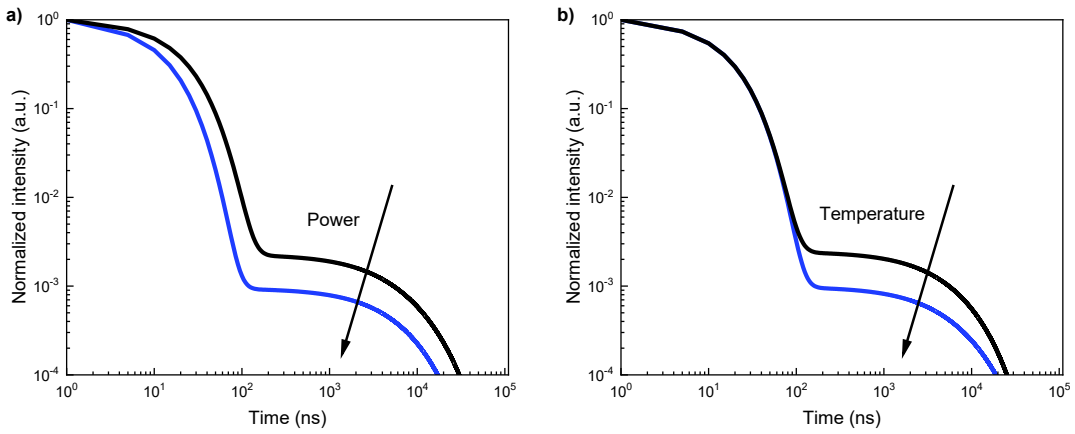

Figure 1.10. Simulated time-resolved photoluminescence spectra of a material exhibiting thermally activated delayed fluorescence. On a double logarithmic scale, the photoluminescence intensity is plotted against time, depicting the characteristic biexponential photoluminescence decay of TADF with prompt and delayed fluorescence. a) power-dependent study and b) temperature-dependent study.

In general, materials with TADF characteristics exhibit a biexponential photoluminescence decay, which is the direct result of prompt and delayed fluorescence. In an optical measurement, all initially generated excitons are singlet excitons. Prompt fluorescence originates from these singlet excitons that have not undergone any other transitions. Delayed fluorescence is a result of excitons that were converted to the triplet state through ISC and subsequently back-converted to the singlet state via rISC. Such re-harvested singlets accordingly decay via a delayed contribution to the total fluorescence. Carrying out a TRPL measurement at varying incident laser power (**Figure 1.10a**) can be used to

investigate the influence of bimolecular processes such as singlet-triplet and triplet-triplet annihilation.[43–47] At low power densities, bimolecular interactions are prevented, which contribute to the total PL decay. Thus, an increase of the total PL decay at higher power densities hints to singlet-triplet and triplet-triplet contributions.[43] Temperature-dependent measurements, as depicted in **Figure 1.10b**, are carried out to verify the involvement of an excited triplet state, which can be harvested due to a small singlet-triplet splitting. As explained by equation (4), rISC is temperature-dependent and lowering the temperature leads therefore to a shorter delayed lifetime. To prevent quenching of the excited triplet state, materials exhibiting TADF must be shielded from molecular oxygen. Hence, quantitative measurements need to be conducted under inert atmosphere and/or under sealed conditions (typically under vacuum, N_2 or Ar).[48]

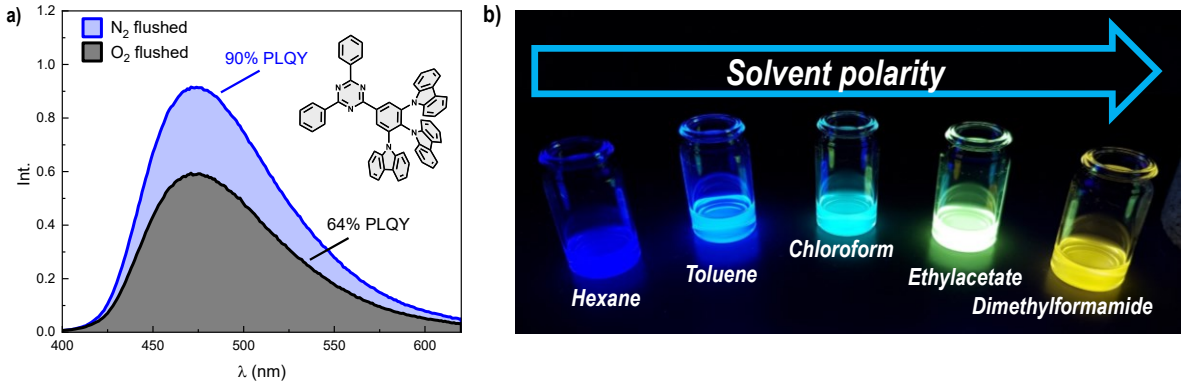

Figure 1.11. Emissive properties of chromophores exhibiting thermally activated delayed fluorescence. a) The detected fluorescence of the TADF emitter 3CzTRZ (9,9',9''-(5-(4,6-diphenyl-1,3,5-triazin-2-yl)benzene-1,2,3-triyl)tris(9*H*-carbazole)) in solution (toluene, 1×10^{-5} M) under inert conditions (N_2) and in presence of oxygen (O_2) excited at 370 nm. Under inert conditions, both the fluorescence and the PLQY are significantly higher than in presence of oxygen, thus indicating the involvement of an excited triplet state. b) Emission of the same chromophore in solvents of different polarity under UV irradiation (356 nm). The differently polarized solvents lead to a varying stabilization of the involved charge transfer state and therefore to a fluorescence spanning from deep blue to yellow.

A straightforward method to indicate the occurrence of TADF is to perform PLQY measurements under both inert conditions and in the presence of oxygen. An increase in PLQY under inert conditions implies the occurrence of TADF (**Figure 1.11a**). As previously mentioned, CT emission is a characteristic of materials exhibiting TADF, and can be experimentally detected by a solvatochromic shift in different solvents (**Figure 1.11b**), which demonstrates a qualitative way to indicate TADF.[49]

1.5 Light-generating processes in OLEDs

The first materials that were employed in OLEDs were solely capable to emit light by fluorescence (**Figure 1.12a**), meaning via an exited singlet state. The drawback of purely fluorescent emitters is that in OLEDs the excitons are formed in both the singlet and the triplet state. This means, that due to spin-statistics, 75% of the generated excitons are in the triplet state and only 25% reside in the singlet state. Hence, for OLEDs based on emitters that only relax via such direct or 'prompt' fluorescence a strong suppression in efficiency is observed. Besides efficiency limitations, triplet excitons can assist in chemical decomposition of organic semiconductors, which accelerates their degradation.[50]

Harvesting of triplet-excitons is therefore of fundamental interest. In 1998, a new concept was presented by *Baldo et al.* utilizing materials that harvest the excited triplet state via phosphorescence (**Figure 1.12b**), which theoretically enables an internal quantum efficiency (IQE) in OLEDs of up to 100%.[51] Phosphorescence in these emitters was achieved by incorporation of heavy metals, which increases the spin-orbit coupling and enables the spin-flip from the excited triplet state back to the ground state.

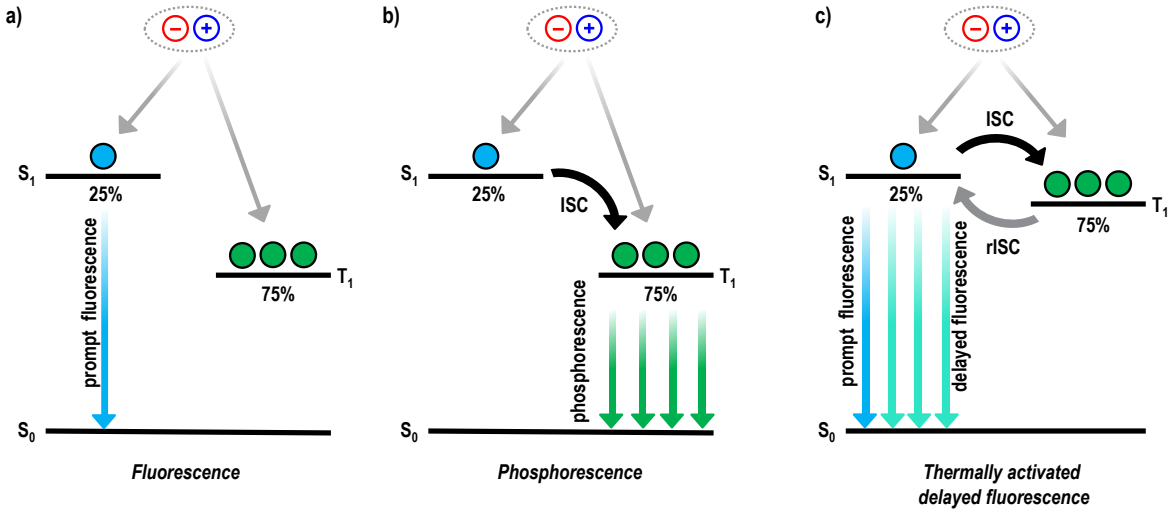

Figure 1.12. Radiative pathways in OLEDs including fluorescence, phosphorescence and thermally activated delayed fluorescence (TADF).

The major drawback in these materials is that phosphorescent emitters require transition metals such as iridium, which are expensive and harmful to the environment and health. Thus, in the past decade research interest focused particularly on materials exhibiting TADF (**Figure 1.12c**), which utilizes a small singlet-triplet splitting and opens up the route for converting all triplet excitons back to singlet excitons via rISC.[26] These materials can be fully organic without the use of any transition metals, but

with the benefit to offer IQEs of up to 100%. In the past years, highly efficient OLEDs based on TADF have been presented with external quantum efficiencies (EQE) exceeding 20 – 30%.[33,52,53]

1.6 Energetic levels in organic semiconductors

The correct understanding of the involved energetic levels in organic semiconductors is crucial for the development of efficient OLEDs. Important energetic levels in organic semiconductors are schematically shown in **Figure 1.13**.

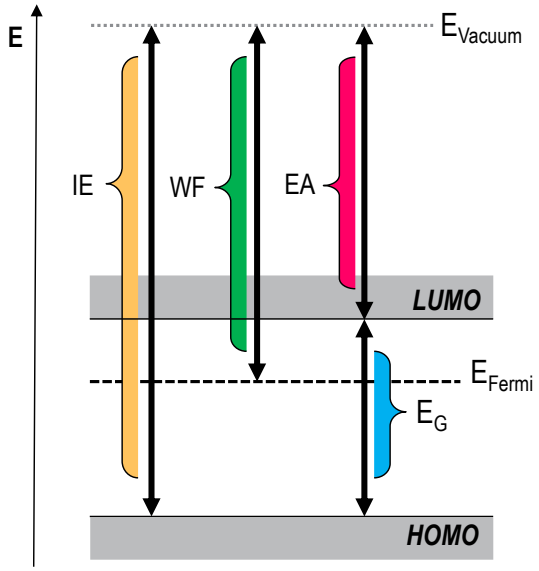

Figure 1.13. Energetic levels in organic semiconductors. Ionization energy (IE), Work function (WF), Electron affinity (EA) and Energy gap (E_G) with regard to the vacuum energy (E_{Vacuum}).[54]

The energy difference between vacuum energy (E_{vacuum}) and the HOMO of an organic semiconductor (or valance band for inorganic semiconductors) equals the ionization energy (IE), which is the minimum energy required to remove an electron from an atom or molecule in the gaseous state. The difference between E_{Vacuum} and LUMO of an organic semiconductor (or conduction band for inorganic semiconductors) is defined as the electron affinity (EA), being the energy gained by transferring an electron from the vacuum level to the LUMO. In general, organic semiconductors possess IEs between 4.5 – 6.5 eV and EAs between 2 – 4 eV.[55] The energetic difference between IE and EA is referred to as the band gap (E_G). In solid state physics, the Fermi level (E_{Fermi}) refers to a hypothetical energy level within the band gap of a semiconductor or insulator at which at thermodynamic equilibrium a 50% probability of occupation by an electron is given. The work function (WF) is defined by the energy difference between the Fermi level and the vacuum level (E_{Vacuum}) and is the minimum work required to remove an electron from a surface of a solid to the vacuum. In the special case of a metal, the work function equals the ionization energy. In (organic) semiconductors, the work function becomes a

theoretical construct, falling somewhere in between IE and EA, inside the band gap, as no occupied states are present. One of the most important techniques for determining the IE is ultraviolet photoelectron spectroscopy (UPS).[56] Ultraviolet light is used for excitation of electrons that occupy the HOMO. Subsequently photoelectrons are emitted, whose energy is detected. One of the most frequently used methods for the measurement of the EA is low-energy inverse electron spectroscopy (LEIPS).[56] Low energetic electrons (typically <5 eV) are used as an excitation source, generating light-emission in the near-ultraviolet region.

1.7 Operation of single carrier devices

1.7.1 Device layout of single carrier devices

Light generation in OLEDs relies on injection, transport and recombination of electrons and holes, making them so-called "dual carrier" devices. A technique to study the transport of electrons and holes in organic semiconductors independently is to fabricate *single carrier* devices, namely electron- and hole-only devices.[57] These devices typically feature an electrode-semiconductor-electrode layout. Of these electrodes, one provides ohmic charge injection, whereas the work function of the other is chosen such that injection of the opposite charge carrier is prevented. As mentioned above, ohmic charge injection is established when the electrode's work function matches the HOMO or LUMO of the organic material. Ideally, both electrodes offer ohmic charge injection, enabling the study of the charge transport regardless of applied bias. In a symmetric hole-only device (**Figure 1.14a**), both electrodes have work functions that match the HOMO of the organic semiconductor, facilitating efficient hole extraction and injection from both sides.

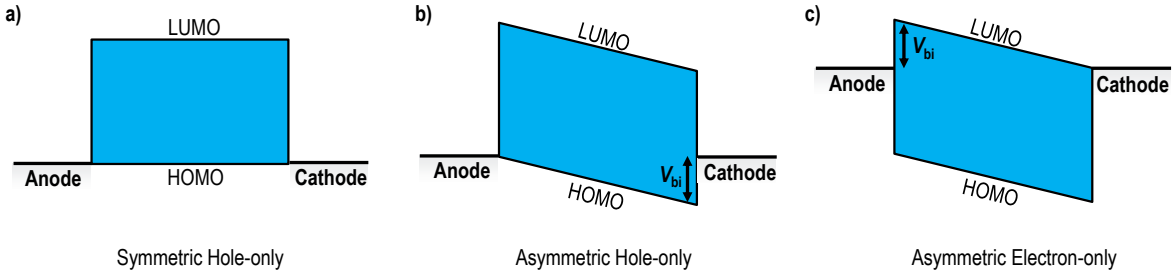

Figure 1.14. Single carrier devices with different contact work functions at thermal equilibrium resulting in built-in voltages (V_{bi}). a) A symmetric hole-only device with two ohmic contacts. b) An asymmetric hole-only device with one ohmic hole contact. c) An asymmetric electron-only device with one ohmic electron contact

Thus, *injection* and *extraction* depend on the applied electric field/voltage. Employing two electrodes with different work functions, where only one forms an ohmic contact and the other one does not match the HOMO (or LUMO) of the semiconductor (rendering it non-ohmic), leads to the formation of a built-in voltage (V_{bi}) across the layer (illustrated in **Figure 1.14b** and **1.14c**).

The built-in voltage V_{bi} can be equal to the work function difference, when neutral contacts such as gold or aluminum are used, but varies considerably for non-neutral contacts, depending on the semiconductor they are contacted with.[58] A single carrier device featuring an internal built-in voltage V_{bi} displays a noticeable shift in the applied voltage. To ensure accurate analysis in such devices, the built-in voltage must be subtracted from the applied voltage to establish a corrected voltage scale. In some single carrier devices, where one contact is ohmic and the other is non-ohmic, no built-in voltage is be observed during a current-voltage measurement, which can be attributed to a small barrier height on the non-ohmic contact side, which is compensated by band-bending (typically in the 0.3 – 0.4 V range). Nevertheless, this setup reduces the injected current via the non-ohmic contact, resulting in strongly asymmetric characteristics.

1.7.2 Current-voltage characteristics of single carrier devices during operation

As previously mentioned, employing electrodes of different work functions in a single carrier device leads to the formation of a built-in voltage across the organic layer and to an electric field, pointing toward the injecting contact. The current-voltage characteristics of single carrier devices can be categorized into two regimes. At low voltages, below the built-in voltage V_{bi}, charge carriers which diffused from the contacts or which are intrinsically present in the organic semiconductor dominate the current.[59,60] Diffusion is a result of the charge carrier gradient across the organic layer. For symmetric devices without a built-in voltage V_{bi}, the current increases linearly with applied voltage on a double logarithmic scale and can be accurately described by Ohm's law (5), where n represents the charge carrier density, μ denotes the charge carrier mobility, q signifies the elementary charge and L stands for the layer thickness.

$$J = nq\mu \frac{V}{L} \tag{5}$$

The linear scaling behavior is depicted by the red fit in **Figure 1.15a**, where the hole-only current-voltage (*J-V*) characteristics of DBA-DI (5-(5,9-dioxa-13b-boranaphtho[3,2,1-de]anthracen-7-yl)-10,15-diphenyl-10,15-dihydro-5*H*-diindolo[3,2-a:3',2'-c]carbazole), an organic semiconductor, are illustrated in a double logarithmic plot.

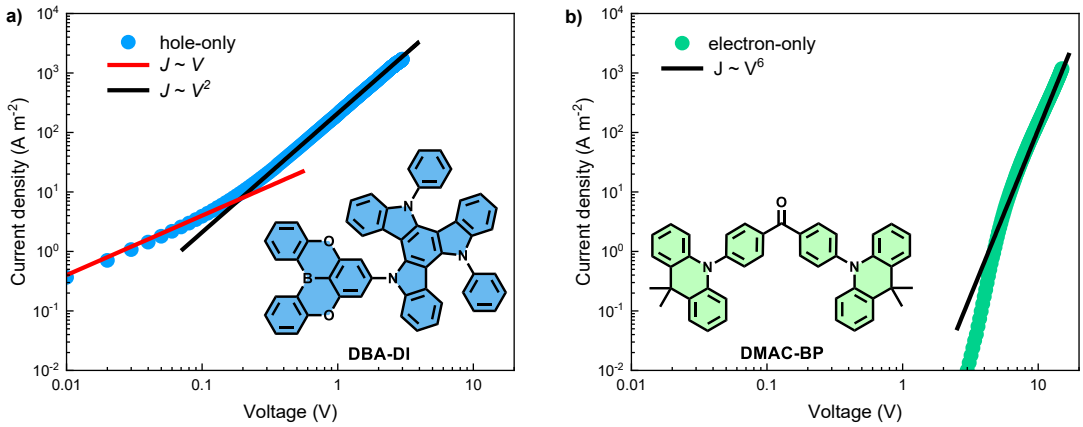

Figure 1.15. Trap-free hole-only current-voltage (*J-V*) characteristics of DBA-DI (a) and trap-limited electron-only current-voltage (*J-V*) characteristics of DMAC-BP (b) shown with molecular structures.

For asymmetric devices where a built-in voltage V_{bi} exists at low voltages, below V_{bi} the electric field is negative, meaning opposite to the applied electric field, and the current is dominated by diffusion. This diffusion current is characterized by an exponential dependence on bias voltage. When the amount of injected carriers exceeds the background carrier density (exceeding the built-in voltage V_{bi}), the current exhibits a quadratic scaling with voltage, indicated by a slope of 2, where it reaches its space charge limited current (SCLC), which is depicted in **Figure 1.15a** (blue symbols, black fit). In this second regime, the electric field becomes positive (reversed to the situation before) and points towards the collecting contact and the current is predominately governed by drift. The SCLC represents the maximum current a single carrier device can sustain and is described by the Mott-Gurney law (6), which is expressed as:[40]

$$J = \frac{9}{8}\varepsilon\mu\,\frac{(V - V_{bi})^2}{L^3} \tag{6}$$

Here ε represents the dielectric constant of the organic semiconductor, μ signifies the charge carrier mobility, V is the applied voltage, V_{bi} the built-in voltage and L represents the layer thickness.

1.7.3 Charge-Trapping in organic semiconductors

The quadratic dependence on voltage of an SCLC serves as a distinctive indicator of trap-free charge transport. While trap-free hole transport is common in various organic semiconductors, including polymers and molecules, electron-transport frequently suffers from charge-trapping. Charge traps represent an energetic state situated within the band gap of an organic semiconductor. Charge transport affected by charge traps typically exhibits a more pronounced voltage dependence, often with slopes of

up to 6.[61] Such a trap-limited electron current is displayed in **Figure 1.15b** for DMAC-BP (Bis(4-(9,9-dimethylacridin-10(9*H*)-yl)phenyl)methanone). Injected charge carriers get trapped in these localized states, which can drastically hinder their transport. In OLEDs, which rely on efficient recombination of both carrier types, charge trapping plays a critical role for their performance. Non-radiative trap-assisted recombination involves the recombination of trapped charge carriers with incoming charge carriers of opposite sign, leading to their non-radiative deactivation.[62,63] Furthermore, trapping of one type of charge carrier results in an imbalance hole and electron transport through the organic semiconductor. In case of electron trapping, hole-electron recombination occurs closer to the cathode, which ultimately leads to a reduced optical outcoupling of generated photons.[63]

A recent study identified the presence of two distinct trap levels situated at -3.6 eV below the vacuum energy for electrons and -6.0 eV for holes.[55] This discovery suggests, that trapping in organic semiconductors has probably a common extrinsic origin. Materials possessing energy levels within this window, with electron affinities below -3.6 eV and ionization energies above -6.0 eV, exhibit trap-free electron and hole transport. While the precise origin of these trap levels remains uncertain, theoretical calculations have suggested that water-clusters might be linked to hole trapping, whereas oxygen-water complexes and/or molecular oxygen could contribute to electron trapping.[55,64–66] Additional to that, various factors have been proposed as potential causes for charge trapping, including environmental contaminations, impurities from the synthesis processes and intrinsic defects within the materials.[67,68]

1.8 Operation of organic light-emitting diodes

1.8.1 Device layout of organic light-emitting diodes

Organic light-emitting diodes have become particularly popular due to their vibrant colors, easy fabrication and high efficiency, making them the perfect candidate for mobile applications. In its simplest configuration, an OLED comprises a single layer of organic semiconductor sandwiched between two electrodes, being also referred to as a *single-layer* device. The working principle is displayed in **Figure 1.16**.

By applying a voltage, electrons are injected from the cathode into the LUMO of the organic semiconductor, while at the same time holes are injected into the HOMO of the respective organic semiconductor. Charge injection plays a crucial role in these single-layer devices, to ensure that charges are not lost at the semiconductor-electrode interface. Thus, the work function of the anode and cathode have to match the HOMO and LUMO of the emitting semiconductor to achieve ohmic behavior. The difference between the anode and cathode in work function results in a built-in voltage V_{bi} across the device

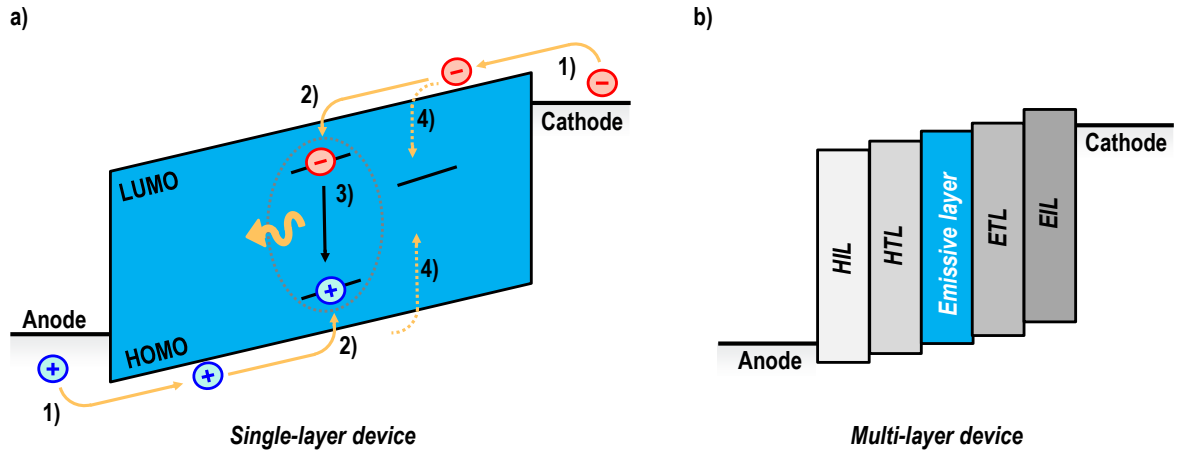

Figure 1.16. a) Schematic band diagram explaining the working principle of a single-layer OLED. 1) Charge injection 2) Charge transport within the emissive layer 3) *Langevin*-type recombination of hole and electron forming an exciton with subsequent light generation 4) non-radiative trap-assisted recombination. b) Schematic band diagram of a multi-layer OLED showing anode, hole injection layer (HIL), hole transport layer (HTL), emissive layer, electron transport layer (ETL), electron injection layer (EIL) and cathode.

When a voltage is applied, charges begin to move and meet inside the emissive layer, where an *exciton* is formed. This exciton is a quasiparticle consisting of an electron-hole pair, which is held together by Coulombic forces. In organic semiconductors, excitons are predominantly of the *Frenkel* type, meaning that the relatively low dielectric constants result in large binding exciton energies (0.4 – 1.0 eV).[69] This forces the excitons to exhibit a small spatial radius with high localization on the same molecule. The formed exciton can be of singlet or triplet nature and must release energy to transition back to the ground state. This can be achieved radiatively through light emission also known as bimolecular *Langevin*-type recombination (**Figure 16a**). Most organic semiconductors have energetic states (or *trap-states*, as mentioned in 1.7.3) inside their band gap, which can lead to non-radiative trap-assisted recombination. The energy of the released photon corresponds to the energy gap between HOMO and LUMO.

The single-layer device layout puts a high demand on efficient charge injection, transport and recombination. As such, typically more organic layers are introduced, which ensure that all charges and excitons recombine within the emissive layer, making these devices a so-called *multi-layer* stack.[70] Hole and electron injection (HIL and EIL) layers are inserted to reduce barriers at the contacts improving charge injection. Hole and electron transport layers (HTL and ETL) are used, to account for imbalanced charge transport, which is encountered in most organic semiconductors. Exciton blocking layers (EBL) are incorporated to confine exciton recombination within the emissive layer and maximize the internal quantum efficiency. Using several layers of organic material has an additional advantage in

positioning the emissive layer close to the optimum inside the optical microcavity, which maximizes the light output.[71] Although offering clear advantages, multi-layer OLEDs happen to show several drawbacks. The incorporation of several organic layers is costly and complex, opening up room for errors during the deposition steps. Next, the heterojunctions between different materials lead to voltage losses, reducing the power efficiency (in lm W^{-1}) of the final device. Lastly, device interpretation becomes cumbersome, as every additional layer introduces its own charge transport characteristics and barrier heights.

1.8.2 Current-voltage characteristics of OLEDs during operation

In a typical single-layer trap-free OLED, three distinct operational regimes can be observed. These *J-V* characteristics are elucidated by band diagrams in **Figure 1.17**. Similar to single carrier devices featuring two electrodes with different work functions, OLEDs also exhibit a built-in voltage V_{bi}.

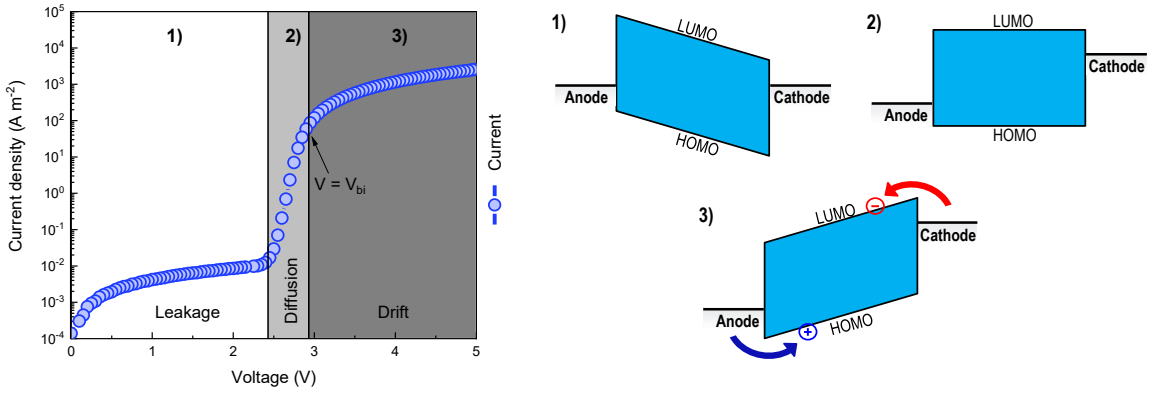

Figure 1.17. *J-V* characteristics of a trap-free OLED. Three distinct regimes (Leakage, Diffusion, Drift) are observed during operation.

This V_{bi} in OLEDs is typically larger than in single carrier devices, owing to a greater offset in work functions of anode and cathode, which align with the HOMO and LUMO of the organic semiconductor. At voltages below V_{bi}, only diffused charge carriers are present in the active layer. In the first regime, the diffused current is overshadowed by the leakage current that originates in parasitical currents or shorts. The leakage current increases linearly with applied voltage in accordance with Ohm's law. Typically, the leakage current should be as low as possible. As the voltage increases and approaches V_{bi}, the built-in field is compensated for and the contribution of diffusing charge carriers becomes more significant, leading to an exponential current-voltage dependence on a semi-logarithmic scale in this regime (see **Figure 1.17**).[72] The exponential growth is referred to as the diffusion regime and is described by the Shockley equation (7)

$$J = J_o \left[\exp\left(\frac{qV}{\eta k_B T}\right) - 1\right] \quad (7)$$

where J_o is the saturation current density, being the current due to motion of minority charge carriers when the diode is reversely biased, η represents the ideality factor (ranging from 1 – 2), k_B is the Boltzmann constant and T the absolute temperature. When the applied voltage matches the built-in voltage, a flat-band condition is present. At voltages exceeding the built-in voltage, the drift of injected charge carriers predominates, resulting in a quadratic scaling of current with applied voltage.

1.8.3 Performance Characterization of OLEDs

The performance of OLEDs can be evaluated by different metrics, with one of the most prominent ones for display applications being the external quantum efficiency (EQE), defined by following equation[73]:

$$n_{EQE} = \eta_{OUT} \times \eta_{S/T} \times \gamma \times \phi_{PLQY} \quad (8)$$

where η_{OUT} corresponds to the outcoupling efficiency, $\eta_{S/T}$ denotes the spin factor, γ equals the electrical efficiency and ϕ_{PLQY} stands for the PLQY. The outcoupling efficiency η_{OUT} denotes the fraction of generated photons emitted from the device. The outcoupling efficiency η_{OUT} for unmodified OLEDs is typically in the range of 20 – 30%.[74] The primary contributor to outcoupling losses is the mismatch in refractive indices between the organic semiconductor (≈ 1.7 – 1.8), the glass substrate (≈ 1.5) and air (≈ 1.0). The spin factor $\eta_{S/T}$ represents the number of excitons decaying radiatively based on spin statistics. For fluorescent OLEDs utilizing materials that harvest exclusively singlet excitons, the spin factor $\eta_{S/T}$ is 0.25 while it equals 1 for phosphorescent materials or for those exhibiting TADF. The electrical efficiency γ indicates the proportion of injected charge carriers that generate excitons and is influenced by charge injection, charge transport and the electron-hole recombination. In the case of ambipolar trap-free charge transport γ approaches 1. The experimental EQE is determined by measuring the wavelength λ and the current density *J*, using following equation (9),

$$n_{EQE} = \frac{\int F_\lambda \times \frac{\lambda}{hc}\, d\lambda}{J \times \frac{1}{e}} \quad (9)$$

Where F_λ represents luminous flux of each wavelength of the electroluminescence spectrum (EL), λ is the wavelength, J is the current density and *e* is the elementary charge. Constants *h* and *c* represent the Planck constant and the speed of light, respectively.

Next to EQE, two other key parameters are used to assess the performance of an OLED. The power efficiency (PE) plays an important role in commercial applications and is usually expressed in lm W^{-1}.[75] It is described by the ratio of luminous flux (F) to electrical power (P), with P being the product of applied current density J and voltage V.

$$n_{PE} = \frac{F}{P} = \frac{L \times \pi}{J \times V} \tag{10}$$

The current efficiency (CE) is defined as the ratio of luminance L (cd) and current density J and usually given in cd A^{-1}.

$$n_{CE} = \frac{L}{J} \tag{11}$$

1.9 Scope and outline

This thesis deals with the investigation and optimization of electron and hole transport in organic semiconductors. The organic semiconductors presented in the 2nd chapter consist of a donor and an acceptor part and were systematically studied for their electrical transport properties by expanding or reducing the donor part. These variations on the donor lead to a clearly measurable difference in electron transport. These differences are unexpected because electron transport is expected to happen on the acceptor. This hints to the fact, that molecular stacking plays a critical role and that organic films happen to exhibit a certain degree of ordering. These observations are particularly interesting because the investigated compounds exhibit bandgaps between 2.5 – 3.0 eV, thereby emitting light in the blue region of the light spectrum. As mentioned in the introductory chapter, a common problem in organic semiconductors is the so-called *charge-trapping*. This undesirable effect is always observed for either holes or electrons, when the bandgap of an organic semiconductor is sufficiently large (> 2.5 eV). The targeted modifications of the chemical structure shown here can completely suppress the charge trapping for compounds with a bandgap larger than 2.5 eV.

In the 3rd chapter, the fabrication of efficient blue organic light-emitting diodes is addressed. For this purpose, a hole injection layer based on PEDOT:PSS was modified to enable efficient and barrier-free injection of positive charge carriers into organic semiconductors with a deep HOMO of up to 5.9 eV. As an active layer, a host-guest system consisting of SpiroAc-TRZ as a blue emitter and mCPCN as a host material was used. In this very simple single-layer OLED, all loss processes could be minimized, achieving an internal quantum efficiency of almost 100%.

In the 4th chapter, the photophysical properties of 3CzTRZ, one of the most promising candidates from the first study, are investigated. It is demonstrated, that despite excellent charge transport properties, the photoluminescence quantum yield (PLQY) is relatively low. The photophysical cause can be traced

back to a slow rISC rate. By incorporating 3CzTRZ into a host material, the triplet lifetime can be significantly increased, giving enough time, to harvest triplet excitons and thereby tripling the OLED efficiency to 15%.

With its large bandgap of ~3 eV, high triplet level and excellent balanced transport, 3CzTRZ demonstrates an ideal host material for emitters with lower singlet and triplet levels. In the 5th and last chapter, DMAC-BP was selected as guest-emitter. DMAC-BP is an efficient green emitter that has already been employed in multi-layer organic light-emitting diodes. However, limited by its electron transport, DMAC-BP is not suitable for efficient use in single-layer organic light-emitting diodes. In combination with the host material 3CzTRZ, the electron transport of DMAC-BP can be increased by several orders of magnitude, enabling high efficiencies and longer lifetimes in a simple device architecture.

References

[1] M. Pope, H. P. Kallmann, P. Magnante, *J. Chem. Phys.* **1963**, *38*, 2042.

[2] C. W. Tang, S. A. Vanslyke, *Appl. Phys. Lett.* **1987**, *51*, 913.

[3] S. Nakamura, Y. Harada, M. Seno, *Appl. Phys. Lett.* **1991**, *58*, 2021.

[4] C. Mo, W. Fang, Y. Pu, H. Liu, F. Jiang, *J. Cryst. Growth* **2005**, *285*, 312.

[5] A. Bässler, H., Köhler, *Charge Transport in Organic Semiconductors*, Springer, Berlin - Heidelberg, **2011**.

[6] V. Coropceanu, J. Cornil, D. A. da S. Filho, Y. Olivier, R. Silbey, J.-L. Brédas, *Chem. Rev.* **2007**, *107*, 926.

[7] K. Takimiya, S. Shinamura, I. Osaka, E. Miyazaki, *Adv. Mater.* **2011**, *23*, 4347.

[8] T. L. Wu, M. J. Huang, C. C. Lin, P. Y. Huang, T. Y. Chou, R. W. Chen-Cheng, H. W. Lin, R. S. Liu, C. H. Cheng, *Nat. Photonics* **2018**, *12*, 235.

[9] Q. Jiang, J. Zhang, Z. Mao, Y. Yao, D. Zhao, Y. Jia, D. Hu, Y. Ma, *Adv. Mater.* **2022**, *34*, 1.

[10] W. Brütting, *Phys. Org. Semicond.* **2006**, 1.

[11] D. Braga, A. Jaafari, L. Miozzo, M. Moret, S. Rizzato, A. Papagni, A. Yassar, *European J. Org. Chem.* **2011**, 4160.

[12] C. F. R. Mackenzie, S. Y. Kwak, S. Kim, E. Zysman-Colman, *Dalt. Trans.* **2023**, *52*, 4112.

[13] E. Lim, B. J. Jung, H. K. Shim, *Macromolecules* **2003**, *36*, 4288.

[14] J. Ouyang, *SmartMat* **2021**, *2*, 263.

[15] S. M. A. Mokhtar, E. Alvarez de Eulate, M. Yamada, T. W. Prow, D. R. Evans, *Med. Devices Sensors* **2021**, *4*, 1.

[16] Grime, *Notes Queries* **1863**, *s3-IV*, 316.

[17] G. A. Olah, *Acc. Chem. Res.* **1971**, *4*, 240.

[18] M. Mąkosza, *Chem. - A Eur. J.* **2020**, *26*, 15346.

[19] J.K.Stille, *Pure Appl. Chem.* **1985**, *57*, 1771.

[20] A. O. King, N. Okukado, E. I. Negishi, *J. Chem. Soc. Chem. Commun.* **1977**, 683.

[21] N. Miyaura, K. Yamada, A. Suzuki, *Tetrahedron Lett.* **1979**, *20*, 3437.

[22] A. Jablonski, *Nat.* **1933**, *131*, 839.

[23] D. Frackowiak, *J. Photochem. Photobiol. B Biol.* **1988**, *2*, 399.

[24] A. Köhler, H. Bässler, *Mater. Sci. Eng. R Reports* **2009**, *66*, 71.

[25] C. M. Marian, *Wiley Interdiscip. Rev. Comput. Mol. Sci.* **2012**, *2*, 187.

[26] H. Uoyama, K. Goushi, K. Shizu, H. Nomura, C. Adachi, *Nature* **2012**, *492*, 234.

[27] P. Pander, F. B. Dias, *Disp. Imaging* **2017**, *2*, 249.

[28] F. B. Dias, J. Santos, D. R. Graves, P. Data, R. S. Nobuyasu, M. A. Fox, A. S. Batsanov, T. Palmeira, M. N. Berberan-Santos, M. R. Bryce, A. P. Monkman, *Adv. Sci.* **2016**, *3*, 1.

[29] M. K. Etherington, J. Gibson, H. F. Higginbotham, T. J. Penfold, A. P. Monkman, *Nat. Commun.* **2016**, *7*, 1.

[30] J. Gibson, A. P. Monkman, T. J. Penfold, *ChemPhysChem* **2016**, 2956.

[31] T. J. Penfold, E. Gindensperger, C. Daniel, C. M. Marian, *Chem. Rev.* **2018**, *118*, 6975.

[32] Q. Zhang, D. Tsang, H. Kuwabara, Y. Hatae, B. Li, T. Takahashi, S. Y. Lee, T. Yasuda, C. Adachi, *Adv. Mater.* **2015**, *27*, 2096.

[33] Q. Zhang, B. Li, S. Huang, H. Nomura, H. Tanaka, C. Adachi, *Nat. Photonics* **2014**, *8*, 326.

[34] M. Sarma, K. T. Wong, *ACS Appl. Mater. Interfaces* **2018**, *10*, 19279.

[35] D. R. Lee, M. Kim, S. K. Jeon, S. H. Hwang, C. W. Lee, J. Y. Lee, *Adv. Mater.* **2015**, *27*, 5861.

[36] Y. Liu, G. Xie, Z. Ren, S. Yan, *ACS Appl. Polym. Mater.* **2019**, *1*, 2204.

[37] S. Sohn, B. Hyun Koh, J. Y. Baek, H. Chan Byun, J. H. Lee, D. S. Shin, H. Ahn, H. K. Lee, J. Hwang, S. Jung, Y. H. Kim, *Dye. Pigment.* **2017**, *140*, 14.

[38] F. Baraket, B. Pedras, É. Torres, M. J. Brites, M. Dammak, M. N. Berberan-Santos, *Dye. Pigment.* **2020**, *175*, 1.

[39] T. Hatakeyama, K. Shiren, K. Nakajima, S. Nomura, S. Nakatsuka, K. Kinoshita, J. Ni, Y. Ono, T. Ikuta, *Adv. Mater.* **2016**, *28*, 2777.

[40] N. F. Mott, R. W. Gurney, *Electronic Processes in Ionic Crystals*, Oxford University Press, London, **1940**.

[41] Y. Yuan, X. Tang, X. Y. Du, Y. Hu, Y. J. Yu, Z. Q. Jiang, L. S. Liao, S. T. Lee, *Adv. Opt. Mater.* **2019**, *7*, 6.

[42] F. B. Dias, T. J. Penfold, A. P. Monkman, *Methods Appl. Fluoresc.* **2018**, *5*, 012001.

[43] K. Thakur, B. van der Zee, G. J. A. H. Wetzelaer, C. Ramanan, P. W. M. Blom, *Adv. Opt. Mater.* **2022**, *10*.

[44] K. Thakur, B. van der Zee, O. Sachnikk, C. Haese, R. Graf, J. J. Michiels, C. R. Gert-Jan A.H. Wetzelaer, P. W. M. Blom, *Adv. Photonics Res.* **2024**, *2400022*, 1.

[45] D. Hertel, H. Bässler, R. Guentner, U. Schert, *J. Chem. Phys.* **2001**, *115*, 10007.

[46] J. Yu, R. Lammi, A. J. Gesquiere, P. F. Barbara, *J. Phys. Chem. B* **2005**, *109*, 10025.

[47] H. Sternlicht, G. C. Nieman, G. W. Robinson, *J. Chem. Phys.* **1963**, *38*, 1326.

[48] T. Serevičius, R. Skaisgiris, G. Kreiza, J. Dodonova, K. Kazlauskas, E. Orentas, S. Tumkevičius, S. Juršenas, *J. Phys. Chem. A* **2021**, *125*, 1637.

[49] P. L. Dos Santos, J. S. Ward, A. S. Batsanov, M. R. Bryce, A. P. Monkman, *J. Phys. Chem. C* **2017**, *121*, 16462.

[50] M. Tanaka, R. Nagata, H. Nakanotani, C. Adachi, *Commun. Mater.* **2020**, *1*, 1.

[51] M. A. Baldo, D. F. O'Brien, Y. You, A. Shoustikov, S. Sibley, M. E. Thompson, S. R. Forrest, *Nature* **1998**, *395*, 151.

[52] C. Y. Chan, M. Tanaka, Y. T. Lee, Y. W. Wong, H. Nakanotani, T. Hatakeyama, C. Adachi, *Nat. Photonics* **2021**, *15*, 203.

[53] C. Adachi, M. A. Baldo, M. E. Thompson, S. R. Forrest, *J. Appl. Phys.* **2001**, *90*, 5048.

[54] A. Kahn, *Mater. Horizons* **2016**, *3*, 7.

[55] N. B. Kotadiya, A. Mondal, P. W. M. Blom, D. Andrienko, G. J. A. H. Wetzelaer, *Nat. Mater.* **2019**, *18*, 1182.

[56] M. Terashima, T. Miyayama, T. Shirao, H. W. Mo, Y. Hatae, H. Fujimoto, K. Watanabe, *Surf. Interface Anal.* **2020**, *52*, 948.

[57] P. W. M. Blom, M. C. J. M. Vissenberg, *Mater. Sci. Eng. R Reports* **2000**, *27*, 53.

[58] G. A. H. Wetzelaer, *Phys. Rev. Appl.* **2020**, *13*, 1.

[59] G. A. H. Wetzelaer, P. W. M. Blom, *Phys. Rev. B - Condens. Matter Mater. Phys.* **2014**, *89*, 1.

[60] N. I. Craciun, J. J. Brondijk, P. W. M. Blom, *Phys. Rev. B - Condens. Matter Mater. Phys.* **2008**, *77*, 1.

[61] H. T. Nicolai, M. Kuik, G. A. H. Wetzelaer, B. De Boer, C. Campbell, C. Risko, J. L. Brédas, P. W. M. Blom, *Nat. Mater.* **2012**, *11*, 882.

[62] G. J. A. H. Wetzelaer, M. Scheepers, A. M. Sempere, C. Momblona, J. Ávila, H. J. Bolink, *Adv. Mater.* **2015**, *27*, 1837.

[63] M. Kuik, L. J. A. Koster, A. G. Dijkstra, G. A. H. Wetzelaer, P. W. M. Blom, *Org. Electron.* **2012**, *13*, 969.

[64] J. M. Zhuo, L. H. Zhao, R. Q. Png, L. Y. Wong, P. J. Chia, J. C. Tang, S. Sivaramakrishnan, M. Zhou, E. C. W. Ou, S. J. Chua, W. S. Sim, L. L. Chua, P. K. H. Ho, *Adv. Mater.* **2009**, *21*, 4747.

[65] P. K. Nayak, R. Rosenberg, L. Barnea-Nehoshtan, D. Cahen, *Org. Electron.* **2013**, *14*, 966.

[66] A. Seemann, T. Sauermann, C. Lungenschmied, O. Armbruster, S. Bauer, H. J. Egelhaaf, J. Hauch, *Sol. Energy* **2011**, *85*, 1238.

[67] W. Graupner, G. Leditzky, G. Leising, U. Scherf, *Phys. Rev. B - Condens. Matter Mater. Phys.* **1996**, *54*, 7610.

[68] M. Meier, S. Karg, K. Zuleeg, W. Brütting, M. Schwoerer, *J. Appl. Phys.* **1998**, *84*, 87.

[69] P. Gomes da Costa, E. M. Conwell, *Phys. Rev. B* **1993**, *48*, 1993.

[70] D. Ammermann, A. Böhler, S. Dirr, H. H. Johannes, W. Kowalsky, *AEU-Archiv fur Elektron. und Ubertragungstechnik* **1996**, *50*, 327.

[71] A. Salehi, X. Fu, D. H. Shin, F. So, *Adv. Funct. Mater.* **2019**, *29*, 1.

[72] G. A. H. Wetzelaer, M. Kuik, H. T. Nicolai, P. W. M. Blom, *Phys. Rev. B - Condens. Matter Mater. Phys.* **2011**, *83*, 1.

[73] B. Van der Zee, Y. Li, G. J. A. H. Wetzelaer, P. W. M. Blom, *Adv. Mater.* **2022**, *34*, 2108887.

[74] W. Brütting, J. Frischeisen, T. D. Schmidt, B. J. Scholz, C. Mayr, *Phys. Status Solidi Appl. Mater. Sci.* **2013**, *210*, 44.

[75] P. Vandersteegen, G. Schwartz, P. Bienstman, R. Baets, *Appl. Opt.* **2008**, *47*, 1947.

2. Suppression of charge-carrier trapping by molecular design

Most organic semiconductors suffer from unipolar charge transport, which is caused by trapping of either electrons or holes. As introduced in chapter 1.7.3, two distinct trap levels for holes and electrons were identified at -6.0 eV and -3.6 eV below the vacuum energy, respectively. Organic semiconductors, which have their IE and EA levels within this window, experience trap-free electron and hole transport. However, for organic semiconductors with a band gap larger than 2.4 eV, charge trapping becomes unavoidable. This poses a significant challenge to fabricate trap-free blue-emitting OLEDs, which require band gaps of 2.8 – 3.0 eV. In this chapter, a molecular strategy is presented, where the HOMO and LUMO reside on different parts of the molecule. By tuning their chemical structure and molecular stacking, the electron-transporting LUMO can be protected from extrinsic impurities, increasing the electron current by orders of magnitude. This way, both, trap-free hole and electron transport can be accomplished, opening up a path toward large band gap organic semiconductors with balanced charge transport for efficient OLEDs.

The following chapter is based on:

O. Sachnik, X. Tan, D. Dou, C. Haese, N. Kinaret, K.-H. Lin, D. Andrienko, M. Baumgarten, R. Graf, G.-J. A. H. Wetzelaer, J. J. Michels, P. W. M. Blom, Elimination of charge-carrier trapping by molecular design, Nat. Mater. 2023, 22, 1114–1120.

Author contributions:

Oskar Sachnik synthesized the CzTRZ-based molecules and performed electrical characterization. Xiao Tan carried out electrical characterization. Naomi Kinaret and Kun-Han Lin performed the computational modelling. Constantin Haese and Robert Graf performed the Solid-State-NMR experiments. Denis Andrienko supervised the computational work, Jasper. J. Michels. supervised the synthetic work, Gert-Jan A. H. Wetzelaer supervised the electrical characterization and Paul W.M. Blom initiated and supervised the overall project and wrote the manuscript with input from the others.

2.1 Introduction

Organic semiconductors often exhibit relatively poor charge transport properties as compared to their inorganic counterparts. There are two fundamental reasons limiting their charge transport: the first one is a low carrier mobility, arising from the fact that organic molecules are held together by weak van der Waals and π–π non-covalent forces, making them susceptible to energetic and structural disorder. As a result, the charge transport is governed by hopping between localized states, which is less efficient than band conduction in crystalline inorganic semiconductors.[1] In the last three decades, by optimizing the molecular packing mobility values exceeding 10 $cm^2 V^{-1} s^{-1}$ for both *n*- and *p*-type organic semiconductors have been reported.[2,3] A second reason leading to poor charge transport, even for high mobility materials, is trapping of charge carriers by impurities. In this case, only a small fraction of the injected carriers contributes to the charge transport. Trapping of either electrons or holes is the main cause of unbalanced transport in organic semiconductors.[4,5] Recently, an energy window was identified inside which organic semiconductors are not susceptible to charge trapping. Trap-free bipolar charge transport can be accomplished when the electron affinity (EA) of the organic semiconductor is higher than 3.5 eV and the ionization energy (IE) is lower than 6.0 eV.[6] This universal window, which applies to semiconducting polymers as well as to small molecules, indicates that the extrinsic charge traps in organic semiconductors share a common origin. Electron trapping has been attributed to oxygen related impurities, whereas hole traps are linked to water clusters.[6–8] Furthermore, next to oxygen also omnipresent water has been proposed as a possible source for electron trapping.[9] However, the relation between processing conditions and trapping is still under debate.

The fundamental question remains whether it is possible to achieve intrinsic trap-free transport of both electrons and holes for organic semiconductors with a band gap larger than the trap-free window of 2.5 eV. In that case, either the highest occupied molecular orbital (HOMO) or lowest unoccupied molecular orbital (LUMO) or both are outside the trap-free window. Since trapping is detrimental to the efficiency of single-layer OLEDs trap-free ambipolar charge transport is a prerequisite to achieve highly efficient devices.[10–12] The limited width of 2.5 eV of the energy window implies that for large band gap materials, as used in blue OLEDs, it is fundamentally not possible to obtain trap-free transport of both carriers, thus preventing the realization of efficient printed single-layer blue OLEDs in future. In addition, for multilayer blue OLEDs, the imbalance in electron and hole transport in the large band gap host leads to an unevenly distributed emission zone as well as to unwanted interactions of excess holes with excitons, which decrease the operational lifetime of the device.[13–15]

Here, an approach is demonstrated how simultaneous trap-free electron and hole transport can be intrinsically accomplished in wide bandgap organic semiconductors through molecular design. The basic idea is to use donor-acceptor based molecules, with the LUMO localized on the acceptor part and

the HOMO localized on the donor part. By shielding the acceptor core where the electron transport takes place with the donor moieties, the interaction of impurities with the LUMO leading to electron trapping can be effectively blocked. This work therefore represents a universal molecular bottom-up concept to eliminate the detrimental effects of external impurities in organic semiconductors.

2.2 Results and Discussion

The basic structure of a series of blue-emitting molecules presented in this study consists of a triazine (TRZ) acceptor linked to carbazole (Cz) donor(s) by a phenylene linker (**Figure 2.1**). Triazene based materials are well known for their efficient transport of electrons.[16] A similar combination of triazine and carbazole has been employed as blue emitter exploiting thermally activated delayed fluorescence, where it was demonstrated that an increase of the amount of Cz donor units from two to three led to an enhancement of the OLED efficiency.[17] However, the individual charge transport properties of these CzTRZ based materials were not addressed. A series of organic semiconducting blue emitters have been synthesized (**Figure 2.1**) and were investigated in terms of electron transport and molecular arrangement in thin films. The first series of blue emitters share the same triazine acceptor but a different number of donating carbazole units (bridged by a phenylene linker): 9-(4-(4,6-diphenyl-1,3,5-triazin-2-yl)-2,6-dimethylphenyl)-9*H*-carbazole (1CzTRZ), 9,9'-(5-(4,6-diphenyl-1,3,5-triazin-2-yl)-1,3-phenylene)bis(9*H*-carbazole) (2CzTRZ), 9,9',9''-(5-(4,6-diphenyl-1,3,5-triazin-2-yl)benzene-1,2,3-triyl)tris(9*H*-carbazole) (3CzTRZ), 9,9',9'',9'''-(3-(4,6-diphenyl-1,3,5-triazin-2-yl)benzene-1,2,4,5-tetrayl)tetrakis(9*H*-carbazole) (4CzTRZ) and 9,9',9'',9''',9''''-(6-(4,6-diphenyl-1,3,5-triazin-2-yl)benzene-1,2,3,4,5-pentayl)pentakis(9*H*-carbazole) (5CzTRZ).

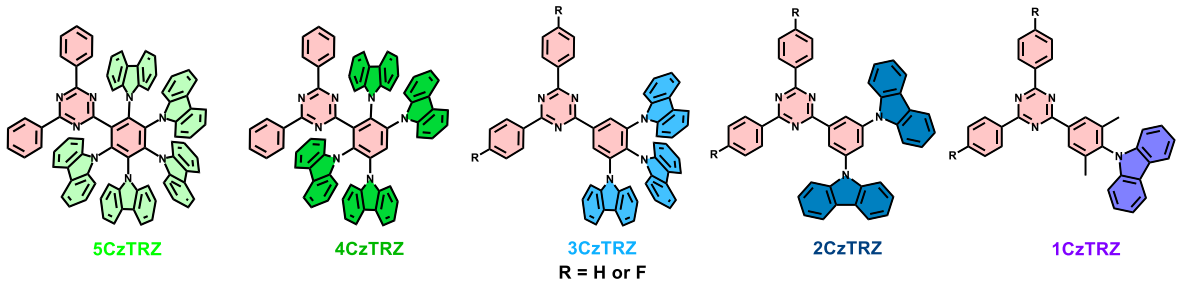

Figure 2.1. Molecular structures. Structural formulas of 1CzTRZ, 2CzTRZ, 3CzTRZ, 4CzTRZ and 5CzTRZ.

First, the ionization energy (IE) and electron affinity (EA) of the five 1-5CzTRZ compounds using a combination of ultraviolet photoelectron spectroscopy (UPS) (**Figure 2.2a**), cyclic-voltammetry (CV) measurements (**Figure A2.1**) and solution UV-Vis absorption and photoluminescence (PL) measurements (**Figure 2.2b** and **c**) were measured.

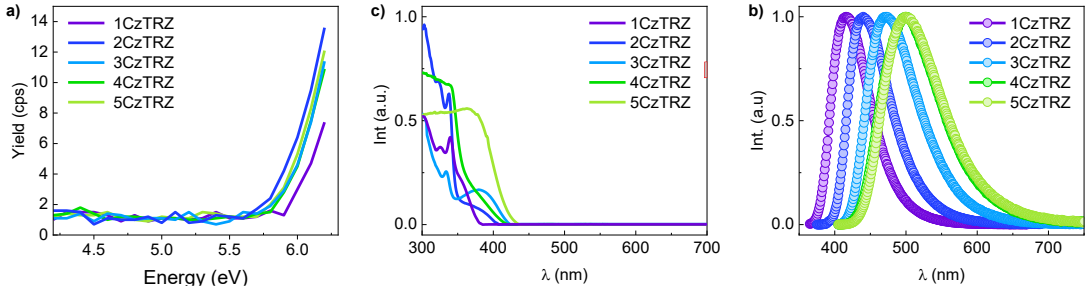

Figure 2.2. a) Photoemission yield spectroscopy in air of 1CzTRZ, 2CzTRZ, 3CzTRZ, 4CzTRZ, 5CzTRZ. Steady-state UV-Vis spectra b) and photoluminescence spectra c) in solution (toluene 1×10^{-5} M) of 1CzTRZ, 2CzTRZ, 3CzTRZ, 4CzTRZ and 5CzTRZ.

The IE of this series of molecules of ~5.8 eV is within the trap-free energy window, meaning that trap-free hole transport is expected for all of these compounds.[6] The measured EA (**Table 2.1**) amounts to 3.1 ± 0.1 eV for all compounds, clearly well below the value of 3.6 eV for trap-free electron transport.[6] Hence, in contrast to the hole current, the electron current is expected to be strongly trap-limited in *all cases* based on energy-level considerations.

Table 2.1. Experimental IE (UPS, CV) and EA (CV).

	1CzTRZ (-F)	2CzTRZ (-F)	3CzTRZ (-F)	4CzTRZ	5CzTRZ
IE from UPS (eV)	5.90 (5.95)	5.73 (5.56)	5.81 (5.90)	5.82	5.81
IE from CV (eV)	5.82 (5.61)	5.78 (5.80)	5.84 (5.67)	5.43	5.84
EA from CV (eV)	3.01 (2.84)	3.12 (3.12)	3.28 (3.11)	3.05	3.15

Subsequently, the electron transport in the emitters 1CzTRZ – 5CzTRZ using electron-only (EO) devices was investigated. Details are explained in the experimental chapter. In **Figure 2.3a**, the measured (symbols) electron current density (J) as a function of voltage (V) for the 1-5CzTRZ series is displayed. The thickness of the investigated devices is in the range of 80-100 nm. Despite the fact that all molecules comprise the same donor and acceptor moieties, a four to five orders of magnitude difference in the electron current density is observed, depending on the number of donor substituents. Intriguingly, the electron current in 3CzTRZ shows a quadratic dependence of the current on voltage, indicative of trap-free space-charge-limited electron transport, despite having its LUMO energy outside the trap-free window. The fact that the lower current density for the other compounds is accompanied by an increased voltage dependence of the current indicates that the strong reduction in transport is caused by electron trapping.[4]

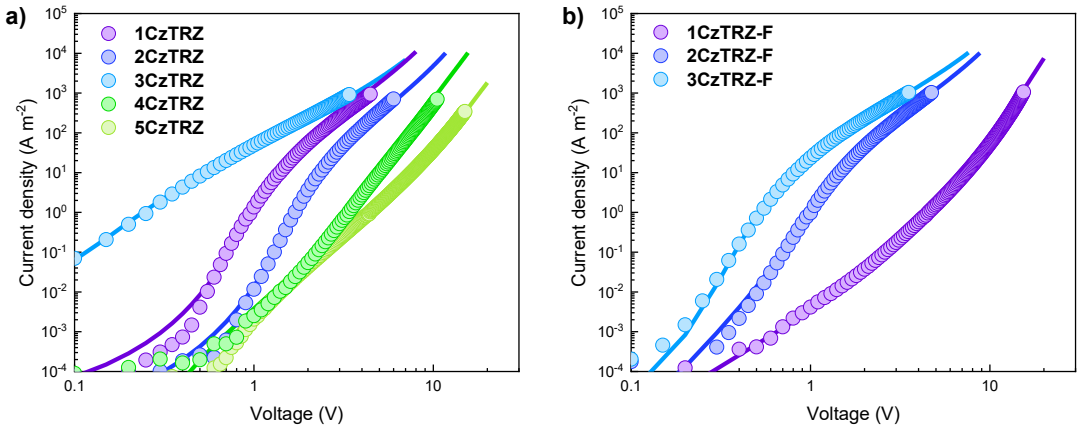

Figure 2.3. Electron current of CzTRZ and based compounds. a) Experimental (symbols) and simulated (lines) current density (*J*)- voltage (*V*) characteristics of 1CzTRZ (94 nm), 2CzTRZ (100 nm), 3CzTRZ (98 nm), 4CzTRZ (79 nm) and 5CzTRZ (102 nm). b) Experimental (symbols) and simulated (lines) current density (*J*)- voltage (*V*) characteristics of the fluorinated compounds 3CzTRZ-F (118 nm), 2CzTRZ-F (91 nm) and 1CzTRZ-F (95 nm).

Similar behavior occurs for the fluorinated 1-3CzTRZ-F series: the EAs as obtained from CV measurements (**Table 2.1**) range from 2.8 – 3.1 eV, and are all far outside the trap-free window. However, as shown in **Figure 2.3b**, also for this series the compound with 3 Cz units 3CzTRZ-F exhibits nearly trap-free electron transport, whereas the electron current of 1CzTRZ-F is strongly reduced, showing a steep *J-V* curve with a slope of around six in the log(*J*)-log(*V*) plot. For both series an optimum electron current is reached for three Cz units, for which a nearly trap-free space-charge limited current ($J \sim V^2$) is measured. A further decrease or increase in the number of Cz moieties results in more severe electron trapping. To quantify the trap density, the *J-V* characteristics are modeled (lines, **Figure 2.3**) with a previously developed drift-diffusion model.[18] The electron mobility is obtained from the quadratic trap-free regime observed for the 3CzTRZ molecule and amounts to 2×10^{-9} m^2 V^{-1} s^{-1}. The currents of the other compounds are then described by the addition of electron traps, assuming a Gaussian energy distribution of trap states[18]. The trap concentrations for the 1-5CzTRZ compounds are given in **Table 2.2**.

Table 2.2. Calculated electron trap densities.

	1CzTRZ	2CzTRZ	3CzTRZ	4CzTRZ	5CzTRZ
Trap density (m^{-3})	6.0×10^{22}	8.0×10^{22}	0.24×10^{22}	6.0×10^{23}	2.8×10^{24}

By studying the dependence on layer thickness and temperature it was confirmed that the observed difference of orders of magnitude in the electron current is not the result of a variation in injection barrier or built-in voltage V_{bi} (**Figure A2.2-A2.4**). Ohmic contacts have been realized by using a 1,3,5-tris(1-phenyl-1*H*-benzo[d]imidazol-2-yl)benzene, (TPBi) tunnel barrier to decouple the semiconductor from the electrode.[19]

To obtain more insight in the molecular mechanism of trapping, as a next step, the density of states (DOS) of the five 1-5CzTRZ and three 1-3CzTRZ-F compounds were computed, assuming the films to be amorphous (disordered molecular arrangement), with traps due to molecular oxygen. For computational details, see the original publication. The calculated ionization energies (**Table A2.3**) agree well with the experimentally obtained numbers (**Table 2.1**). The DOS distribution of the electron affinity (EA) of molecular oxygen and *amorphous* 1-5CzTRZ (LUMO) show that, as expected, the value of the EA increases with increasing number of carbazoles from 1CzTRZ to 3CzTRZ (**Figure 2.5**). Since the EA distributions of O_2 are not significantly different, the increased EA results in reduced trapping. Further increase of the number of carbazoles (4-5CzTRZ) results in lower EA and enhanced trapping (see also **Table A2.3**), which agrees with the trend of trap densities obtained from the drift-diffusion model (**Table 2.2**). In contrast, for the fluorinated 1-3CzTRZ-F compounds the value of EA and distributions of O_2 do not significantly vary, such that identical trapping is expected for all compounds (**Table A2.5, A2.6**). This is clearly in contrast with the strong variation in electron current, shown in **Figure 2.3b**. This suggests that it is not only the energetics of the molecules being responsible for the observed large variation in electron transport of the various CzTRZ based compounds. An open question is whether extrinsic electron trapping is also strongly dependent on the molecular arrangement of the molecules in the solid film. Of course, this can only be the case if the films are not fully amorphous, but rather exhibit molecular ordering to some extent, for instance in a coexisting phase comprising (nano-)crystalline domains.[20,21]

To investigate the molecular ordering in the compounds with three or fewer carbazole units, the fluorinated mono- and tricarbazole species were subjected to a comparative analysis using two complementary experimental methods, namely x-ray diffraction (XRD) and magic angle spinning (MAS) solid-state NMR (SS-NMR).[22,23] XRD was applied to single crystals, grown by anti-solvent diffusion as described in the Material and Methods section. The SS-NMR analysis was used to establish the extent of ordering in the evaporated thin film. The reason to select the 1CzTRZ-F and 3CzTRZ-F for this analysis is that the fluorine substituent provides for a highly sensitive marker, owing to the fact that its natural isotope (^{19}F) has spin $+1/2$.[24] Furthermore, the 1CzTRZ-F and 3CzTRZ-F exhibit a few orders of magnitude difference in their electron transport, with the transport in 1CzTRZ-F heavily trap-limited and a nearly trap-free transport in 3CzTRZ-F. Additionally, it was possible to grow crystals of sufficient quality for XRD of both 1CzTRZ-F and 3CzTRZ-F compounds.

To characterize the structure of the single crystals, XRD analysis (see for details **Table A2.7**) revealed the space group for 1CzTRZ-F to be P1 (monoclinic), with no co-crystallized solvent molecules. As displayed in **Figure 2.4a** and **b**, the unit cell contains four molecules, paired into two dimers with antiparallel stacking of the triazine planes and significant spatial overlap between the outer phenyl groups. The distance between the molecular planes is 3.5 Å. The carbazole units are arranged in an angle close to 90° relative to the connecting phenyl ring, caused by the steric hindrance of the two ortho-methyl groups.

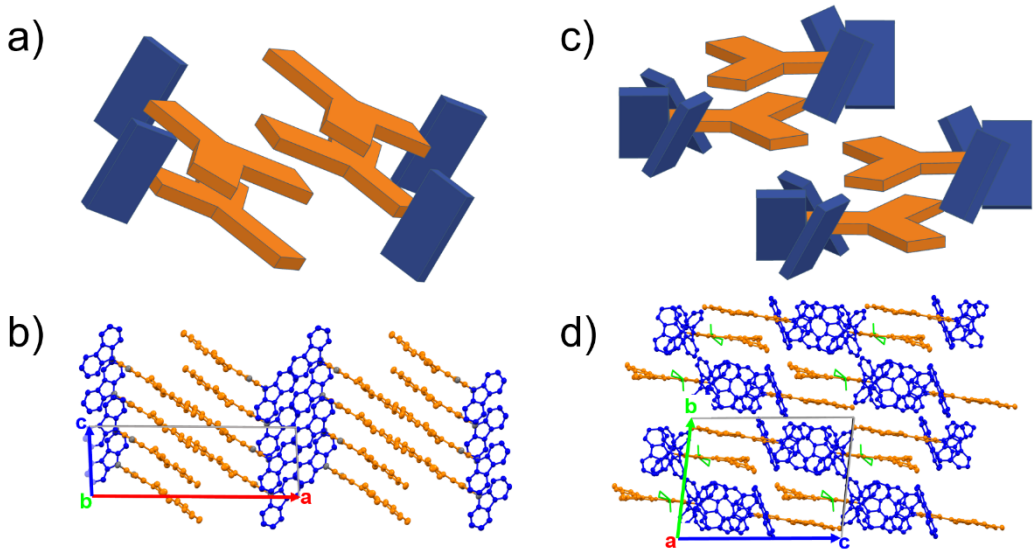

Figure 2.4. Molecular structures obtained from XRD. a,b,c,d, Crystal structures of the 1CzTRZ-F (a, b) and 3CzTRZ-F (c, d) compounds, determined by XRD. For a better visualization of the molecular packing, the two dimers of both crystallographic unit cells are draws schematically in a) and c). In b) and d), the triazine acceptor and the carbazole donor units are colored according to the schematic drawing a) and c) to illustrate the spatial arrangement of the acceptor-donor contacts in the 3-dimensional crystal structure. The green features in d) indicate co-crystallized chloroform molecules.

Furthermore, as shown in **Figure 2.4a**, the Cz units of the species within one dimer are rotated relative to each other by approximately 60° around the centers of the triazine rings. The three-dimensional arrangement leads to a structure with alternating two-dimensional layers of carbazole and triazine rings perpendicular to the crystallographic a-axis. Dimer formation agrees with earlier work by Monkman et al. who demonstrated that dimers are responsible for the spectral shifts observed in carbazole based TADF emitters.[25] The 3CzTRZ-F crystal structure falls in the $P2_1/c$ space group (triclinic), exhibiting solvent co-crystallization. Again, four molecules in a single unit cell (see **Figure 2.4c** and **d**) are encountered, exhibiting a dimeric arrangement. However, now the dimers are formed by antiparallel molecular alignment and the stacking involves not only the triazine rings, but also the outer phenyl

rings. The torsion angles of the carbazole groups are 120±10°, possibly resulting from weak π-π interaction of neighboring units bound to the same phenyl ring. The stacking of neighboring molecules is slightly tilted and the π systems of adjacent molecules do not perfectly superimpose. The stacking of neighboring molecular planes, however, connects molecules within a plane, forming a one-dimensional double layer of acceptor units along the crystallographic a-axis. The distance between the molecular planes is 3.4 Å. In summary, 3CzTRZ-F shows an inclined face-to-face stacking of the phenyl substituted triazine cores along the crystallographic a-axis, which effectively may act as a "tunnel" for electron transport, crowded by carbazole units. In contrast, in 1CzTRZ-F such crowding is lacking. It is therefore proposed that the origin of the difference in the electron trapping between the mono- and tricarbazole carbazole species is the result of the stacking geometry: "open" for the monocarbazole species and "closed" for the tricarbazole compounds, meaning that in the latter the electron transporting core is effectively shielded from interactions with extrinsic contaminants such as oxygen.

In what follows, MAS SS-NMR was used to confirm that molecular ordering indeed occurs in vapor deposited material, supporting our explanation of differences in electron transport in terms of differences in molecular packing. The spectra of 1CzTRZ-F (^{1}H and ^{19}F) and 3CzTRZ-F (^{1}H and ^{19}F) are plotted in **Figure A2.8**. For 1CzTRZ-F the ^{19}F signal is split despite the symmetry in the molecular structure (**Figure A2.8a**). This demonstrates that there is a preferred local molecular packing arrangement that breaks the molecular symmetry of the two ^{19}F sites in the molecule. In a random or fully amorphous arrangement, there should be as well molecules where the molecular symmetry is preserved and then only a single very broad peak should be seen. Similar as for 1CzTRZ also in the ^{19}F MAS NMR spectrum of the 3CzTRZ-F (**Figure A2.8b**) compounds two signals are observed, again pointing to a difference in the local chemical environment between the two ^{19}F sites.

Having established that there is a local ordering in the films it is evident that the theoretical interpretation based on the amorphous phase of 1-5CzTRZ (**Figure A2.6**) and 1-3CzTRZ-F (**Figure A2.7**) should be handled with care, since the impact of molecular packing is not captured by these simulations. For this purpose, the DOS of the crystalline phases was simulated, using the structural data obtained from XRD for 1CzTRZ-F and 3CzTRZ-F (**Figure 2.4**). As shown in **Figure 2.5**, the EA distributions of oxygen are quite similar in crystalline and amorphous 3CzTRZ-F. In contrast, for 1CzTRZ-F the oxygen EAs are much higher in the crystalline phase than in the amorphous phase, implying deeper traps. Considering the fact that there are regions in organic thin films with molecular packing resembling the crystalline state, the deep O_2 traps (**Table A2.6**) in crystalline 1CzTRZ-F result in a higher overall trap density as compared to 3CzTRZ-F, which agrees with the trend of trap densities obtained from the drift-diffusion model (**Table A2.2**).

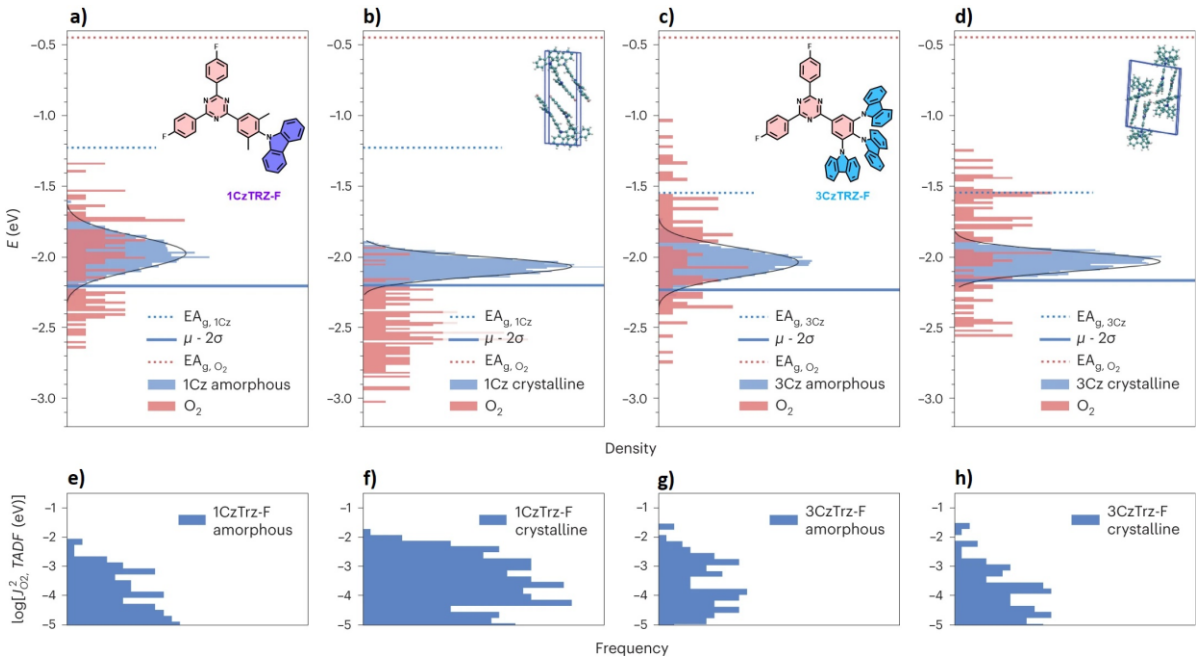

Figure 2.5. Calculated density-of-states distributions. a,b,c,d, The density of states of electron affinity of (a) amorphous 1CzTRZ-F, (b) crystalline 1CzTRZ-F, (c) amorphous 3CzTRZ-F, and (d) crystalline 3CzTRZ-F. e,f,g,h, Magnitude of electronic transfer integral vs. occurrence frequency in (e) amorphous 1CzTRZ-F, (f) crystalline 1CzTRZ-F, (g) amorphous 3CzTRZ-F, and (h) crystalline 3CzTRZ-F, respectively. The dotted lines are the gas-phases electron affinity for molecular oxygen and organic materials. The blue solid line represents the energy μ_e -2σ_e, with μ_e corresponding to the average of the calculated solid-state EA values and σ_e the standard deviation of the Gaussian distribution, respectively (**Table A2.5**), The energy μ_e -2σ_e is expected to correspond to the onset of the solid-state EA from UPS measurements.

However, as shown in **Figure 2.5c** and **d** energetic considerations alone cannot account for the trap-free transport observed in 3CzTRZ-F. This clearly suggests that the molecular packing is also an essential ingredient to obtain a trap-free current due to shielding of the electron transporting core from impurities by the stacking geometry. To further elucidate the effectiveness of the O_2 traps in the 1CzTRZ-F and 3CzTRZ compounds the electronic transfer integrals representing the coupling between close lying oxygen and CzTRZ-F pairs (**Figure 2.5e-h**) were evaluated. It is demonstrated that the total coupling strength, represented by the area under the histogram, is largest in the 1CzTRZ-F crystalline phase, thereby stabilizing the oxygen and resulting in oxygen becoming a deeper and more effective trap in the crystalline 1CzTRZ-F.

To put the trap-free electron transport in 3CzTRZ further in perspective, in **Figure 2.6** the electron and hole current for 3CzTRZ are shown, together with the electron current of 1,3,5-tris(1-phenyl-1*H*-benzo[d]imidazol-2-yl)benzene, TPBi, a state-of-the-art electron transport material (ETM) used in multilayer OLEDs and perovskite based LEDs.[26,27]

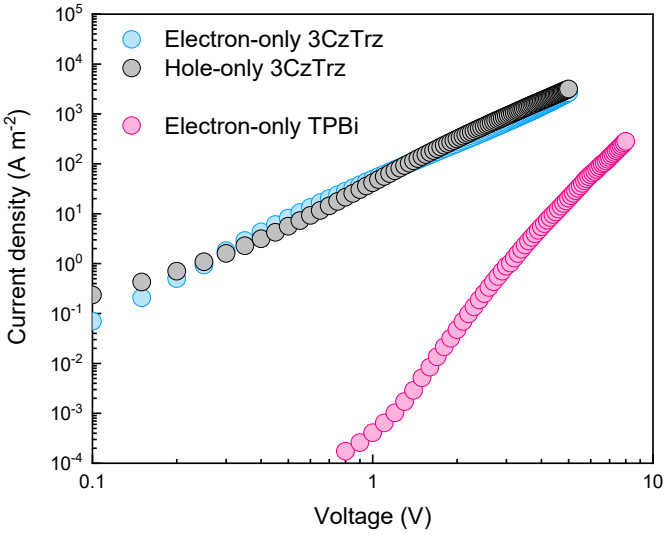

Figure 2.6. Electron and hole current in 3CzTRZ and electron current in TPBi. Current density (*J*) - voltage (*V*) characteristics of electron- and hole-only devices of 3CzTRZ and TPBi. The active layer thickness in each device is 100 nm.

2.3 Conclusion

For 3CzTRZ not only both the electron and hole current of 3CzTRZ are nearly trap-free but also balanced in charge-carrier mobility, which amounts to 2×10^{-9} m^2 V^{-1} s^{-1}. In terms of electron transport 3CzTRZ clearly outperforms TPBi. **Figure 2.6** shows that, due to trapping, the electron current in TPBi is more than two orders of magnitude lower compared to the trap-free 3CzTRZ material. To the best of our knowledge, this is the first report showing large bandgap organic semiconductors with balanced and trap-free electron and hole transport. In conclusion, a bottom-up molecular strategy is presented to avoid trapping of charge carriers by extrinsic impurities in wide band gap organic semiconductors. By using donor-acceptor based molecules, the HOMO and LUMO orbitals can be spatially separated and arranged by chemical design. An optimized molecular packing then enables a steric shielding of the electron transporting acceptor units. This shielding strongly reduces the vulnerability of the semiconductor with regard to extrinsic impurities such as oxygen that cause electron trapping in organic semiconductors with low electron affinity, even up to the level of fully trap-free transport. This work therefore represents a molecular concept to eliminate the detrimental effects of external impurities in organic semiconductors.

References

[1] H. Bässler, *Phys. Status Solidi* **1993**, *175*, 15.

[2] J. L. Brédas, J. P. Calbert, D. A. Da Silva Filho, J. Cornil, *Proc. Natl. Acad. Sci. U. S. A.* **2002**, *99*, 5804.

[3] G. Schweicher, G. Garbay, R. Jouclas, F. Vibert, F. Devaux, Y. H. Geerts, *Adv. Mater.* **2020**, *32*.

[4] H. T. Nicolai, M. Kuik, G. A. H. Wetzelaer, B. De Boer, C. Campbell, C. Risko, J. L. Brédas, P. W. M. Blom, *Nat. Mater.* **2012**, *11*, 882.

[5] H. F. Haneef, A. M. Zeidell, O. D. Jurchescu, *J. Mater. Chem. C* **2020**, *8*, 759.

[6] N. B. Kotadiya, A. Mondal, P. W. M. Blom, D. Andrienko, G. J. A. H. Wetzelaer, *Nat. Mater.* **2019**, *18*, 1182.

[7] J. M. Zhuo, L. H. Zhao, R. Q. Png, L. Y. Wong, P. J. Chia, J. C. Tang, S. Sivaramakrishnan, M. Zhou, E. C. W. Ou, S. J. Chua, W. S. Sim, L. L. Chua, P. K. H. Ho, *Adv. Mater.* **2009**, *21*, 4747.

[8] M. Nikolka, K. Broch, J. Armitage, D. Hanifi, P. J. Nowack, D. Venkateshvaran, A. Sadhanala, J. Saska, M. Mascal, S. H. Jung, J. K. Lee, I. McCulloch, A. Salleo, H. Sirringhaus, *Nat. Commun.* **2019**, *10*, 1.

[9] G. Zuo, M. Linares, T. Upreti, M. Kemerink, *Nat. Mater.* **2019**, *18*, 588.

[10] B. Van der Zee, Y. Li, G. J. A. H. Wetzelaer, P. W. M. Blom, *Adv. Mater.* **2022**, *34*, 2108887.

[11] N. B. Kotadiya, P. W. M. Blom, G. J. A. H. Wetzelaer, *Nat. Photonics* **2019**, *13*, 765.

[12] D. Abbaszadeh, A. Kunz, G. A. H. Wetzelaer, J. J. Michels, N. I. Craciun, K. Koynov, I. Lieberwirth, P. W. M. Blom, *Nat. Mater.* **2016**, *15*, 628.

[13] L. S. Cui, J. U. Kim, H. Nomura, H. Nakanotani, C. Adachi, *Angew. Chemie - Int. Ed.* **2016**, *55*, 6864.

[14] Y. Chen, X. Wei, Z. Li, Y. Liu, J. Liu, R. Wang, P. Wang, Y. Yamada-Takamura, Y. Wang, *J. Mater. Chem. C* **2017**, *5*, 8400.

[15] Q. Niu, R. Rohloff, G. J. A. H. Wetzelaer, P. W. M. Blom, N. I. Crăciun, *Nat. Mater.* **2018**, *17*, 557.

[16] H. F. Chen, S. J. Yang, Z. H. Tsai, W. Y. Hung, T. C. Wang, K. T. Wong, *J. Mater. Chem.* **2009**, *19*, 8112.

[17] D. R. Lee, M. Kim, S. K. Jeon, S. H. Hwang, C. W. Lee, J. Y. Lee, *Adv. Mater.* **2015**, *27*, 5861.

[18] L. J. A. Koster, E. C. P. Smits, V. D. Mihailetchi, P. W. M. Blom, *Phys. Rev. B - Condens. Matter Mater. Phys.* **2005**, *72*, 1.

[19] N. B. Kotadiya, H. Lu, A. Mondal, Y. Ie, D. Andrienko, P. W. M. Blom, G. J. A. H. Wetzelaer, *Nat. Mater.* **2018**, *17*, 329.

[20] R. Noriega, J. Rivnay, K. Vandewal, F. P. V. Koch, N. Stingelin, P. Smith, M. F. Toney, A. Salleo, *Nat. Mater.* **2013**, *12*, 1038.

[21] G. Han, Y. Guo, X. Song, Y. Wang, Y. Yi, *J. Mater. Chem. C* **2017**, *5*, 4852.

[22] M. Seifrid, G. N. M. Reddy, B. Chmelka, G. Bazan, M. Seifrid, G. N. M. Reddy, B. Chmelka, G. Bazan, **2023**.

[23] D. M. Delongchamp, R. J. Kline, D. A. Fischer, L. J. Richter, M. F. Toney, *Adv. Mater.* **2011**, *23*, 319.

[24] R. K. Harris, P. Jackson, *Chem. Rev.* **1991**, *91*, 1427.

[25] M. K. Etherington, N. A. Kukhta, H. F. Higginbotham, A. Danos, A. N. Bismillah, D. R. Graves, P. R. McGonigal, N. Haase, A. Morherr, A. S. Batsanov, C. Pflumm, V. Bhalla, M. R. Bryce, A. P. Monkman, *J. Phys. Chem. C* **2019**, *123*, 11109.

[26] Q. Zhang, B. Li, S. Huang, H. Nomura, H. Tanaka, C. Adachi, *Nat. Photonics* **2014**, *8*, 326.

[27] C. Zou, Y. Liu, D. S. Ginger, L. Y. Lin, *ACS Nano* **2020**, *14*, 6076.

3. Blue single-layer organic light-emitting diodes with near-unity internal efficiency

Typically, efficient organic light-emitting diodes comprise a multilayer stack including several charge-transport and charge and exciton-blocking layers. These layers are incorporated to confine excitons within the emissive layer, forcing their emissive deactivation. In this chapter, a simplified and highly efficient (approaching near-unity) single-layer blue-emitting OLED based on thermally activated delayed fluorescence is demonstrated. This is achieved through the use of an ohmic polymeric anode and an ohmic metallic cathode. The polymeric anode is based on PEDOT:PSS, a commonly used hole-contact material in organic light-emitting diodes, organic photovoltaics and field-effect transistors. Through modification of the PEDOT:PSS anode, a simply applicable hole-contact with a work function of up to 5.9 eV is created, rendering it practically ohmic (barrier-free) for a variety of organic semiconductors.

The following chapter is based on:
O. Sachnik, Y. Li, X. Tan, J. J. Michels, P. W. M. Blom, G. A. H. Wetzelaer, Single-Layer Blue Organic Light-Emitting Diodes With Near-Unity Internal Quantum Efficiency, Adv. Mater. 2023, 35, 2300574.

Author contributions:
Oskar Sachnik performed the synthesis of materials, PEDOT:PSS modifications, device fabrication, electrical measurements, collected the data and prepared all figures. Xiao Tan performed the optical measurements. Yungui Li performed the optical simulations. Gert-Jan Wetzelaer performed the EGDM simulations. Oskar Sachnik and Gert-Jan Wetzelaer wrote the manuscript with input from Paul. W. M. Blom. Jasper J. Michels, Paul. W. M. Blom and Gert-Jan Wetzelaer supervised the project.

3.1 Introduction

The first demonstration of electroluminescence in organic materials has driven the research of optoelectronic devices, such as organic light-emitting diodes (OLEDs), paving the way to mass-commercialization in display and lightning applications.[1] Early OLEDs employed a simple device structure by sandwiching the semiconducting layer between two electrodes, injecting holes into the organic semiconductor layer via the anode and electrons via the cathode. These countercharges are then transported through the organic semiconductor, where they meet and recombine via exciton formation and subsequent radiative decay, resulting in visible light emission. After the first demonstrations of electroluminescence in these simple OLEDs, considerable efficiency gains were made by increasing the number of functional layers and by harvesting triplet excitons.[2–6]

In these multilayer OLEDs, the light-emitting layer is surrounded by several charge-transport and charge- and exciton-blocking layers. By selecting materials with suitable charge-transport properties and appropriate energy levels for charges and excitons, these additional layers are used to transport charges to the emissive layer, in which charges and excitons are confined with the help of blocking layers.[2] As such, it is ensured that all charges and excitons recombine and decay within the emissive layer to maximize the internal quantum efficiency of the conversion of charges into photons. In addition, the emissive layer can be optimally positioned within the multilayer stack to reach maximum light outcoupling, thereby maximizing the external quantum efficiency (EQE). Typical maximum outcoupling efficiencies for multilayer OLEDs are in the 20% to 30% range, being the main limiting factor in the EQE of state-of-the-art multilayer OLEDs.[7,8]

However, a major drawback of multilayer OLEDs is their complexity in terms of design, fabrication, and interpretation. The additional transport and blocking layers have very specific requirements regarding energy levels, energy gap, and triplet energy, in order to minimize charge-injection barriers and enhance charge and exciton-blocking capabilities. This makes the design of a multilayer OLED cumbersome and induces additional fabrication steps, which drives up the costs. Furthermore, the additional heterojunctions frequently induce additional energy barriers and thus voltage losses, and these interfaces may be potential sources of device degradation. It is generally accepted that such complex device structures are required to achieve high EQEs in the 20-30% range.[9,10] This then basically would rule out the realization of efficient OLEDs with a highly simplified structure consisting of a single emissive layer sandwiched between two electrodes, similar to the early OLEDs. Such a simplified structure is a prerequisite for solution-processed OLEDs due to stack integrity issues. A fundamental question therefore is what the maximum attainable efficiency in OLEDs with a simplified device structure would be and how it compares to the complex multilayer devices.

Recently, an efficient OLED with simplified device structure based on a yellow thermally activated delayed fluorescence (TADF) emitter has been demonstrated.[11] In this OLED, the TADF emitter was sandwiched between two ohmic contacts, without any charge-transport or blocking layers. The ohmic contacts, however, required the presence of tunneling interlayers, consisting of organic-semiconductor layers of a few nanometers thick. Although the requirements for these thin interlayers in terms of energy levels and triplet energies are far less elaborate than for conventional charge-transport layers, coating steps are still required to deposit these interlayers.[12] Not only is this suboptimal for vacuum-deposited OLEDs, but it would be an additional hurdle to overcome when aiming for fully solution-processed OLEDs.

For blue single-layer OLEDs, direct charge injection into the emitter via ohmic contacts becomes particularly challenging, since blue emitters have a large energy gap of around 3 eV. For emitters with a high ionization energy, efficient hole injection can be achieved with a combination of a high work function transition-metal oxide and a suitable tunneling interlayer, which, however, involves two vacuum-based deposition steps[12]. An alternative approach to achieve a high work function contact is to blend perfluorinated ionomers (PFI) with the conducting polymer PEDOT:PSS, which enhances the film work function up to 5.9 eV, as a result of the formation of a surface dipole, induced by a thin fluorine-rich overlayer.[13,14] Although higher efficiencies were reported for OLEDs containing PFI-modified hole-injection layers, as compared to standard PEDOT:PSS, it has been suggested that despite the high work function, these contacts are non-ohmic.[15,16] Direct evidence of the formation of an ohmic hole contact between PEDOT:PSS:PFI and high ionization energy (IE) organic semiconductors has indeed not been presented to date. Ohmic contacts are, however, of paramount importance for single-layer OLEDs to operate efficiently.

In this chapter, it is demonstrated that a blend film containing PEDOT:PSS and PFI in fact can provide ohmic hole injection into high-IE organic semiconductors. Subsequently, a single-layer blue-emitting TADF OLED is presented, with the use of a spin-coated PFI-modified hole contact and a metal cathode. It is demonstrated that the presence of a host in the emissive layer eliminates the need for an organic tunneling interlayer for ohmic electron injection. The device shows an external quantum efficiency of up to almost 28%, which equates to practically unity internal quantum efficiency when considering losses due to optical outcoupling, despite the absence of a charge- and exciton-confinement structure. Therefore it is shown that highly simplified, single-layer OLEDs with zero electrical losses are a feasible alternative to state-of-the-art multilayer devices.

3.2 Results and Discussion

As a first step, ohmic hole injection from PEDOT:PSS:PFI into a high-IE organic semiconductor is demonstrated. The most direct way to demonstrate an ohmic hole contact, is the fabrication of a hole-only device with one of the contacts as an ohmic reference. In **Figure 3.1**, the current density-voltage characteristics of a hole only device of (9,10-bis(4-(9*H*carbazol-9-yl)−2,6-dimethylphenyl)−9,10-diboraanthracene (CzDBA) is displayed. CzDBA has a high IE of 5.93 eV.[17] The hole-only device consists of a PEDOT:PSS:PFI (1:6:14 by wt.) bottom contact and a C_{60}(4 nm)/MoO_3(10 nm)/Al top electrode. This top electrode has been shown to provide ohmic hole injection into a variety of organic semiconductors, including CzDBA, and is therefore an ideal reference.[11,12]

As shown in **Figure 3.1**, symmetric *J-V* characteristics are observed, indicating that hole injection from PEDOT:PSS:PFI under forward bias is equally efficient to injection from the ohmic top electrode under reverse bias.

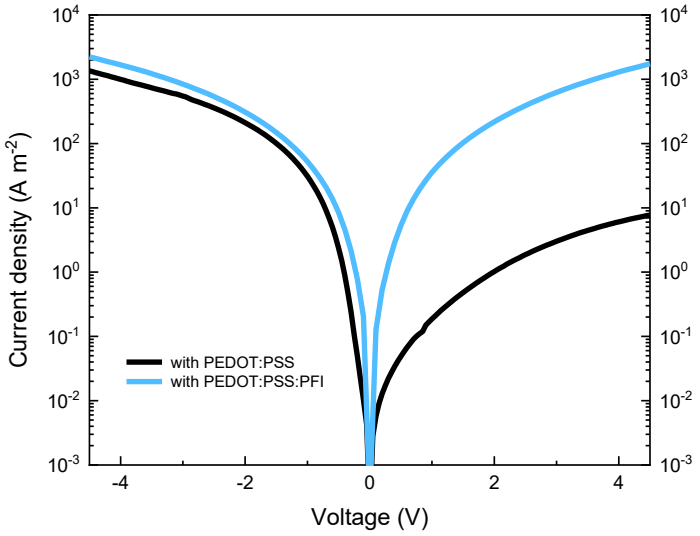

Figure 3.1. Ohmic hole injection from a PFI-modifed anode. Current density (*J*) vs voltage (*V*) characteristics of a hole-only device of CzDBA (80 nm) with a HIL/CzDBA/C_{60}/MoO_3/Al device structure where the hole-injection layer (HIL) is either PEDOT:PSS or PEDOT:PSS:PFI. At negative bias, current is injected from the ohmic C_{60}/MoO_3 top contact. Positive bias corresponds to hole injection from the bottom HIL. The symmetric *J-V* characteristic is indicative of ohmic hole injection from PEDOT:PSS:PFI, while the injected hole current from PEDOT:PSS is substantially reduced due to the injection barrier.

A control device with a standard PEDOT:PSS bottom contact shows an injected current that is more than two orders of magnitude lower as a result of the hole-injection barrier due to the work-function mismatch. The current under reverse bias is practically unaltered, indicating that the PEDOT:PSS:PFI layer does not give rise to additional electrical resistance. Therefore, it can be concluded that hole injection from PEDOT:PSS:PFI into CzDBA is ohmic. To further validate that a truly ohmic hole contact is formed with the simple PEDOT:PSS:PFI layer, a single-layer OLED of CzDBA was fabricated which reached an EQE of ~18% (Appendix, **Figure A3.1b**), which is close to the reported value of 19% for an ohmic MoO_3/C_{60} bottom contact, while exhibiting similarly low operating voltages.[11]

The demonstration of ohmic hole injection from PEDOT:PSS:PFI into a high-IE organic semiconductor shows promise for blue-emitting single-layer OLEDs. The fabrication of efficient blue-emitting OLEDs in general is challenging, because the wide energy gap of blue emitters complicates efficient charge injection. Furthermore, charge and exciton confinement in *multilayer* blue OLEDs requires wide-gap transport and blocking layers with high triplet energies, which makes material selection more cumbersome. In a single-layer OLED, these blocking and transport layers are absent, thereby greatly simplifying the device design.

To investigate the possibility of fabricating highly efficient blue-emitting OLEDs in a single-layer architecture, SpiroAc-TRZ (10-(4-(4,6-diphenyl-1,3,5-triazin-2-yl)phenyl)-10*H*-spiro[acridine-9,9'-fluorene] was chosen as a blue-emitting organic semiconductor, which exhibits TADF.[18] SpiroAc-TRZ has been successfully applied in multilayer OLEDs and has favorable properties, such as a high photoluminescence quantum yield of up to 100% and a highly horizontal dipole orientation when doped in a mCPCN (9-(3-(9*H*-carbazol-9-yl)phenyl)-9*H*-carbazole-3-carbonitrile) host matrix.[18,19] The mCPCN host has a larger band gap and higher triplet energy than the SpiroAc-TRZ emitter, and in the chosen host-to-guest ratio of 1:1, charge transport is expected to be solely taking place on the emitter, i.e. guest-to-guest transport. A photoluminescence quantum yield (PLQY) of 97% was measured for a 1:1 host-guest ratio.

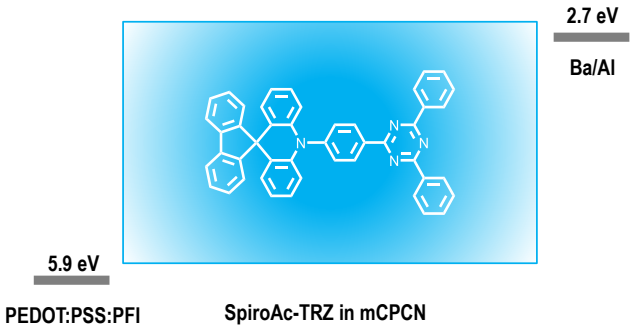

Figure 3.2. Device layout of a SpiroAc-TRZ single-layer OLED. The emissive layer comprising evaporated SpiroAc-TRZ:mCPCN (1:1) is sandwiched between a PEDOT:PSS:PFI bottom anode and a barium/aluminum top cathode. The work functions of the electrodes and the chemical structure and energy levels of SpiroAc-TRZ are indicated.

Figure 3.2 shows the device layout of our single-layer OLED, using a spin-coated layer of PEDOT:PSS:PFI as a hole contact, a co-evaporated active layer of SpiroAc-TRZ and mCPCN, and an electron contact comprising a thin layer of barium (2.5 nm) capped with aluminum (100 nm). In such a simple device architecture, balanced electron and hole transport is a prerequisite to achieve an optimal recombination zone close to the center of the emissive layer. To characterize the electron and hole transport, electron- and hole- only devices of the co-evaporated layer were fabricated. Hole-only devices were fabricated using a PEDOT:PSS:PFI/SpiroAc-TRZ:mCPCN(1:1)/C_{60}/MoO_3/Al device layout, with the C_{60}(3 nm)/MoO_3/Al top electrode as a proven ohmic hole contact.[12] The *J-V* characteristics are symmetric in voltage, indicating that injection from PEDOT:PSS:PFI is as efficient as injection from the ohmic top contact (**Figure A3.2**). Electron-only devices were fabricated using two low work function contacts in a Al/SpiroAc-TRZ:mCPCN(1:1)/Ba (5 nm)/Al layout. Intriguingly, while in previous single-layer OLEDs an ohmic electron contact required a thin (4 nm) 2,2',2''-(1,3,5-benzinetriyl)-tris(1-phenyl-1-*H*-benzimidazole) (TPBi) interlayer, it could here be omitted without compromising electron injection (**Figure A3.3a**).[11] We hypothesize that the presence of a wide-gap host pre-empts the need for an interlayer with a high LUMO, as the presence of the (high-LUMO) host molecules near the top interface could facilitate electron injection into the emitter similar to the case of a thin interlayer tunneling barrier.

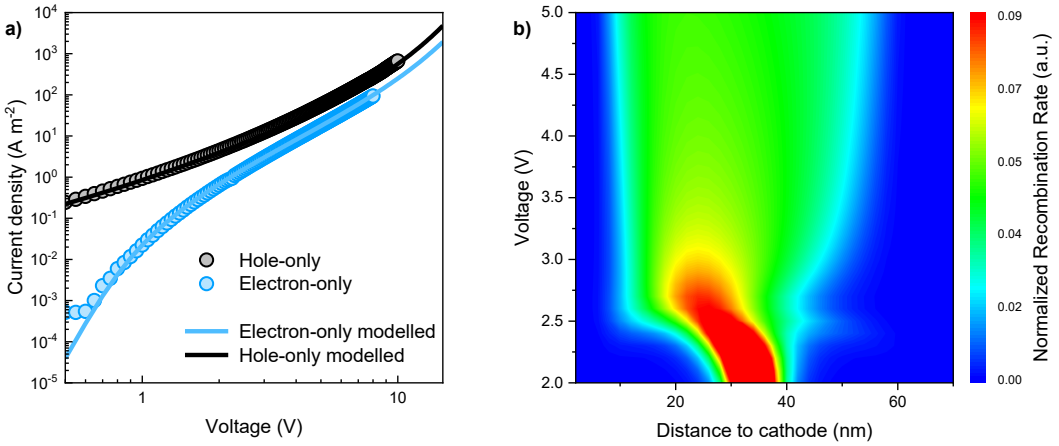

Figure 3.3. Charge transport characteristics and simulated recombination profile. a) Current density-voltage characteristics of SpiroAc-TRZ:mCPCN (1:1) electron- and hole-only devices (symbols) and simulated currents (lines), with a layer thickness of 105 nm. b) Recombination profile normalized to the integrated rate for a SpiroAc-TRZ:mCPCN double-carrier device with a layer thickness of 70 nm.

This hypothesis is confirmed by fabricating electron-only devices based on neat SpiroAc-TRZ with and without a TPBi interlayer. In the absence of a host, a large injection barrier is present when omitting the TPBi interlayer, despite the low work function of barium of 2.7 eV, which should be sufficient to align the electrode Fermi level with the LUMO of SpiroAc-TRZ (**Figure A3.3b**).[20] This confirms that the host assists in electron injection into the emitter, which would allow for further simplification of the single-layer OLED, by omitting the tunneling interlayer for electron injection.

The comparison of the electron and hole current (**Figure 3.3a**) shows balanced charge transport. To quantify the charge-transport parameters, both currents were fitted with a drift-diffusion model, in which the mobility is incorporated according to the extended Gaussian disorder model (**Table A3.1**).[21,22] The mobility for both holes and electrons amounts to 5.6×10^{-9} cm^2 V^{-1} s^{-1} in the limit of vanishing electric field and charge concentration. The hole current can be simulated without additional charge traps. The electron current shows minor electron trapping with a trap density of 2.0×10^{16} cm^{-3}. This can be observed from the stronger voltage dependence of the current at low voltage, prior to reaching the trap-filled limit at around 1 V.[23] Charge transport via the emitter is balanced and is dominated by guest-to-guest hopping in the 1:1 host:guest ratio (**Figure A3.4**). Based on the charge-transport characteristics, the recombination profile of a single-layer OLED can be simulated (**Figure 3.3b**). Owing to the balanced charge transport, the recombination profile has its maximum close to the center of the active layer, which is expected to be beneficial for the efficiency, and remains fairly constant beyond an operating voltage of 2.5 V.

Considering the balanced charge transport and the fact that ohmic hole and electron injection can be achieved with a simple polymeric anode and a metallic cathode, all prerequisites for a highly simplified blue single-layer OLED appear to be in place. Therefore, a single-layer OLED based on SpiroAc-TRZ was fabricated using the device structure as displayed in **Figure 3.2**. The current density-luminance-voltage characteristics are shown in **Figure 3.4a**, and the corresponding EQE and power efficiency are displayed in **Figure 3.4b** as a function of brightness. The OLED exhibits sky-blue light emission with an electroluminescence spectrum peaking at 490 nm (inset **Figure 3.4b**) and reaches an impressive maximum EQE of 27.7%. A luminance of 100 cd m^{-2} is already reached at 3.1 V, only slightly exceeding the magnitude of the optical energy gap of 2.88 eV. As a result of the high EQE and the low operating voltage, the device reaches a maximum power efficiency of 85 lm W^{-1}. In addition, the efficiency roll-off is relatively small, maintaining a high EQE of 23% even at a luminance of 1000 cd m^{-2}. The turn-on voltage at 1 cd m^{-2} equals 2.53 V, which is lower than the optical gap of 2.88 eV (**Figure A3.5**), which can be traced back to the recombination of diffused and thermally generated charge carriers below the built-in voltage, the concentration of which is maximized due to the ohmic contacts.[24] For this reason, single-layer OLEDs with ohmic contacts are capable of operating at very low voltages. A control device with a non-ohmic PEDOT:PSS electrode reaches an EQE of 14% (**Figure A3.6**), even after electrical conditioning. The device-performance parameters are summarized in **Table A3.2**. These device characteristics are on par with state-of-the-art multilayer OLEDs, with the difference that here the performance is achieved with an emissive layer simply sandwiched between a polymeric anode and a metal cathode, without any (high triplet energy) charge- or exciton blocking layers. The highly reduced complexity of the device both in terms of the amount of materials and the number of layers is very attractive for the fabrication, design and analysis of OLEDs.

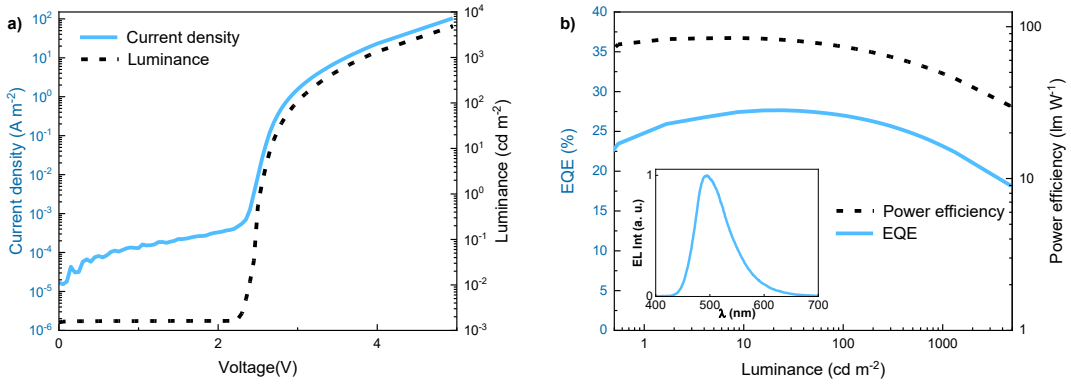

Figure 3.4. Device performance of a single-layer SpiroAc-TRZ:mCPCN (1:1) OLED. a) Current density-voltage and luminance-voltage characteristics of a single-layer SpiroAc-TRZ:mCPCN (1:1) OLED with an emissive-layer thickness of 77 nm. b) EQE and power efficiency vs. luminance, Inset: electroluminescence spectrum with a maximum at 490 nm.

Despite the obvious benefits of such a simple device layout, a question that may arise is whether the absence of blocking layers would compromise the device performance, as such additional layers have been crucial in the development of OLEDs over recent years. To assess such potential performance losses, the internal quantum efficiency by means of optical outcoupling simulations was analyzed.[8,25] The model simulates the fraction of light that is emitted to air and incorporates the measured optical constants of all layers including the co-evaporated SpiroAc-TRZ:mCPCN (1:1) film (**Figure A3.7**), as well as the horizontal dipole orientation of the emitter of 83% (**Figure A3.8a**), as was also obtained previously for this system.[18] The maximum simulated optical outcoupling efficiency for a device with an optimized 80 nm SpiroAc-TRZ:mCPCN layer equals ~27% (**Figure A3.9**), similar to what has previously been obtained for light outcoupling in single-layer OLEDs.[25] The fact that the outcoupling efficiency matches the measured EQE implies that the internal quantum efficiency approaches unity. Therefore, even without blocking layers, no charges or excitons are lost by surface recombination or quenching at the electrodes.

The addition of a 20 nm hole- and exciton-blocking layer between the emissive layer and the cathode did not improve the EQE (**Figure A3.10**), confirming that nonradiative losses near the metallic cathode are absent. Indeed, it has been demonstrated that such nonradiative losses are fully suppressed for truly ohmic contacts[26], as have been used in our blue single-layer OLED. Near ohmic contacts, the charge density of majority carriers is high (**Figure A3.11**), such that minority carriers cannot escape the device without recombining. This can also be seen from the simulated recombination profile in **Figure 3.3b**, where the recombination rate goes to zero near the electrode interfaces, implying no leaking of minority carriers into the electrodes. In **Figure A3.11**, it is demonstrated that the simulated electrical efficiency, defined as number of formed excitons per injected charge, equals unity, rationalizing the high internal quantum efficiency. Additionally, it was demonstrated that the EQE is temperature independent (**Figure A3.12**), which further excludes potential nonradiative losses, such as exciton-polaron quenching. The realization of a single-layer OLED with zero electric loss demonstrates that there is no fundamental efficiency deficit with regard to complex multi-layer structures and paves the way for future highly efficient printed OLEDs.

3.3 Conclusion

In conclusion, it was demonstrated that a highly efficient and simple sky-blue OLED can be accomplished with one layer of light-emitting material between two ohmic contacts. The OLED consists of a layer of a TADF emitter blended with a host in equal ratios, sandwiched between a PEDOT:PSS:PFI hole contact and a metal top electrode, without any additional interlayers. It was verified that these contacts provide ohmic charge injection, leading to a highly simplified single-layer OLED with 27.7% EQE and low operating voltage, with a low efficiency roll-off at high brightness.

Using optical outcoupling simulations, it was demonstrated that the device exhibits close to 100% internal quantum efficiency, establishing that additional charge- and exciton-blocking layers are not needed in a single-layer OLED with ohmic contacts. Therefore, our work demonstrates that a very simple device architecture with a greatly reduced number of materials and coating steps can rival current multilayer OLEDs. The solution-processed hole contact even lays the foundations for efficient fully solution-processed single-layer OLEDs. Not only is this highly simplified single-layer OLED structure advantageous from the perspective of device design and fabrication, but it is also of great benefit for developing understanding of the device physics, which is complicated in multilayer architectures due to the multitude of materials and heterojunctions and associated energy barriers, of which the charge-transport and barrier-height parameters are rarely known sufficiently precise for a meaningful analysis.

References

[1] C. W. Tang, S. A. Vanslyke, *Appl. Phys. Lett.* **1987**, *51*, 913.

[2] J. Kido, M. Kimura, K. Nagai, *Science* **1995**, *267*, 1332.

[3] H. Uoyama, K. Goushi, K. Shizu, H. Nomura, C. Adachi, *Nature* **2012**, *492*, 234.

[4] C. Adachi, M. A. Baldo, M. E. Thompson, S. R. Forrest, *J. Appl. Phys.* **2001**, *90*, 5048.

[5] Y. Liu, C. Li, Z. Ren, S. Yan, M. R. Bryce, *Nat. Rev. Mater.* **2018**, *3*.

[6] K. Walzer, B. Männig, M. Pfeiffer, K. Leo, *Chem. Rev.* **2007**, *107*, 1233.

[7] S. Y. Kim, J. J. Kim, *Org. Electron.* **2010**, *11*, 1010.

[8] M. Furno, R. Meerheim, S. Hofmann, B. Lüssem, K. Leo, *Phys. Rev. B - Condens. Matter Mater. Phys.* **2012**, *85*, 1.

[9] J. W. Sun, J. H. Lee, C. K. Moon, K. H. Kim, H. Shin, J. J. Kim, *Adv. Mater.* **2014**, *26*, 5684.

[10] Q. Zhang, D. Tsang, H. Kuwabara, Y. Hatae, B. Li, T. Takahashi, S. Y. Lee, T. Yasuda, C. Adachi, *Adv. Mater.* **2015**, *27*, 2096.

[11] N. B. Kotadiya, P. W. M. Blom, G. J. A. H. Wetzelaer, *Nat. Photonics* **2019**, *13*, 765.

[12] N. B. Kotadiya, H. Lu, A. Mondal, Y. Ie, D. Andrienko, P. W. M. Blom, G. J. A. H. Wetzelaer, *Nat. Mater.* **2018**, *17*, 329.

[13] T. W. Lee, Y. Chung, O. Kwon, J. J. Park, *Adv. Funct. Mater.* **2007**, *17*, 390.

[14] Z. Zhong, Y. Ma, H. Liu, F. Peng, L. Ying, S. Wang, X. Li, J. Peng, Y. Cao, *ACS Appl. Mater. Interfaces* **2020**, *12*, 20750.

[15] Y. H. Kim, C. Wolf, H. Cho, S. H. Jeong, T. W. Lee, *Adv. Mater.* **2016**, *28*, 734.

[16] D. Belaineh, J. K. Tan, R. Q. Png, P. F. Dee, Y. M. Lee, B. N. N. Thi, N. S. Ridzuan, P. K. H. Ho, *Adv. Funct. Mater.* **2015**, *25*, 5504.

[17] T. L. Wu, M. J. Huang, C. C. Lin, P. Y. Huang, T. Y. Chou, R. W. Chen-Cheng, H. W. Lin, R. S. Liu, C. H. Cheng, *Nat. Photonics* **2018**, *12*, 235.

[18] T. A. Lin, T. Chatterjee, W. L. Tsai, W. K. Lee, M. J. Wu, M. Jiao, K. C. Pan, C. L. Yi, C. L. Chung, K. T. Wong, C. C. Wu, *Adv. Mater.* **2016**, *28*, 6976.

[19] M. S. Lin, S. J. Yang, H. W. Chang, Y. H. Huang, Y. T. Tsai, C. C. Wu, S. H. Chou, E. Mondal, K. T. Wong, *J. Mater. Chem.* **2012**, *22*, 16114.

[20] K. C. Mishra, R. Garner, P. C. Schmidt, *J. Appl. Phys.* **2004**, *95*, 3069.

[21] L. J. A. Koster, E. C. P. Smits, V. D. Mihailetchi, P. W. M. Blom, *Phys. Rev. B - Condens. Matter Mater. Phys.* **2005**, *72*, 1.

[22] W. F. Pasveer, J. Cottaar, C. Tanase, R. Coehoorn, P. A. Bobbert, P. W. M. Blom, M. De Leeuw, M. A. J. Michels, *Phys. Rev. Lett.* **2005**, *94*, 1.

[23] W. Kao, K.-C.; Hwang, *Pergamon Press* **1981**, *14*.

[24] Y. Li, O. Sachnik, B. van der Zee, K. Thakur, C. Ramanan, G. J. A. H. Wetzelaer, P. W. M. Blom, *Adv. Opt. Mater.* **2021**, *9*.

[25] Y. Li, N. B. Kotadiya, B. van der Zee, P. W. M. Blom, G. J. A. H. Wetzelaer, *Adv. Opt. Mater.* **2021**, *9*, 2001812.

[26] G. J. A. H. Wetzelaer, P. W. M. Blom, *ACS Appl. Mater. Interfaces* **2022**, *14*, 7523.

[27] S. R. Forrest, D. D. C. Bradley, M. E. Thompson, *Adv. Mater.* **2003**, *15*, 1043.

4. Reduction of non-radiative losses in trap-free organic light-emitting diodes

In chapter 2 the organic semiconductor 9,9',9"-(5-(4,6-diphenyl-1,3,5-triazin-2-yl)benzene-1,2,3-triyl)tris(9*H*-carbazole) (3CzTRZ) was identified as an promising candidate for efficient single-layer blue organic light-emitting diodes (OLEDs). Next to trap-free electron and hole transport, it offers thermally activated delayed fluorescence (TADF) for triplet harvesting and a large band gap of ~ 3.0 eV. Even though offering promising properties, neat films of 3CzTRZ suffer from a low PLQY of only 40%. In time-resolved photoluminescence measurements it is revealed that the low PLQY is a result of the fast intersystem crossing rate (~10^7 s^{-1}) with the reverse intersystem crossing being almost 3 orders of magnitude lower (~10^4 s^{-1}) and comparable to the rate of non-radiative recombination of triplet excitons to the ground state. As mentioned in chapter 1.6, 75% of excitons in an OLED are generated in the triplet-state. The loss of non-radiative triplets results in a low external quantum efficiency of 4.5% employing 3CzTRZ in a single-layer OLED. It is shown, that the incorporation of 3CzTRZ in a large band gap host, increases the triplet lifetime by at least one order of magnitude, enhancing the PLQY to 70% and boosting the EQE to 15%.

The following chapter is based on:

O. Sachnik, X. Zhou, J. Nikan, B. van der Zee, Y. Li, Paul W. M. Blom, G.-J. A. H. Wetzelaer, Reduction of Non-Radiative Losses in Trap-Free Organic Light-Emitting Diodes by Dilution with A Large Bandgap Host, Adv. Opt. Mater. 2024, 12, 2302000.

Author contributions:

Oskar Sachnik performed PLQY measurements, device fabrication and electrical characterization and prepared all figures. Xin Zhou carried out time-resolved photoluminescence measurements and fitted the PL decay curves. Jawid Nikan simulated the EQE roll-off. Bas van der Zee simulated the ELQY and PLQY. Paul W.M. Blom proposed the project and Gert-Jan A. H. Wetzelaer supervised the project. Paul W. M. Blom wrote the initial manuscript, with input from Gert-Jan A. H. Wetzelaer and Oskar Sachnik.

4.1 Introduction

Upon years of continuous research, organic light-emitting diodes (OLEDs) have emerged as one of the most advanced technologies for display applications.[1] In its most simple form, an OLED requires an organic semiconductor, sandwiched between an electron-injecting cathode and hole-injecting anode. However, a major problem for such a single-layer device is the presence of extrinsic defects in the organic semiconductor, such as oxygen and water.[2–5] Such defects have a triple negative effect on OLED efficiency: first, they trap charge carriers leading to non-radiative trap-assisted recombination.[6] Second, singlet excitons formed after bimolecular recombination of injected electrons and holes diffuse towards defects where they get quenched, resulting in a low photoluminescence quantum yield (PLQY).[7] Third, due to the unbalanced transport by trapping of electrons and/or holes the recombination zone is located close to one of the injecting electrodes, leading to a low outcoupling efficiency.[8] Consequently, the common perception is that a high efficiency can only be attained with the use of a multilayer OLED structure. In these multilayer structures, the recombination zone is confined in a thin emissive layer, surrounded by transport and blocking layers.[9,10] The incorporation of electron and hole-transporting layers compensates for injection issues from the contacts and for imbalanced charge transport that most organic semiconductors suffer from.[11] Additionally, exciton blocking layers are introduced to prevent the migration and quenching of excitons.[12,13] Furthermore, the thin emissive layer can be placed in a position in the OLED that is optimal for light outcoupling.[14] As a result, most multilayer structures contain 5 or more layers, which prevents the use of solution processing due to stack integrity issues leading to enhanced fabrication costs. Furthermore, the more complex structure hinders optimization and understanding of degradation processes.

The prerequisite for an efficient OLED based on just a single layer of emitting material is the combination of ohmic contacts, trap-free balanced bipolar charge transport and efficient current to light conversion. Combination of all these properties sets a high demand on the selection of the organic semiconductor. Regarding trapping by extrinsic defects, it has recently been found that it is related to the energy levels of the organic semiconductor, the ionization energy (IE) and electron affinity (EA).[15] For IEs higher than 6.0 eV, hole trapping by water clusters limits the hole transport, whereas for EAs lower than 3.5 eV, electron transport is hindered by trapping due to oxygen-related defects.[4,16] Therefore, the energy levels of an organic semiconductor have to be situated within this energy window to enable trap-free electron and hole transport. The organic semiconductor (9,10-bis(4-(9*H*carbazol-9-yl)−2,6-dimethylphenyl)−9,10-diboraanthracene (CzDBA) with a band gap of 2.5 eV has its energy levels located exactly at the edges of this trap-free energy window, resulting in nearly trap-free and balanced electron and hole transport.[17,18] Combined with a high PLQY (~90%) and triplet harvesting by thermally activated delayed fluorescence (TADF), an efficient OLED with 19% external quantum efficiency was realized with a simplified structure.[18,19] Here, next to the single emissive CzDBA layer,

two tunnel barriers were applied to ensure Ohmic contacts, which next to efficient charge injection also prevent quenching of charges at the electrodes due to band bending.[20] However, the width of ~2.5 eV of the trap-free energy window poses a fundamental limit for realizing trap-free transport in organic semiconductors with a band gap larger than 2.5 eV, as required for blue-emitting OLEDs, where typically a band gap of ~3 eV is needed.

In chapter 2 a strategy was presented to overcome this challenge, by spatially separating the electron and hole transporting part of an organic semiconductor having its EA outside of the trap-free window. The molecular design then enables the organic semiconductor to stack in such way, that the electron transporting part, where the LUMO is located, is protected from trap-related sources by the surrounding hole transporting part, where the HOMO is located.[21] The most promising candidate found in that study is 9,9',9''-(5-(4,6-diphenyl-1,3,5-triazin-2-yl)benzene-1,2,3-triyl)tris(9*H*-carbazole) (3CzTRZ), a compound with a band gap close to 3.0 eV and a practically trap-free electron and hole transport.[21,22] As previously demonstrated, the absence of electron and hole trapping realizes perfectly balanced charge transport in 3CzTRZ (**Figure 4.1**).[21]

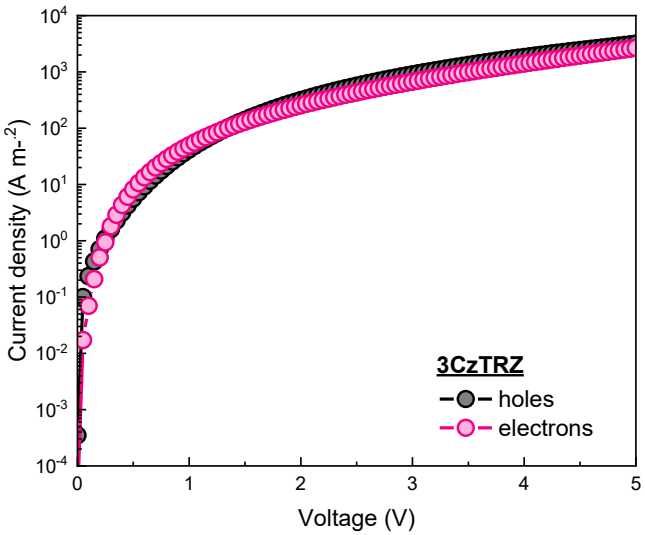

Figure 4.1. Current density (*J*)- voltage (*V*) characteristics of a hole-only and electron-only device of a neat layer 3CzTRZ with 98 nm thickness.[21] The employed device structures of the electron- and hole-only devices utilize either an ohmic electron (3CzTRZ / TPBi (4 nm)/Ba (5 nm)/Al) top contact or an ohmic hole (3CzTRZ /C_{60}/MoO_3/Al) top contact, respectively. The obtained perfectly balanced charge transport of 3CzTRZ makes it a potential candidate for a single-layer organic light-emitting diode.

Furthermore, due to its spatial separation of HOMO and LUMO orbitals, 3CzTRZ not only exhibits remarkable electrical properties, but also TADF by reverse intersystem crossing (rISC). Combination of these beneficial characteristics and the simultaneous large band gap make it a promising candidate for an efficient blue single-layer OLED.

4.2 Results and Discussion

To further investigate the suitability of 3CzTRZ for single-layer blue OLEDs, photoluminescence quantum yield (PLQY) measurements of the neat film were performed.[23] Surprisingly, in spite of the near absence of charge trapping defects at which excitons might dissociate, 3CzTRZ exhibits a relatively low PLQY of only 40% in a neat film (**Table 4.1**). For single-layer OLEDs with balanced charge transport, meaning that the recombination zone peaks in the middle of the layer, an outcoupling efficiency to air in the range of 25-26% is expected.[8] Together with a PLQY of ~40% an external quantum efficiency (EQE) of ~10-11% is therefore expected for the 3CzTRZ OLED.As a next step, an OLED was fabricated based on a single layer of 3CzTRZ sandwiched between an ohmic hole and electron contact (**Figure 4.2b**).

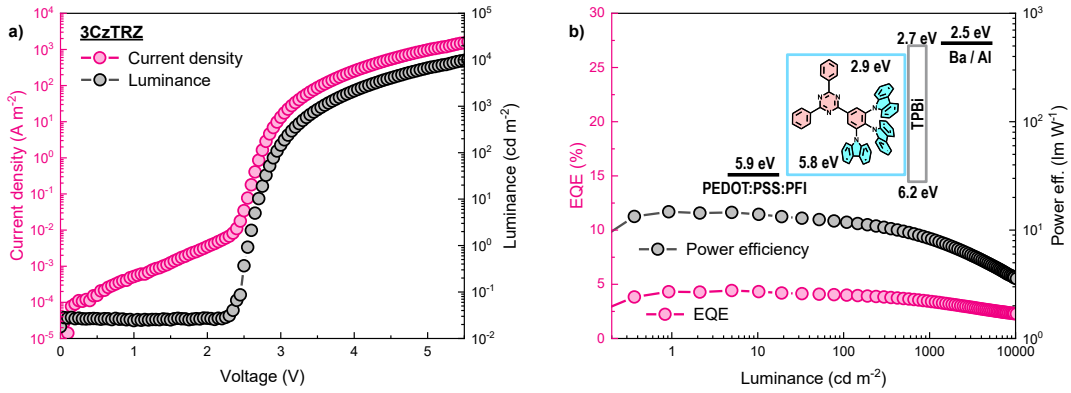

Figure 4.2. a) Current-density-voltage (*J-V)* and luminance-voltage *(L-V)* characteristics of a single-layer OLED of 3CzTRZ with 82 nm thickness b) corresponding EQE and power efficiency. The inset shows a schematic device layout of the single-layer OLED. The emissive layer is sandwiched between a PEDOT:PSS:PFI bottom anode and a barium/aluminum top cathode. To facilitate electron injection, a thin TPBi (4 nm) interlayer between emissive layer and top contact is inserted. The work functions of the electrodes and other energy levels are indicated.

As a bottom hole-injecting contact PEDOT:PSS:PFI was chosen, which was recently demonstrated to provide ohmic hole injection into organic semiconductors with IEs up to ~5.9 eV.[24] To ensure ohmic electron injection, a top contact configuration comprising a thin (4 nm) TPBi interlayer as tunnel barrier between the emissive organic semiconductor and metal cathode was used.[25].The resulting device

performance based on a simple layer of 3CzTRZ is displayed in **Figure 4.2a** and **b**. A turn-on voltage of 2.54 V at 1 cd m^{-2} is observed, which is lower than the optical bandgap (2.95 V) and is due to the recombination of diffused charge carriers below the built-in voltage.[26] The device reaches a luminance of 100 cd m^{-2} at 3.10 V and 1000 cd m^{-2} at 4.65 V.

The maximum EQE of 4.5% is considerably lower than expected from considerations based on the PLQY and outcoupling efficiency, resulting in a low power efficiency of 24 lm W^{-1}. Summarizing, in spite of the absence of charge trapping defects both PLQY and EQE of the 3CzTRZ single-layer OLEDs are far below expectations. To elucidate the origin of the low PLQY and EQE time-resolved photoluminescence (TRPL) measurements on 3CzTRZ were performed. The PL decay curve is shown in **Figure 4.3a** (red symbols). The measurements are simulated using rate equations for the singlet and triplet exciton density, given by

$$\frac{d[S]}{dt} = [S_0] - \frac{[S]}{\tau_s} - k_{ISC}[S] + k_{rISC}[T] + 0.25k_{TTA}[T][T] \quad (1)$$

$$\frac{d[T]}{dt} = -\frac{[T]}{\tau_T} + k_{ISC}[S] - k_{rISC}[T] - 1.25k_{TTA}[T][T]\,, \quad (2)$$

with $[S_0]$ the initial singlet density, τ_s and τ_t the singlet and triplet lifetime, k_{TTA} the triplet-triplet annihilation rate constant, k_{rISC} the reversed intersystem crossing rate, and $[S]$ and $[T]$ the singlet and triplet concentration, respectively.[27] Typically, the prompt fluorescence ($\boldsymbol{\tau}_{PF}$) is attributed to the singlet lifetime τ_s and represents the decay to the ground state S_0 of excitons that initially populate S_1. The delayed fluorescence ($\boldsymbol{\tau}_{DF}$) arises from fluorescence that occurs as a result of the repopulation of S_1 by T_1 via rISC. The simulation is shown in **Figure 4.3a** as a solid line and the fit parameters are given in **Table 4.1**. With the addition of a small contribution of triplet-triplet annihilation, both the decay as well as the PLQY, determined by the area under the curve, were reproduced.

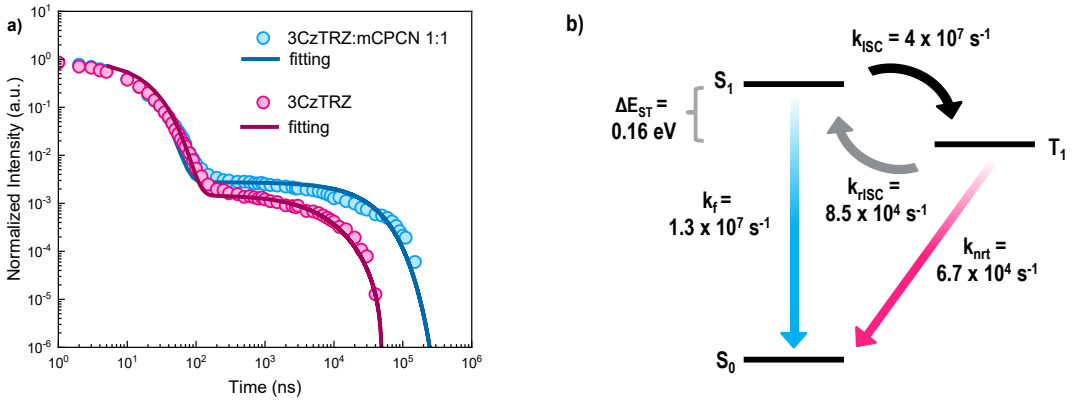

Figure 4.3. a) Transient photoluminescence decay measurement of neat 3CzTRZ (red) and 3CzTRZ:mCPCN (1:1) blend (blue) in film. Dots represent the experimental data and lines represent the fit obtained by a numerical model.[27] b) Characteristic time constants of the photophysical processes of the neat 3CzTRZ film.

To put the photophysical processes in perspective, in **Figure 4.3b** the characteristic time constants of each process in a schematic energy diagram are plotted. From fitting the PL decay, it is observed that the prompt fluorescence lifetime (τ_{PF}) is mainly governed by the fast ISC process, with the lifetime limited by intersystem crossing to the triplet state, rather than decay of the singlet state. On the other hand, the reverse intersystem crossing process is very slow and nearly equal to the triplet lifetime, implying a high chance of nonradiative decay of the triplet state. The delayed fluorescence lifetime (τ_{DF}) is entirely limited by the triplet lifetime τ_T, which can therefore be reliably obtained from fitting the PL decay. The relatively high intersystem crossing rate combined with the low reverse intersystem crossing rate, implies in practice that on the event of one triplet *to* singlet up-conversion, almost 10^3 singlet excitons experience the down-conversion to the non-emissive triplet-state.

For 3CzTRZ a singlet-triplet gap (ΔE_{ST}) of 0.16 eV was reported, which is relatively large and is most likely the origin of the low k_{rISC} rate.[22] The fact that $1/k_{ISC}<\tau_s$ has the consequence that even after a triplet has been upconverted from T_1 to S_1 it has a bigger chance to fall back to T_1 instead of radiatively recombining to S_0. Combined with the slow rISC rate the triplet state T_1 stays therefore heavily populated over a long time period. This, combined with the fact that the non-radiative triplet decay τ_T is almost equally fast as the rISC process then explains the low PLQY of 3CzTRZ.

Table 4.1: Summarized PL decay results obtained by numerical fitting

	k_{ISC} (s^{-1})	k_{rISC} (s^{-1})	τ_t (s)	τ_s (s)	k_{TTA} (m^3 s^{-1})	$PLQY_{exp}$	$PLQY_{sim}$
100%	4×10^7	8.5×10^4	1.5×10^{-5}	8×10^{-8}	6×10^{-19}	40%	35%
50%	4×10^7	1.5×10^5	$\geq 1.0 \times 10^{-4}$	1.5×10^{-7}	6×10^{-20}	69%	60%

The large population of the triplet state and resulting non-radiative losses via recombination of triplets to the ground state also has consequences for the analysis of the OLED efficiency. Typically, to rationalize the OLED efficiency, the product of the electrical efficiency, spin statistics (100% for TADF), outcoupling efficiency and PLQY is calculated. However, in the case that non-radiative losses of triplet excitons play an important role, as is the case for 3CzTRZ, this analysis is not correct. In a PLQY experiment, 100% singlets are generated as a starting point, of which a certain fraction is then transformed into triplets via ISC. In contrast, in an OLED, 75% of the excitons are directly generated as triplets, meaning that the overall triplet density and therefore non-radiative losses of triplets is different for both experiment, as also recently noted by Ruhstaller *et al*.[28] In other words, the PLQY is not necessarily equal to the electroluminescence quantum yield (ELQY).

In **Figure 4.4** the calculated PLQY and ELQY for 3CzTRZ as function of the rate of non-radiative triplet recombination k_{nrt} are plotted. The PLQY and ELQY are here determined by starting with initially 100% singlet excitons and a 1:3 singlet-to-triplet ratio, respectively, using the method of Ruhstaller *et al*.[28] For low rates (long triplet lifetimes), the triplets are mainly depleted via rISC, and non-radiative recombination of triplets does not play a role, such that PLQY equals ELQY. With increasing rate, a difference between PLQY and ELQY starts to evolve. When assuming $k_{nrt}=1/\tau_T$, the experimentally obtained triplet lifetime yields a k_{nrt} of 6.7×10^4 s^{-1}, corresponding to an ELQY of only 20%, and a PLQY of 34%. We note that k_{nrt} is likely lower in this system, since triplet-triplet annihilation will reduce k_{nrt} by taking away triplets. Additionally, the PLQY may also be influenced by additional nonradiative singlet decay, which was omitted in the calculations in **Figure 4.4** for simplicity. Most importantly, the analysis in **Figure 4.4** reveals that when the PLQY of a TADF emitter is limited by the non-radiative decay of triplet excitons, it cannot be used as a simple factor to calculate the external quantum efficiency: based on the PLQY, an EQE of around 10% would be expected for the 3CzTRZ OLED, when considering an optical-outcoupling efficiency of 25%, whereas the measured value is only 4.5%, which matches the EQE as expected from the low ELQY of 20%

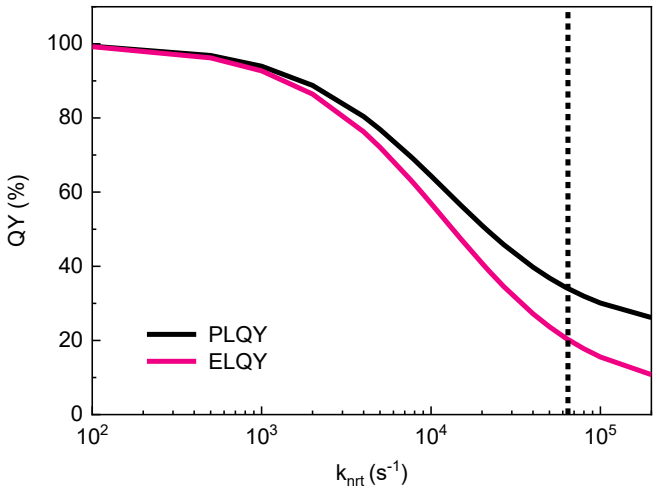

Figure 4.4. ELQY and PLQY for the 3CzTRZ emitter plotted versus k_{nrt}. The solid vertical dotted line corresponds to the value of k_{nrt} from fitting the TRPL.

A further enhancement of the ELQY and PLQY of 3CzTRZ would thus require an elongation of the triplet lifetime τ_T. A common strategy to prevent loss processes, such as concentration quenching or interactions between triplet and/or singlet excitons is the adjustment of the molecular structure in such way, that an increase in the intermolecular distance is achieved e.g. by incorporation of bulkier side groups.[29] Although such strategies typically offer improvements in reduction of the concentration quenching and increase of the PLQY, a major downside is that a simple change in the molecular structure can have tremendous influence on the intrinsic charge transport. In our study, the incorporation of *tert*-butyl groups on the carbazole donor-part resulted in a large imbalance of the charge transport, with the hole-transport being almost 2 orders of magnitude higher than the electron-transport (**Figure A4.1**). Even though this adjustment offered improvements in the PLQY (up to 79%), the imbalanced charge transport will lead inevitably to an even worse OLED performance as most of the recombination then happens close to the cathode, resulting in a low outcoupling efficiency.

Another successful strategy to increase the intermolecular separation is the incorporation of a host-matrix which enables the dilution of the emitter.[30–32] The host typically has a larger bandgap than the guest, and for sufficiently high concentration of the guest the transport of holes and electrons is carried exclusively by the guest. In this way, the balanced charge transport of 3CzTRZ, although diluted, can be preserved. mCPCN (9-(3-(9*H*-carbazol-9-yl)phenyl)-9*H*-carbazole-3-carbonitrile) was chosen as a host-matrix because of its large band gap of 3.6 eV and its previous successful employment in a single-layer OLED structure.[24] For 3CzTRZ a simple 1:1 dilution showed already an improvement of the PLQY close to 70% under nitrogen atmosphere, which is a strong indication for the reduction of non-

radiative loss-processes in the solid film. A similar PLQY enhancement was previously observed by *Lee* et al. by doping 3CzTRZ in DPEPO (bis[2-(diphenylphosphino)phenyl]ether oxide), which yielded a quantum yield of close to 100% in a 3:7 (3CzTRZ:DPEPO) dilution.[22] The TRPL of the 1:1 diluted film was also analyzed to quantitatively understand the increase of the PLQY. Measurements and the simulations are shown in **Figure 4.3a** (blue symbols), the resulting fit parameters are given in **Table 1**.

An identical decay of both films up to 100 ns was observed, which indicates that the prompt fluorescence is not affected by the dilution. In turn, this means that the singlet lifetime τ_S and intersystem crossing rate k_{ISC} that govern τ_{PF} are identical for the pristine and diluted film. Furthermore, the cross-over point from prompt- to delayed fluorescence is also hardly affected, meaning that k_{rISC} is also not strongly affected by dilution. At longer times, however, a strong increase of the delayed fluorescence in the doped film was seen. As mentioned above, the delayed fluorescence is heavily influenced by the availability of excited triplet states, which can undergo up-conversion to emissive singlets. From the modelling an at least one order of magnitude higher triplet lifetime in the doped film was obtained, which is a direct result of the dilution of excited triplets. It is observed that the delayed fluorescence lifetime is no longer limited by the triplet-exciton lifetime. The longer triplet lifetime then allows more triplets to be upconverted to the S_1 state, resulting in a higher PLQY. Also, for the diluted film, the simulated PLQY agrees well with the experimentally obtained value. For the obtained τ_T of 10^{-4} s, according to **Figure 4.4**, an ELQY of ~57% would be expected, meaning that as compared to the pristine 3CzTRZ OLED a threefold increase of the EQE is expected.

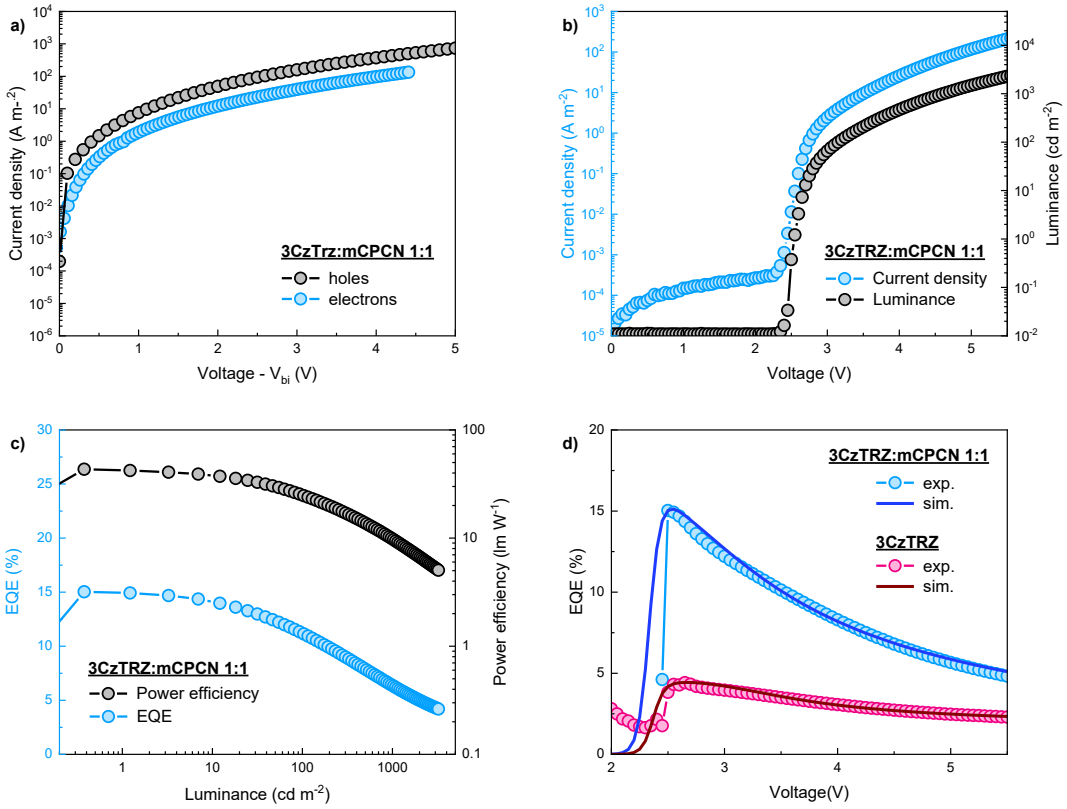

Figure 4.5. a) *J-V* characteristics of hole- and electron-only of 3CzTRZ:mCPCN (1:1) with 72 nm thickness. The voltage of the electron-only device was corrected for a built-in voltage V_{bi} of 0.63 eV.[33] b) *J-V-L* characteristics of a single-layer 3CzTRZ:mCPCN (1:1) OLED with a PEDOT:PSS:PFI/ 3CzTRZ:mCPCN (72 nm)/TPBi (4 nm)/Ba (3 nm)/Al device layout. c) corresponding EQE and power efficiency. d) EQE vs voltage of both OLEDs of pristine 3CzTRZ and 3CzTRZ:mCPCN (1:1). The experimental data is plotted as symbols, whereas the lines represent simulations with a drift-diffusion solver. The simulated singlet-generation efficiency is multiplied by a factor of 0.16 to obtain the EQE.

While maintaining trap-free charge transport and now with improved photophysical properties, a single-layer OLED of 3CzTRZ doped in the mCPCN matrix was fabricated. The resulting *J-V-L* characteristics in **Figure 4.5b** reveal a similar turn-on voltage of 2.54 V compared to the neat film device, as would be expected for direct charge injection into the emitter. The doped device reaches a luminance of 100 cd m^{-2} at 3.2 V and 1000 cd m^{-2} at 4.6 V. Interestingly, similar voltages need to be applied to achieve the same brightness as in the neat film device. Normally, upon dilution an increase in the operating voltage would be expected. A closer look reveals that indeed only half of the current is passed through the diluted sample at the same voltage, which is a direct result of a lower charge mobility due to separation of charge transport sites. Nevertheless, it is observed that the same amount of light is being generated at a

given voltage, which results from an enhanced ELQY. Even though less charges are present in the diluted sample, the excited triplet states have more time to undergo the RISC process and decay by light emission as already demonstrated by our TRPL results. The benefits of dilution are also represented in the corresponding EQE and power efficiency (**Figure 4.5c**), which experience the expected threefold enhancement to 15% and 43 lm W^{-1}, respectively (**Figure 4.5d**). These results confirm that embedding a balanced emitter in a host-matrix of larger band gap constitutes an effective option to enhance the TADF efficiency and ultimately the device performance.

To analyze the EQE vs voltage characteristics in more detail, the OLEDs were simulated with a recently developed drift-diffusion model for TADF OLEDs.[34] First, the *J-V* characteristics are simulated based on the electron and hole mobility obtained from the charge-transport measurements. The drift-diffusion simulations then solve the recombination rate, and therefore exciton density, as a function of position in the device. Subsequently, the singlet-generation efficiency as a function of voltage is obtained by implementing the experimental photophysical parameters, including the exciton lifetimes, the rISC rates, and triplet-triplet annihilation. Multiplying the singlet-generation efficiency with a factor that includes the optical outcoupling and the radiative decay of singlet excitons then gives the EQE. For the neat 3CzTRZ-based OLED, the maximum singlet-generation efficiency amounts to only 27% (**Figure A4.3d**), being the result of the nonradiative decay of triplet excitons due to the short triplet lifetime, as determined from the PL experiment. This low internal efficiency therefore explains the low EQE of only 4.5%. In addition, the efficiency roll-off can be entirely reproduced without any fit parameters and is governed by the experimental triplet-triplet annihilation rate.

For the 3CzTRZ:mCPCN OLED, the maximum singlet-generation efficiency is drastically increased up to 70% to 93% (**Figure A4.4d**), which is entirely due to the increased triplet lifetime, resulting an increased amount of triplet excitons converted to the singlet state via rISC. Only a range in electrical efficiency can be given, since only a minimum value for the triplet lifetime can be estimated from the PL decay. Nevertheless, the greatly enhanced singlet-generation efficiency due to the increased triplet lifetime is in accordance with the threefold enhancement in EQE of the OLED upon dilution in a host matrix. The efficiency-roll of is also reproduced, but requires additional triplet-polaron quenching to match the shape of the EQE-*V* curve. This observation is tentatively explained by the reduction of triplet-triplet annihilation in the diluted film, in turn increasing the relative importance of other annihilation effects, such as triplet-polaron quenching. It is noted, that further dilution of the emitter (1:2) leads to a further improvement of the PLQY (99%), but at the same time to a larger imbalance in the electron and hole transport (**Figure A4.2a**). The resulting reduction of the outcoupling efficiency nearly compensates the increase of the PLQY, such that only a limited further improvement in the device performance is achieved (**Figure A4.2c**, 17% EQE and 46 lm W^{-1}).

4.3 Conclusion

In conclusion, it was demonstrated that the electrical quantum efficiency of OLEDs based on the emitter 3CzTRZ is improved by reduction of the nonradiative triplet decay rate upon dilution of the emitter in a large gap host. The combination of trap-free transport and TADF make 3CzTRZ a promising candidate for single-layer OLEDs. However, even though having promising electrical properties, 3CzTRZ on its own suffers from a low PLQY of 40% in the solid film and, unexpectedly, a comparatively even lower EQE of only 4.5% in a single-layer OLED. TRPL measurements were performed, which revealed that 3CzTRZ mainly suffers from an imbalance of k_{ISC} and k_{RISC}, with k_{ISC} being almost 3 orders higher due to the large ΔE_{ST} of 0.16 eV. Since k_{RISC} is close to the rate of non-radiative recombination of triplets to the ground state, the majority of generated singlet excitons are converted to the triplet state and decay from there non-radiatively. In an OLED, this effect is even further amplified since 75% of the excitons are directly generated in the triplet state. By doping 3CzTRZ in a large band gap matrix, the triplet lifetime is extended by at least one order of magnitude and the PLQY is improved to 70%. Incorporated in a single-layer OLED, the 3CzTRZ:mCPCN guest-host system showed three-fold enhancement of the EQE to 15%. The doped film of 3CzTRZ exhibits similar operating voltages to the neat film, even though less current is passed through the layer, giving rise to a high power efficiency of 43 lm W^{-1}. Through a combination of transient PL measurements and drift-diffusion device simulations, it is shown that the enhanced OLED performance upon dilution of 3CzTRZ in a mCPCN matrix is due to an elongated triplet-exciton lifetime.

References

[1] C. W. Tang, S. A. Vanslyke, *Appl. Phys. Lett.* **1987**, *51*, 913.

[2] J. M. Zhuo, L. H. Zhao, R. Q. Png, L. Y. Wong, P. J. Chia, J. C. Tang, S. Sivaramakrishnan, M. Zhou, E. C. W. Ou, S. J. Chua, W. S. Sim, L. L. Chua, P. K. H. Ho, *Adv. Mater.* **2009**, *21*, 4747.

[3] A. Seemann, T. Sauermann, C. Lungenschmied, O. Armbruster, S. Bauer, H. J. Egelhaaf, J. Hauch, *Sol. Energy* **2011**, *85*, 1238.

[4] H. T. Nicolai, M. Kuik, G. A. H. Wetzelaer, B. De Boer, C. Campbell, C. Risko, J. L. Brédas, P. W. M. Blom, *Nat. Mater.* **2012**, *11*, 882.

[5] P. K. Nayak, R. Rosenberg, L. Barnea-Nehoshtan, D. Cahen, *Org. Electron.* **2013**, *14*, 966.

[6] G. J. A. H. Wetzelaer, M. Scheepers, A. M. Sempere, C. Momblona, J. Ávila, H. J. Bolink, *Adv. Mater.* **2015**, *27*, 1837.

[7] I. Rörich, A. K. Schönbein, D. K. Mangalore, A. Halda Ribeiro, C. Kasparek, C. Bauer, N. I. Cr ăciun, P. W. M. Blom, C. Ramanan, *J. Mater. Chem. C* **2018**, *6*, 10569.

[8] Y. Li, N. B. Kotadiya, B. van der Zee, P. W. M. Blom, G. J. A. H. Wetzelaer, *Adv. Opt. Mater.* **2021**, *9*, 2001812.

[9] B. Ruhstaller, T. Beierlein, H. Riel, S. Karg, J. C. Scott, W. Riess, *IEEE J. Sel. Top. Quantum*

Electron. **2003**, *9*, 723.

[10] B. Perucco, N. A. Reinke, D. Rezzonico, E. Knapp, S. Harkema, B. Ruhstaller, *Org. Electron.* **2012**, *13*, 1827.

[11] N. Chopra, J. Lee, Y. Zheng, S. H. Eom, J. Xue, F. So, *ACS Appl. Mater. Interfaces* **2009**, *1*, 1169.

[12] V. I. Adamovich, S. R. Cordero, P. I. Djurovich, A. Tamayo, M. E. Thompson, B. W. D'Andrade, S. R. Forrest, *Org. Electron.* **2003**, *4*, 77.

[13] C. H. Shih, P. Rajamalli, C. A. Wu, W. T. Hsieh, C. H. Cheng, *ACS Appl. Mater. Interfaces* **2015**, *7*, 10466.

[14] J. Kido, M. Kimura, K. Nagai, *Science (80-.).* **1995**, *267*, 1332.

[15] N. B. Kotadiya, A. Mondal, P. W. M. Blom, D. Andrienko, G. J. A. H. Wetzelaer, *Nat. Mater.* **2019**, *18*, 1182.

[16] N. B. Kotadiya, A. Mondal, P. W. M. Blom, D. Andrienko, G. J. A. H. Wetzelaer, *Nat. Mater.* **2019**, *18*, 1182.

[17] T. L. Wu, M. J. Huang, C. C. Lin, P. Y. Huang, T. Y. Chou, R. W. Chen-Cheng, H. W. Lin, R. S. Liu, C. H. Cheng, *Nat. Photonics* **2018**, *12*, 235.

[18] N. B. Kotadiya, P. W. M. Blom, G. J. A. H. Wetzelaer, *Nat. Photonics* **2019**, *13*, 765.

[19] H. Uoyama, K. Goushi, K. Shizu, H. Nomura, C. Adachi, *Nature* **2012**, *492*, 234.

[20] N. B. Kotadiya, H. Lu, A. Mondal, Y. Ie, D. Andrienko, P. W. M. Blom, G. J. A. H. Wetzelaer, *Nat. Mater.* **2018**, *17*, 329.

[21] O. Sachnik, X. Tan, D. Dou, C. Haese, N. Kinaret, K.-H. Lin, D. Andrienko, M. Baumgarten, R. Graf, G.-J. A. H. Wetzelaer, J. J. Michels, P. W. M. Blom, *Nat. Mater.* **2023**.

[22] D. R. Lee, M. Kim, S. K. Jeon, S. H. Hwang, C. W. Lee, J. Y. Lee, *Adv. Mater.* **2015**, *27*, 5861.

[23] L. Porrès, A. Holland, L. O. Pålsson, A. P. Monkman, C. Kemp, A. Beeby, *J. Fluoresc.* **2006**, *16*, 267.

[24] O. Sachnik, Y. Li, X. Tan, J. J. Michels, P. W. M. Blom, G. A. H. Wetzelaer, *Adv. Mater.* **2023**, 2300574.

[25] D. Trieb, P. W. M. Blom, G. J. A. H. Wetzelaer, *Adv. Mater. Interfaces* **2023**, *2202424*, 1.

[26] Y. Li, O. Sachnik, B. van der Zee, K. Thakur, C. Ramanan, G. J. A. H. Wetzelaer, P. W. M. Blom, *Adv. Opt. Mater.* **2021**, *9*.

[27] K. Thakur, B. van der Zee, G. J. A. H. Wetzelaer, C. Ramanan, P. W. M. Blom, *Adv. Opt. Mater.* **2022**, *10*.

[28] S. Sem, S. Jenatsch, K. Stavrou, A. Danos, A. P. Monkman, B. Ruhstaller, *J. Mater. Chem. C* **2022**, *10*, 4878.

[29] Y. Mei, D. Liu, J. Li, J. Wang, *J. Mater. Chem. C* **2022**, *10*, 16524.

[30] Y. J. Cho, K. S. Yook, J. Y. Lee, *Adv. Mater.* **2014**, *26*, 4050.

[31] W. S. Jeon, T. J. Park, S. Y. Kim, R. Pode, J. Jang, J. H. Kwon, *Org. Electron.* **2009**, *10*, 240.

[32] C. H. Chang, M. C. Kuo, W. C. Lin, Y. T. Chen, K. T. Wong, S. H. Chou, E. Mondal, R. C. Kwong, S. Xia, T. Nakagawa, C. Adachi, *J. Mater. Chem.* **2012**, *22*, 3832.

[33] G. A. H. Wetzelaer, *Phys. Rev. Appl.* **2020**, *13*, 1.

[34] B. van der Zee, Y. Li, G. J. A. H. Wetzelaer, P. W. M. Blom, *Adv. Electron. Mater.* **2022**, *8*, 2101261.

5. Trap-free host for single-layer organic light-emitting diodes

In chapter 2 it was revealed that the organic semiconductor 9,9',9"-(5-(4,6-diphenyl-1,3,5-triazin-2-yl)benzene-1,2,3-triyl)tris(9*H*-carbazole) (3CzTRZ) offers trap-free electron and hole transport combined with a large band gap of ~ 3.0 eV. In spite of offering promising capabilities, in-depth studies in chapter 4 showed, that the pristine material is limited in terms of PLQY and ELQY due to a slow reverse intersystem crossing rate. Nevertheless, due to its superior charge-transport, 3CzTRZ can be employed as a large band gap host for other organic emitters. Most organic semiconductors need to be incorporated in so-called multilayer OLED stacks (see 1.8.1), to compensate for the unbalanced charge transport that most materials suffer from. In this chapter, the green emitting bis(4-(9,9-dimethylacridin-10(9*H*)-yl)phenyl)methanone (DMAC-BP) with a strongly trap-limited electron current is used as guest in combination with 3CzTRZ as a large band gap host. 3CzTRZ assists in the electron transport, improving it by several orders of magnitude. This way, balanced charge transport is accomplished within one semiconducting layer. The resulting EQE of 19.6% in a single-layer architecture is comparable to reported results in multilayer devices (18.9 – 21%). Next to comparable external efficiencies, the OLED offers an almost 40% higher power efficiency and longer lifetimes, than other reported devices.

The following chapter is based on:

O. Sachnik, Y. Ie, N. Ando, X. Tan, P. W. M. Blom, G.-J. A. H. Wetzelaer, Single-Layer Organic Light-Emitting Diode with Trap-Free Host Beats Power Efficiency and Lifetime of Multilayer Devices, Adv. Mater. 2024, 36, 2311892.

Author contributions:

Oskar Sachnik developed the idea, performed device fabrication and electrical characterization, collected the data and prepared all figures. Yutaka Ie and Naoki Ando carried out LEIPS measurements. Xiao Tan performed electrical characterization of DMAC-BP. P.W.M.B. proposed the project and Gert-Jan A. H. Wetzelaer supervised the project. Paul W. M. Blom wrote the initial manuscript, with input from Gert-Jan A. H. Wetzelaer and Oskar Sachnik.

5.1 Introduction

In the last decade, organic light-emitting diodes (OLEDs) have become the dominating technology for displays of mobile applications, such as phones and tablets. The achieved high external quantum efficiencies (EQEs) in the 20-30% range are the result of a number of developments, including the harvesting of dark triplet excitons via phosphorescence and efficient charge injection by using doped injection layers.[1–3] Furthermore, to compensate for unbalanced charge transport, charge-blocking layers are employed, which confine electrons and holes in the emissive layer that typically employs a host-guest structure.[4,5] To avoid diffusion of excitons to neighboring layers. exciton-blocking layers with a high triplet energy are employed as well.[6,7] Consequently, a typical multilayer OLED consists of 5-6 layers with a total of 6-8 different organic molecules. In recent research, in order to avoid the use of rare and expensive heavy-metal containing phosphorescent emitters, all-organic emitters exhibiting thermally activated delayed fluorescence (TADF) have been developed as an alternative method to harvest triplet excitons.[8] By a reduction of the overlap between the highest occupied (HOMO) and lowest unoccupied molecular orbitals (LUMO) the energetic splitting between the singlet and triplet energy is strongly reduced, enabling a conversion from triplets to singlets by thermal energy.

So far, OLEDs based on these TADF emitters employ the same multilayer device structure as used for phosphorescent emitters.[9–11] As a result, there is a general consensus that such a multilayer structure is a prerequisite for achieving highly efficient OLEDs. Achieving simultaneous efficient charge injection, high electroluminescence quantum yield, absence of exciton quenching at the electrodes and balanced transport in just one active layer is deemed unrealistic. An OLED with a single-layer architecture, however, could potentially have a number of advantages over multilayer OLEDs. First, the number of organic compounds would be strongly reduced from 6-8 to only 1 or 2. Next to the absence of intermittent evaporation steps and cross contamination prevention, this would also allow printing of the active layer without stack integrity issues, which combined will give a cost advantage. Furthermore, the spreading of the emission zone over the complete device structure as compared to the recombination confinement in a thin layer could be beneficial for the device stability due to the reduced local exciton and charge carrier concentrations.[12–16] This would reduce degradation effects originating from exciton-exciton and/or exciton-polaron annihilation.[17–23] The absence of charge blocking layers will also enable charge carriers to travel through the OLED without the obstruction of charge blocking layers, which is beneficial for the operating voltage.[24–26] In case of an equal EQE this would result in a higher power efficiency, which is relevant for portable applications.

The big ‘if’, however, is the question whether EQEs comparable to state-of-the-art multilayer OLEDs can be reached by a device employing only one organic active layer. In recent years, the prerequisites to obtain high efficiencies in a single-layer OLED have been investigated. Here, fluorescent polymer-

based LEDs (PLEDs) have been used as a workhorse. For a PLED based on the conjugated polymer super-yellow poly(phenylene-vinylene) (SY-PPV) it was found that the EQE of 4% is the result of a combination of direct electron-hole recombination (2.5%) and triplet-triplet annihilation (TTA) (1.5%). Since TTA is a loss process in TADF-based OLEDs the addition of a triplet harvesting functionality would only increase the EQE to a maximum of 10%.[27] Further enhancement of the efficiency requires the elimination of electron trapping, which has a triple negative effect on the EQE. First, the non-radiative recombination of trapped electrons with free holes is a loss process, lowering the electrical efficiency in the range of 70-80%.[28] Furthermore, also the photoluminescence quantum yield is lowered to 65% since singlet excitons dissociate at the electron traps.[29] Finally, the resulting confinement of the recombination zone close to the cathode lowers the optical outcoupling efficiency.[30] Elimination of the electron trapping would enhance the maximum attainable efficiency then from 10% to the 27-28% range for a single-layer device, which would be on par with the multilayer OLEDs. An essential step is therefore the elimination of trapping effects.

In a recent study, it was demonstrated that for organic semiconductors a trap-free energy window exists with a width of 2.5 eV.[31] Semiconductors with an electron affinity lower than 3.5 eV are susceptible to electron trapping, whereas an ionization energy larger than 6 eV gives rise to hole trapping. For trap-free bipolar charge transport, both energy levels have to be inside this energy window. This, however, puts a fundamental challenge on the realization of trap-free organic semiconductors with a bandgap larger than 2.5 eV, as required for blue OLEDs. Another important condition for realizing efficient single-layer OLEDs is the realization of Ohmic contacts. Not only is efficient charge injection beneficial for the efficiency and operating voltage of the OLED, but the resulting band bending due to the accumulated charges near the Ohmic contact prevents the minority carrier to leave the device without recombining[32]. In this way, Ohmic contacts additionally prevent recombination close to the metallic electrode, avoiding outcoupling losses due to energy transfer to surface plasmon polariton modes.[33,34] It was found that Ohmic contacts on nearly any organic semiconductor can be realized by the combination of a tunnel barrier with a metal-oxide electrode.[35] Here, the tunnel barrier electrostatically decouples the electrode from the semiconductor. Using this injection strategy combined with the energetic demands for trap-free bipolar transport, an OLED based on the yellow TADF emitter 5,10-bis(4-(9*H*-carbazol-9-yl)phenyl)-5,10-dihydroboranthrene (CzDBA) was fabricated.[36] The OLED comprised a simplified structure consisting of two tunnel barriers and an active layer of CzDBA, which has the relevant energy levels exactly at the edges of the trap-free window. Due to the resulting nearly trap-free electron and hole transport combined with Ohmic contacts an EQE of 19% was achieved.
The fact that the realization of bipolar trap-free transport puts stringent demands on the energy levels of TADF emitters excludes many well-known materials for the realization of efficient single-layer OLEDs. One such example is the green emitter bis(4-(9,9-dimethylacridin-10(9*H*)-

yl)phenyl)methanone (DMAC-BP).[37] Employed in doped and non-doped multilayer OLED stacks, EQEs in the range 19-21% have been reported, together with (maximum) power efficiencies of 52.9-59 lm W^{-1}.[37–39]

Here, a new concept of using a trap-free host material in a single-layer DMAC-BP-based OLED is demonstrated. Due to the unrivalled electron transport of the trap-free host, balanced charge transport and high mobilities are achieved for both electrons and holes. Direct charge injection into the emissive layer with the single-layer architecture, together with efficient bipolar charge transport results in very low operating voltages, giving rise to record-high power efficiencies for DMAC-BP OLEDs, clearly surpassing the best multilayer OLEDs based on this emitter. The spreading of the emission zone further results in greatly enhanced operational stability.

5.2 Results and Discussion

As good and balanced charge transport is a prerequisite for single-layer OLEDs, first the charge transport in pristine DMAC-BP was investigated. In **Figure 5.1a**, the electron and hole current density vs voltage (*J-V*) in a pristine DMAC-BP film is shown, obtained using electron- and hole only devices. Details of the devices and their processing are given in 7. *Experimental Methods*. The charge transport is highly unbalanced, which is expected given the position of the HOMO and LUMO levels of -5.6 eV and -2.7 eV, respectively. Here, the HOMO level is within the trap-free window, whereas the LUMO level is far outside, resulting in severe electron trapping. For the OLED of pristine DMAC-BP it was made use of a spin-coated PEDOT:PSS anode, of which the work function is enhanced by blending it with perfluorinated ionomers (PFI).[40] Such a solution-processed PEDOT:PSS:PFI anode was recently shown to form Ohmic contacts on CzDBA with an IE as high as 5.9 eV, without the need for a tunnel barrier.[41] For the electron injection a Ba/Al electrode was used in combination with a thin TPBi (4 nm) tunnel barrier. Although a thick TPBi layer has the potential to function as a hole-blocking and exciton-blocking layer, a 4 nm layer is not sufficient to prevent energy transfer of excitons to the metallic top electrode.[42] Furthermore, it has been demonstrated that tunneling layers in this thickness range are transparent for holes.[35] Therefore, the TPBi interlayer only facilitates electron injection, while not exhibiting a blocking function like in multilayer OLEDs. As such the OLED can be classified as a single-layer OLED, in which the use of thin injection layers is common practice. In **Figure 5.1b** and **1c**, the *J-V* and luminance-voltage (*L-V*) characteristics are shown for a pristine DMAC-BP OLED. As expected, due to the strong electron trapping and resulting confinement of the emission zone close to the cathode the maximum EQE and power efficiency of the OLED amount to only 8% and 32 lm W^{-1}, respectively.

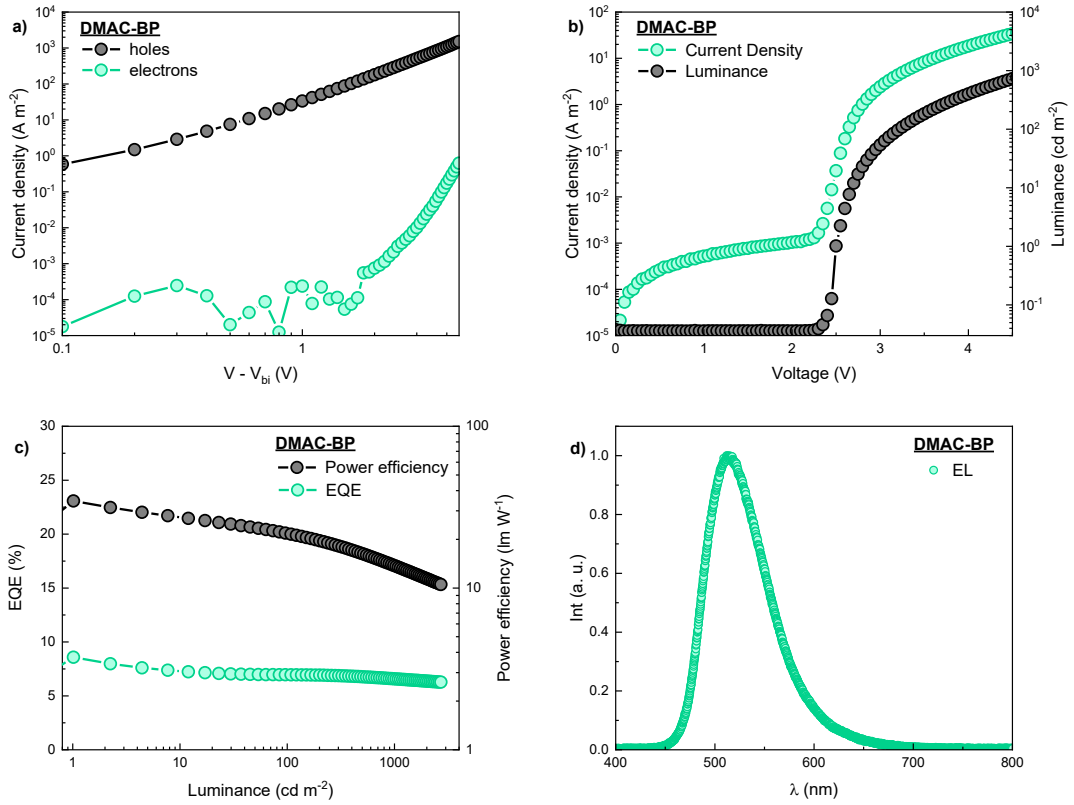

Figure 5.1. (a) Current-density vs. voltage (*J-V*) characteristics for electrons (green symbols) and holes (black symbols) for a pristine DMAC-BP film of 100 nm thickness. The electron-only device was corrected for a built-in voltage of $V_{bi} = 0.68$ V. (b) Current density (green symbols) and luminance (black symbols) vs voltage for a single-layer DMAC-BP OLED with 144 nm thickness. (c) External quantum efficiency (EQE) (green symbols) and power efficiency (black symbols) for a single-layer DMAC-BP OLED.

In Chapter 2, a bottom-up strategy was presented to avoid trapping in organic semiconductors with a band gap larger than 2.5 eV. By spatially separating the HOMO and LUMO orbitals and tuning the stacking of the molecules by chemical modification, the LUMO orbitals can be spatially protected from electron-trapping impurities. For the compound 9,9',9"-(5-(4,6-diphenyl-1,3,5-triazin-2-yl)benzene-1,2,3-triyl)tris(9*H*-carbazole) (3CzTRZ), the electron current was observed to be nearly trap-free, in spite of the LUMO being outside the trap-free window.[43] Such a large band gap trap-free organic semiconductor is ideally suited to be used as a host for TADF emitters with unbalanced transport, such as DMAC-BP.

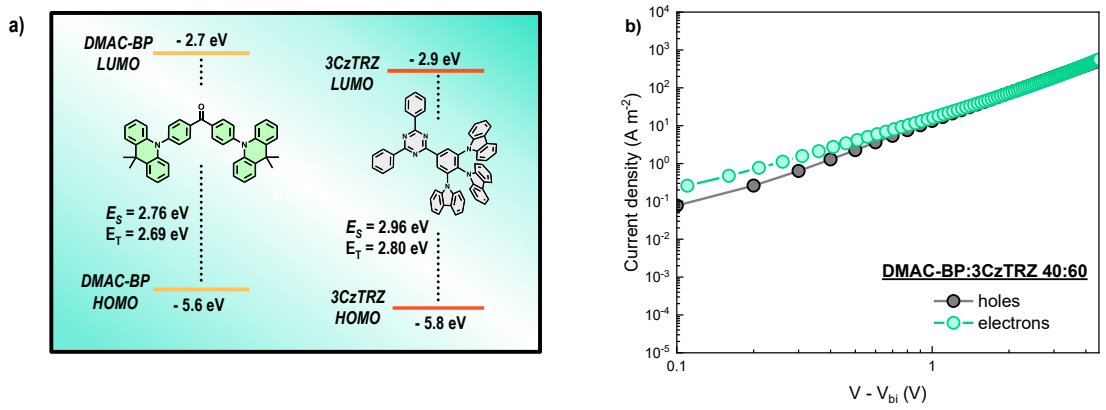

Figure 5.2. (a) Energy band diagram of DMAC-BP and 3CzTRZ and indicated singlet and triplet levels.[37,45] (b) Current-density vs. voltage (*J-V*) characteristics for electrons (green symbols) and holes (black symbols) for a film consisting of a 40:60 DMAC-BP:3CzTRZ blend of 70 nm thickness. The electron-only was corrected for a built-in voltage of V_{bi} = 0.69 V.

In **Figure 5.2a** the energy levels of DMAC-BP and 3CzTRZ are schematically indicated. 3CzTRZ has a HOMO level of -5.8 eV and a LUMO level of -2.9 eV.[43] In a DMAC-BP:3CzTRZ blend in near equal ratios, the electron transport will take place in the 3CzTRZ, whereas the hole transport is governed by the DMAC-BP, resulting in nearly trap-free transport for both carriers. The offset between the LUMO levels was verified using inverse photoelectron spectroscopy (IPES) (**Figure A4.4**).[44] In **Figure 5.2b** the electron and hole current for a 40:60 DMAC-BP:3CzTRZ blend are shown. For this blend ratio, the electron and hole transport is perfectly balanced and nearly trap-free, as evidenced by the quadratic dependence of the current on voltage, characteristic of a trap-free space-charge-limited current. The applied voltage for the electron-only device was corrected for a built-in voltage of V_{bi} = 0.69 eV. When the amount of DMAC-BP is further reduced to 10% the electron current in the 3CzTRZ becomes dominant over the hole current in the strongly diluted DMAC-BP, again resulting in unbalanced transport (now electron dominated), see Figure A5.1.

As a next step, OLEDs based on the 40:60 DMAC-BP:3CzTRZ blend with a PEDOT:PSS:PFI anode and TPBi(4 nm)/Ba/Al cathode were fabricated. In **Figure 5.3** the *J-V* and *L-V* (a) characteristics are shown, together with the EQE and power efficiency (**Figure 5.3b**). As shown in **Figure 3b**, the maximum EQE of the 40:60 DMAC-BP:3CzTRZ blend OLED is strongly enhanced up to 19.6% for the optimal layer thickness (see **Figure A5.6** and **A5.7**). This EQE is similar to the reported values in the range of 19-21% for multilayer OLEDs with DMAC-BP as the emitter.[37–39] However, the reduced operating voltage of the single-layer device due to the absence of charge blocking layers, reaching 1000 cd m^{-2} already at 2.95 V, results in a superior maximum power efficiency of 82 lm W^{-1} and 77.8

lm W^{-1} at a luminance of 100 cd m^{-2}. The single-layer OLED strongly outperforms the power efficiencies of multilayer OLEDs[37–39], with the maximum reported value being 59 lm W^{-1} at 100 cd m^{-2}.[37] Even at a high luminance of 5,000 cd m^{-2}, the power efficiency is still 41.7 lm W^{-1}, which is higher than the best reported value of 25.7 lm W^{-1} at the same luminance, the latter being achieved for a multilayer device using DMIC-TRZ as a host for DMAC-BP in the emissive layer.[39] In **Figure 5.4a** schematics of the device structure and (power) efficiencies of the various OLEDs are shown for comparison. This result demonstrates that single-layer OLEDs are capable of outperforming multilayer devices employing the same TADF emitter.

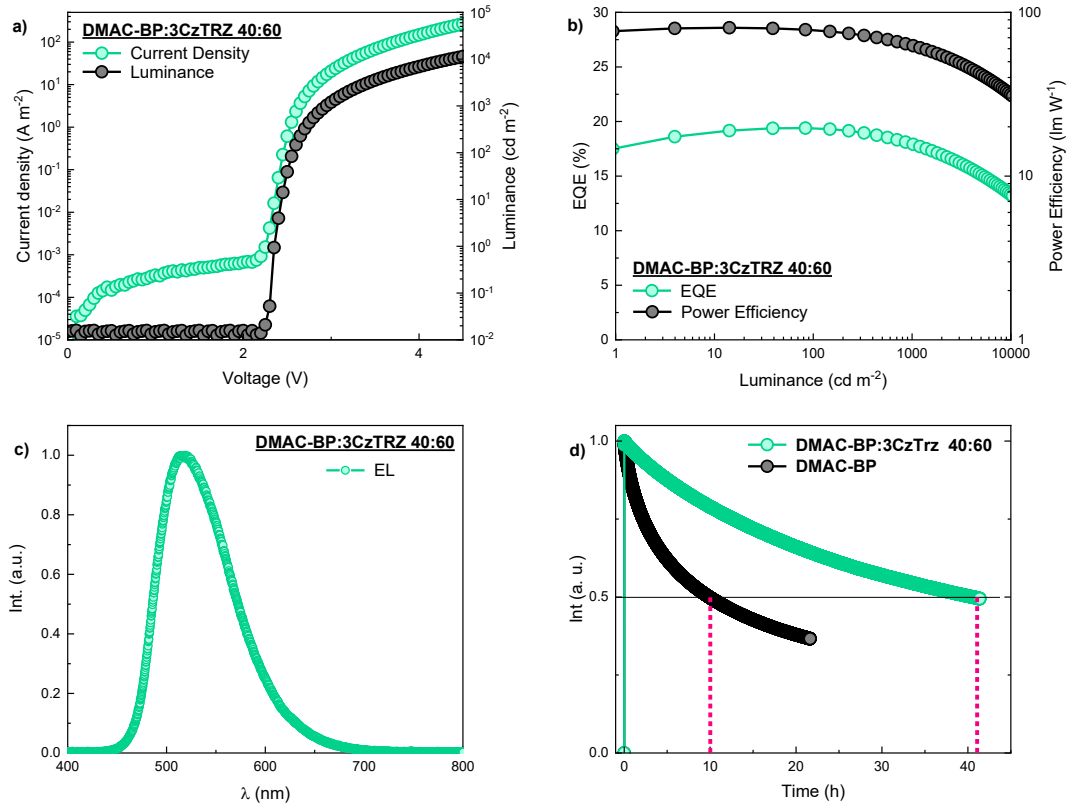

Figure 5.3. a) Current density (green symbols) and luminance (black symbols) vs voltage for a 40:60 DMAC-BP:3CzTRZ blend OLED with 70 nm thickness. b) External quantum efficiency (EQE) (greensymbols) and power efficiency (black symbols) for the 40:60 DMAC-BP:3CzTRZ blend OLED. c) The observed electroluminescence spectrum for the DMAC-BP:3CzTRZ 40:60 based OLED d) Lifetime measurements of pure DMAC-BP and DMAC-BP:3CzTRZ (40:60) at 1000 cd m^{-2} initial luminance.

The use of a trap-free host to achieve balanced charge transport not only positively affects the efficiency, but also the lifetime. As shown in **Figure 5.3d**, the LT_{50} lifetime of the 40:60 DMAC-BP:3CzTRZ blend OLED reaches 41 hours at an initial luminance of 1,000 cd m^{-2}, while the single-layer OLED based on neat DMAC-BP achieves a lifetime of 10 hours. In a multilayer OLED, a lifetime of under 4 hours has been reported for non-doped DMAC-BP, while the lifetime is limited to only 30 minutes when using a conventional host.[37] As a result, it is demonstrated that both the use of 3CzTRZ as a host, as well as the use of the single-layer device concept vastly improves the device stability, which is believed to originate from the broadening of the emission zone.

When reducing the emitter concentration, the charge transport becomes electron dominated. This is expected, since hole-transport takes place on DMAC-BP, and a lower concentration reduces guest-to-guest hopping. For OLEDs consisting of a 10:90 DMAC-BP:3CzTRZ blend the performance decreases due to the loss of the balanced transport (**Figure A5.1**). However, with a maximum EQE of 14% these OLEDs still outperform the pristine DMAC-BP OLEDs. The reason is that in the electron-dominated 10:90 DMAC-BP:3CzTRZ OLED the recombination zone is far away from the metallic cathode and close to the PEDOT:PSS:PFI anode, resulting in lower losses due to coupling of photons to surface-plasmon modes. On the other hand, in a 50:50 ratio, the OLED becomes slightly hole dominated (**Figure A5.2**). The slight loss of charge balance reduces the EQE compared to the optimum 40:60 DMAC-BP:3CzTRZ ratio.

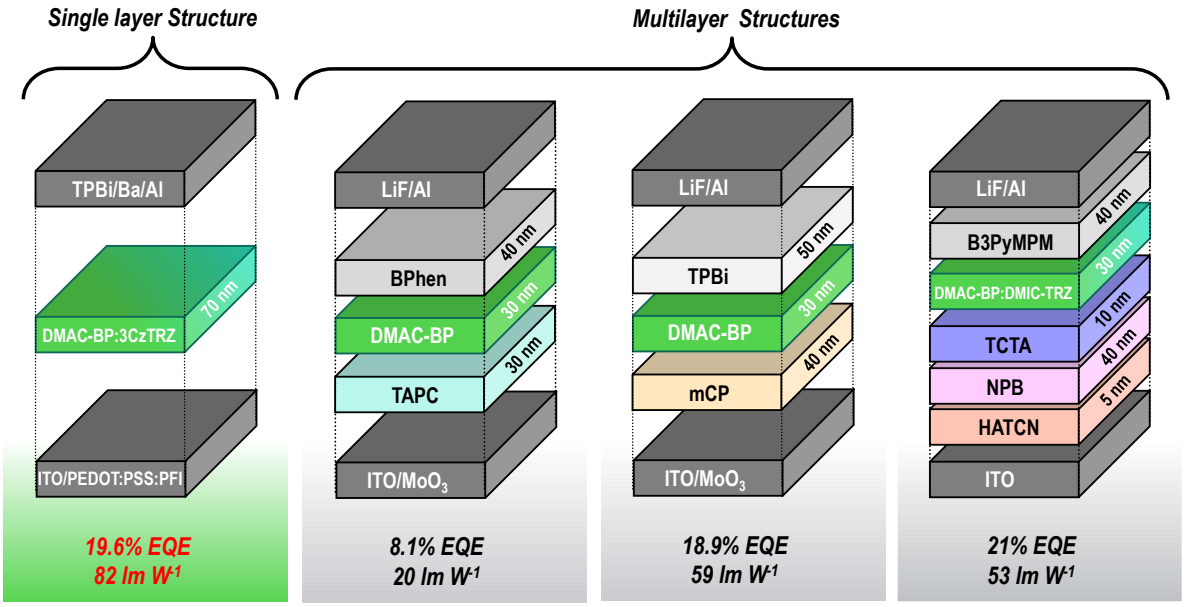

Figure 5.4. Schematic diagram of the single-layer OLED used in this study and multilayer OLEDs reported in literature with the corresponding maximum EQE and maximum power efficiency.

To further investigate the relevance of the use of a trap-free large band gap host like 3CzTRZ, as a reference a single-layer OLED using the well-known wide-gap host 9-(3-(9*H*-carbazol-9-yl)phenyl)-9*H*-carbazole-3-carbonitrile (mCPCN) is investigated, using a blend ratio of 1:1 with DMAC-BP.[41,46,47] For the host mCPCN with the HOMO at -5.80 eV and LUMO at -2.24 eV the electron and hole transport will both take place on DMAC-BP, resulting again in imbalanced transport. As shown in **Figure 5.5a** the electron and hole transport is indeed strongly unbalanced, although the balance is improved as compared to pristine DMAC-BP. This might be the result of the trap-dilution effect that modifies the statistics between free and trapped carriers.[48] The resulting EQE and power efficiency of the DMAC-BP:mCPCN (**Figure 5.5b**) are therefore in between those of the pristine DMAC-BP and 40:60 DMAC-BP:3CzTRZ devices, amounting to a maximum of 13% and 50 lm W^{-1}, respectively. However, the reduced charge transport has a strong negative impact on the operating voltage. As a result, the power efficiency only amounts to 15.0 lm W^{-1} at a luminance of 100 cd m^{-2}. This result confirms the relevance of applying a trap-free host to obtain balanced transport and high power efficiency in TADF OLEDs.

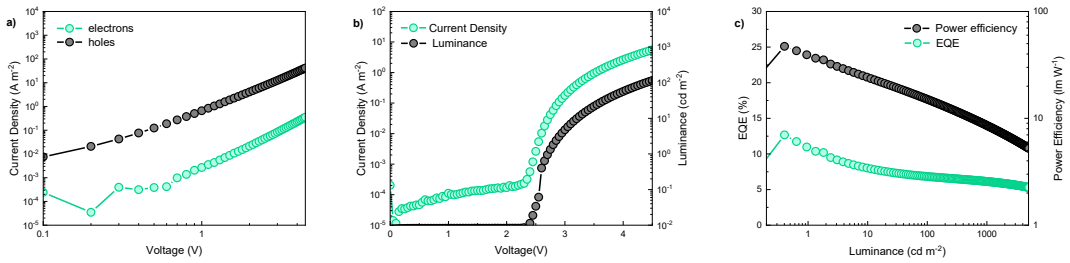

Figure 5.5. (a) Current-density vs. voltage (*J-V*) characteristics for electrons (green symbols) and holes (black symbols) for a film consisting of a DMAC-BP:mCPCN 1:1 blend of 94 nm thickness. The applied voltage for the electron-only device was corrected for a built-in voltage of V_{bi} = 0.70 V. (b) External quantum efficiency (EQE) (green symbols) and power efficiency (black symbols) for a single layer DMAC-BP:mCPCN 1:1 OLED.

The use of 2CzTRZ as a host was investigated, too. 2CzTRZ has a similar LUMO energy as 3CzTRZ, but shows some electron trapping.[43] As a result, electron transport takes place via 2CzTRZ, so that the impact of electron trapping in the host material can be investigated. As shown in **Figure A5.8**, the electron transport is clearly lower than the hole transport at low voltage, which is due to electron trapping. Since the electron-trap density in 2CzTRZ is still in the lower range for organic semiconductors, a transition to the trap-filled limit occurs at a voltage within the OLED operation window. Therefore, at higher voltages the charge transport becomes balanced. This is also reflected in the EQE (**Figure A5.9**) of the single-layer OLED of the DMAC-BP:2CzTRZ blend, which is low at

low luminance due charge imbalance, while it increases to decent levels at higher luminance due to more balanced transport. It is noted that for host with more severe trapping, as is common in organic semiconductors, the EQE will be heavily compromised.

5.3 Conclusion

In conclusion, it was demonstrated that a trap-free wide band gap organic semiconductor such as 3CzTRZ can be used to achieve balanced charge transport in intrinsically trap-limited emitters such as DMAC-BP. Balanced charge transport is a prerequisite for the use of organic emitters in a single-layer OLED to attain a decent device performance. It was demonstrated that single-layer OLEDs employing a trap-free host can surpass the performance of current multilayer OLED architectures, by virtue of a lower operating voltage due to improved charge transport and the absence of heterojunctions within the stack. Exhibiting a similar EQE to multilayer devices, the lower operating voltage results in drastically improved power efficiencies. The obtained power efficiency (max 82 lm W^{-1}) represents a record for DMAC-BP OLEDs, being almost 40% higher than the next most efficient reported device. In addition, it was demonstrated that also the operational stability is greatly improved, due to a better spreading of the emission zone. These results cannot be achieved with conventional host materials, which characteristically exhibit trap-limited charge transport of at least one type of charge carrier, with electron trapping being the most common case.

References

[1] M. A. Baldo, D. F. O'Brien, Y. You, A. Shoustikov, S. Sibley, M. E. Thompson, S. R. Forrest, *Nature* **1998**, *395*, 151.

[2] K. Walzer, B. Männig, M. Pfeiffer, K. Leo, *Chem. Rev.* **2007**, *107*, 1233.

[3] M. Furno, R. Meerheim, S. Hofmann, B. Lüssem, K. Leo, *Phys. Rev. B - Condens. Matter Mater. Phys.* **2012**, *85*, 1.

[4] H. Sasabe, N. Toyota, H. Nakanishi, T. Ishizaka, Y. J. Pu, J. Kido, *Adv. Mater.* **2012**, *24*, 3212.

[5] J. Kido, M. Kimura, K. Nagai, *Science (80-.).* **1995**, *267*, 1332.

[6] J. A. Seo, S. K. Jeon, M. S. Gong, J. Y. Lee, C. H. Noh, S. H. Kim, *J. Mater. Chem. C* **2015**, *3*, 4640.

[7] C. H. Shih, P. Rajamalli, C. A. Wu, W. T. Hsieh, C. H. Cheng, *ACS Appl. Mater. Interfaces* **2015**, *7*, 10466.

[8] H. Uoyama, K. Goushi, K. Shizu, H. Nomura, C. Adachi, *Nature* **2012**, *492*, 234.

[9] S. O. Jeon, K. H. Lee, J. S. Kim, S. G. Ihn, Y. S. Chung, J. W. Kim, H. Lee, S. Kim, H. Choi, J. Y. Lee, *Nat. Photonics* **2021**, *15*, 208.

[10] L. S. Cui, A. J. Gillett, S. F. Zhang, H. Ye, Y. Liu, X. K. Chen, Z. Sen Lin, E. W. Evans, W. K. Myers, T. K. Ronson, H. Nakanotani, S. Reineke, J. L. Bredas, C. Adachi, R. H. Friend,

Nat. Photonics **2020**, *14*, 636.

[11] J. Sun, H. Ahn, S. Kang, S. B. Ko, D. Song, H. A. Um, S. Kim, Y. Lee, P. Jeon, S. H. Hwang, Y. You, C. Chu, S. Kim, *Nat. Photonics* **2022**, *16*, 212.

[12] L. Duan, D. Zhang, K. Wu, X. Huang, L. Wang, Y. Qiu, *Adv. Funct. Mater.* **2011**, *21*, 3540.

[13] S. J. Lee, J. R. Koo, H. W. Lee, S. E. Lee, H. J. Yang, S. S. Yoon, J. Park, Y. K. Kim, *Electron. Mater. Lett.* **2014**, *10*, 1127.

[14] S. J. Lee, S. E. Lee, D. H. Lee, J. R. Koo, H. W. Lee, S. S. Yoon, J. Park, Y. K. Kim, *Jpn. J. Appl. Phys.* **2014**, *53*.

[15] T. H. Han, Y. H. Kim, M. H. Kim, W. Song, T. W. Lee, *ACS Appl. Mater. Interfaces* **2016**, *8*, 6152.

[16] J. S. Bangsund, K. W. Hershey, D. C. K. Rathwell, H. Y. Na, J. H. Jeon, P. Trefonas, R. J. Holmes, *J. Soc. Inf. Disp.* **2019**, *27*, 434.

[17] B. Van Der Zee, Y. Li, G. J. A. H. Wetzelaer, P. W. M. Blom, *Phys. Rev. Appl.* **2022**, *18*, 064002.

[18] R. Coehoorn, H. Van Eersel, P. A. Bobbert, R. A. J. Janssen, *Adv. Funct. Mater.* **2015**, *25*, 2024.

[19] C. Zhao, L. Duan, *J. Mater. Chem. C* **2020**, *8*, 803.

[20] R. Mac Ciarnáin, H. W. Mo, K. Nagayoshi, H. Fujimoto, K. Harada, R. Gehlhaar, T. H. Ke, P. Heremans, C. Adachi, *Adv. Mater.* **2022**, *34*, 2201409.

[21] T. Y. Cheng, J. H. Lee, C. H. Chen, P. H. Chen, P. S. Wang, C. E. Lin, B. Y. Lin, Y. H. Lan, Y. H. Hsieh, J. J. Huang, H. F. Lu, I. Chao, M. Leung, T. L. Chiu, C. F. Lin, *Sci. Rep.* **2019**, *9*, 3654.

[22] J. Wu, L. Ameri, L. Cao, J. Li, *Appl. Phys. Lett.* **2021**, *118*, 073301.

[23] T. Xu, M. Yang, J. Liu, X. Wu, I. Murtaza, G. He, H. Meng, *Org. Electron.* **2016**, *37*, 93.

[24] M. E. Kondakova, T. D. Pawlik, R. H. Young, D. J. Giesen, D. Y. Kondakov, C. T. Brown, J. C. Deaton, J. R. Lenhard, K. P. Klubek, *J. Appl. Phys.* **2008**, *104*, 094501.

[25] S. J. Cha, Y. R. Cho, M. C. Suh, *Synth. Met.* **2015**, *200*, 143.

[26] J. Lee, J. I. Lee, J. Y. Lee, H. Y. Chu, *Appl. Phys. Lett.* **2009**, *94*, 193305.

[27] B. Van der Zee, Y. Li, G. J. A. H. Wetzelaer, P. W. M. Blom, *Adv. Mater.* **2022**, *34*, 2108887.

[28] M. Kuik, L. J. A. Koster, A. G. Dijkstra, G. A. H. Wetzelaer, P. W. M. Blom, *Org. Electron.* **2012**, *13*, 969.

[29] I. Rörich, A. K. Schönbein, D. K. Mangalore, A. Halda Ribeiro, C. Kasparek, C. Bauer, N. I. Crăciun, P. W. M. Blom, C. Ramanan, *J. Mater. Chem. C* **2018**, *6*, 10569.

[30] Y. Li, N. B. Kotadiya, B. van der Zee, P. W. M. Blom, G. J. A. H. Wetzelaer, *Adv. Opt. Mater.* **2021**, *9*, 2001812.

[31] N. B. Kotadiya, A. Mondal, P. W. M. Blom, D. Andrienko, G. J. A. H. Wetzelaer, *Nat. Mater.*

2019, *18*, 1182.

[32] G. J. A. H. Wetzelaer, P. W. M. Blom, *ACS Appl. Mater. Interfaces* **2022**, *14*, 7523.

[33] R. Meerheim, M. Furno, S. Hofmann, B. Lüssem, K. Leo, *Appl. Phys. Lett.* **2010**, *97*, 253305.

[34] C. Fuchs, P. A. Will, M. Wieczorek, M. C. Gather, S. Hofmann, S. Reineke, K. Leo, R. Scholz, *Phys. Rev. B - Condens. Matter Mater. Phys.* **2015**, *92*, 245306.

[35] N. B. Kotadiya, H. Lu, A. Mondal, Y. Ie, D. Andrienko, P. W. M. Blom, G. J. A. H. Wetzelaer, *Nat. Mater.* **2018**, *17*, 329.

[36] N. B. Kotadiya, P. W. M. Blom, G. J. A. H. Wetzelaer, *Nat. Photonics* **2019**, *13*, 765.

[37] Q. Zhang, D. Tsang, H. Kuwabara, Y. Hatae, B. Li, T. Takahashi, S. Y. Lee, T. Yasuda, C. Adachi, *Adv. Mater.* **2015**, *27*, 2096.

[38] X. Jiang, H. Lin, C. Xue, G. Zhang, W. Jiang, G. Xing, *J. Mater. Sci. Mater. Electron.* **2020**, *31*, 19136.

[39] D. Zhang, C. Zhao, Y. Zhang, X. Song, P. Wei, M. Cai, L. Duan, *ACS Appl. Mater. Interfaces* **2017**, *9*, 4769.

[40] T. W. Lee, Y. Chung, O. Kwon, J. J. Park, *Adv. Funct. Mater.* **2007**, *17*, 390.

[41] O. Sachnik, Y. Li, X. Tan, J. J. Michels, P. W. M. Blom, G. A. H. Wetzelaer, *Adv. Mater.* **2023**, 2300574.

[42] G. Cnossen, K. E. Drabe, D. A. Wiersma, *J. Cherm. Phys.* **1993**, *98*, 5276.

[43] O. Sachnik, X. Tan, D. Dou, C. Haese, N. Kinaret, K.-H. Lin, D. Andrienko, M. Baumgarten, R. Graf, G.-J. A. H. Wetzelaer, J. J. Michels, P. W. M. Blom, *Nat. Mater.* **2023**.

[44] N. V Smith, *Rep. Prog. Phys.* **1988**, *51*, 1227.

[45] D. R. Lee, M. Kim, S. K. Jeon, S. H. Hwang, C. W. Lee, J. Y. Lee, *Adv. Mater.* **2015**, *27*, 5861.

[46] M. S. Lin, S. J. Yang, H. W. Chang, Y. H. Huang, Y. T. Tsai, C. C. Wu, S. H. Chou, E. Mondal, K. T. Wong, *J. Mater. Chem.* **2012**, *22*, 16114.

[47] W. Zeng, H. Y. Lai, W. K. Lee, M. Jiao, Y. J. Shiu, C. Zhong, S. Gong, T. Zhou, G. Xie, M. Sarma, K. T. Wong, C. C. Wu, C. Yang, *Adv. Mater.* **2018**, *30*, 1704961.

[48] D. Abbaszadeh, A. Kunz, G. A. H. Wetzelaer, J. J. Michels, N. I. Craciun, K. Koynov, I. Lieberwirth, P. W. M. Blom, *Nat. Mater.* **2016**, *15*, 628.

6. Summary

Organic semiconductors offer a variety of modifications to their chemical structure. This makes them attractive to be used as active layers in electronic devices, such as photovoltaics, light-emitting diodes and field-effect transistors. One of the most important commercial application for organic semiconductors are organic light-emitting diodes. Although being established as a technology, OLEDs can be still improved in terms of lifetime and efficiency. For this, it is of fundamental interest to understand the intrinsic charge transport in organic semiconductors. The scope of this thesis was to understand how the chemical structure can be modified to design materials, that exhibit band gaps of ≥ 3.0 eV with no charge trapping of holes and electrons.

In chapter 2, a design strategy was presented, which exemplified, how charge trapping can be effectively deactivated in organic semiconductors. In this chapter, a material (3CzTRZ) with trap-free hole and electron transport was identified, while exhibiting a sufficiently large bandgap of ~ 3.0 eV. Next to balanced charge transport, 3CzTRZ features thermally activated delayed fluorescence, being capable of theoretically harvesting all generated singlet and triplet excitons in an organic light-emitting diode.

In chapter 3, a material, which is structurally comparable to 3CzTRZ, was examined and employed in a single-layer blue OLED. SpiroAc-TRZ features a similar donor-acceptor structure with comparably low number of electron and hole traps. Employing SpiroAc-TRZ in a single-layer OLED, resulted in a high external quantum efficiency of 27.7%. Optical simulations revealed that the internal quantum efficiency approaches unity.

Despite having excellent charge transport properties, TRPL measurements in chapter 4 revealed, that 3CzTRZ suffers from a low reverse intersystem crossing rate, comparable to the rate of non-radiative recombination of triplet excitons to the ground state. It was shown, that the incorporation of 3CzTRZ in a large band gap host, increases the triplet lifetime by at least one order of magnitude, boosting the EQE in an OLED from 4.5% (pure material) to 15% (diluted in host).

While being limited in the reverse intersystem crossing rate, 3CzTRZ offers a high singlet and triplet energy, which makes it a potential host candidate for smaller band gap emitters. For this purpose, DMAC-BP, a green emitter with trap-limited electron transport was chosen in chapter 5. Employing 3CzTRZ as a host-material for DMAC-BP, the electron transport could be improved by several orders of magnitude, leading to balanced charge transport characteristics inside the device. This resulted in excellent external quantum efficiencies, improved power efficiencies and lifetimes, that were unknown

for DMAC-BP so far. This study demonstrated, that 3CzTRZ can be an excellent host-material for future compounds suffering from poor electron transport.

7. Experimental methods

7.1 Device fabrication

7.1.1 Device cleaning

Cleaning was performed prior to device fabrication inside a clean room. Substrates were individually cleaned by scrubbing with detergent solution (Extran® MA 02, Merck KGaA) for 1 min and thoroughly rinsed with deionized water. The substrates were submerged in a deionized water bath at 40 °C for 5 min and subsequently ultrasonicated in acetone and isopropyl alcohol for 5 min, respectively. The substrates were blown dry and heated in an oven (HORO Dr. Hofmann GmbH) at 135 °C for 10 min. In a last step, the substrates were treated with UV-ozone for 45 min.

7.1.2 PEDOT:PSS modification

PFI-containing blends were prepared 24 h prior to device fabrication by mixing PEDOT:PSS (CLEVIOS P VP AI 4083) with Nafion® in a 1:6:14 ratio and diluted in deionized water (1:1). PEDOT:PSS:PFI was applied by spin coating, resulting in films of 20 nm thickness, which were subsequently annealed at 130 °C for 12 min.

7.1.3 Device fabrication

For hole-only and OLED devices, a hole-injection layer consisting of PEDOT:PSS:PFI was spincoated on freshly cleaned ITO substrates (**Figure 7.1a**). The substrates were fully covered with PEDOT:PSS:PFI dispersion and spincoating was performed for 3 s at 2000 rpm speed and 2000 rpm acceleration and 60 s at 3000 rpm speed and 1000 rpm acceleration to afford a thickness of 20 nm (**Figure 7.1b**). The PEDOT:PSS:PFI covered substrates were heated in an oven at 135 °C for 13 min.

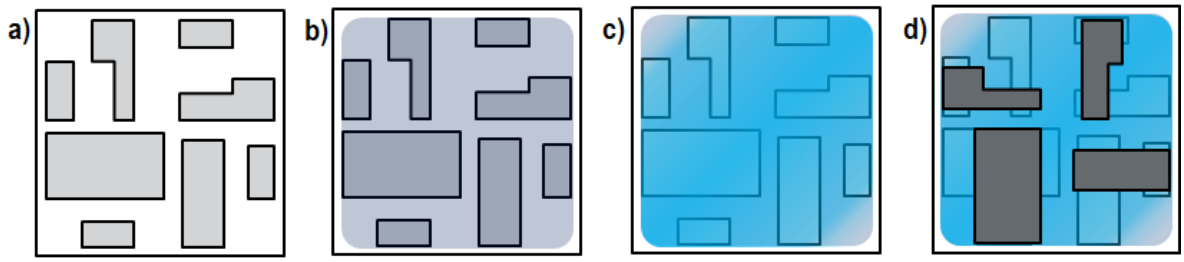

Figure 7.1. Hole-only and OLED device fabrication. a) UV-Ozone treated ITO substrate b) PEDOT:PSS:PFI spincoated on ITO substrate c) Thermally evaporated organic semiconductor d) Thermally evaporated metallic contacts.

The substrates were transferred into a nitrogen-filled glove box after annealing. Thermal evaporation of organic materials (**Figure 7.1c**) was performed at a base pressure of ~2×10^{-6} mbar inside an organic evaporator (COAT340-ORG, Vactec B. V.). Thin tunneling interlayers such as TPBi (3 nm) for OLEDs and C_{60} (4 nm) for hole-onlys were subsequently evaporated. OLEDs were capped with Barium (3 nm) and Aluminium (100 nm) inside an inorganic evaporator (COAT340, Vactec B. V.) using a shadow mask to form the top electrode (**Figure 7.1d**). Hole-only devices were capped with MoO_3 (7 nm) and Aluminium (100 nm) using a shadow mask to form the top electrode (**Figure 7.1d**).

For electron-only devices, freshly cleaned glass substrates were used. Aluminium (30 nm) was thermally evaporated using a shadow mask to form the bottom electrode (**Figure 7.1a**). The substrates were subsequently oxidized in air for 5 min. The substrates were transferred back into the thermal evaporater and the organic layer and TPBi tunneling interlayer (4 nm) were deposited (**Figure 7.1b**). The device was finished with a Barium (3 nm) and Aluminium (100 nm) capping layer (**Figure 7.1c**).

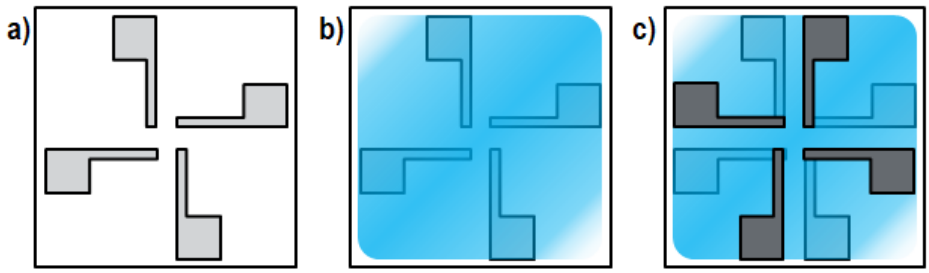

Figure 7.2. Electron-only device fabrication. a) Clean glass substrate with thermally evaporated aluminum contact b) Thermally evaporated organic semiconductor d) Thermally evaporated metallic contacts.

7.1.4 Device measurement

Electrical characterization was carried out under nitrogen atmosphere with a Keithley 2400 source meter and light output was recorded with a Si photodiode with NIST-traceable calibration, with a detector area (1 cm^2) larger than the emitting area of the OLED (0.16 cm^2). The photodiode was placed close to (but not in contact with) the OLED to capture all photons emitted in a forward hemisphere. To avoid any light detection emitted from the substrate edges, the edges were masked by the sample holder and the substrate size (3 × 3 cm^2) was considerably larger than the photodetector area. The EQE, the luminance and power efficiency were calculated from the measured photocurrent, the device current, and the electroluminescence spectrum. Electroluminescence spectra were obtained with a USB4000-UV-VIS-ES spectrometer.

7.2 NMR measurements

7.2.1 Solution NMR

All solution NMR spectra (^{1}H, $^{13}C\{H\}$,^{19}F) were measured using a Bruker Avance III setup at 700.25 MHz ^{1}H Larmor frequency and were performed at 298 K with deuterated tetrachloroethane if not differently specified. Chemical shift values δ are given in ppm und coupling constants J are given in Hz. The multiplicity of signals is described using following shortcuts: s (singlet), d (doublet), dd (doublet of doublets), t (triplet), q (quartet), m (multiplet).

7.2.2 Solid-state NMR

Solid samples were packed into Bruker BioSpin zirconia rotors with 1.3 mm outer diameter. ^{1}H MAS NMR spectra were acquired with 4 scans of direct excitation using a 2.0 µs 90 degree excitation pulse and a recycle delay of 30 s on a Bruker Avance NEO spectrometer operating at 850.27 MHz ^{1}H Larmor frequency at a MAS spinning speed of 50 kHz. ^{19}F MAS NMR spectra were acquired with 16 scans of direct excitation using a 2.5 µs 90 degree excitation pulse and a recycle delay of 30 s on a Bruker Avance III spectrometer at 470.61 MHz ^{19}F Larmor frequency and 25 kHz MAS spinning frequency.

7.3 Determination of energy levels

7.3.1 Photoelectron Spectroscopy

Ionization energies were measured with an atmospheric photoemission yield spectrometer (AC-2) from Riken Keiki Co., Ltd. The sample was dissolved in DCM (5 mg/mL) and dropcasted on freshly cleaned ITO substrates.

7.3.2 Cyclic Voltammetry (CV)

Cyclic voltammetry was carried out on a computer-controlled GSTAT12 in a three-electrode cell in anhydrous acetonitrile solution of *n*-Bu4NPF6 (0.05 M) with a scan rate of 100 mV/s at room temperature under argon. Pt wires were used as the counter and working electrodes, a silver wire applied was as reference electrode.

7.4 Mass spectrometry

Matrix-assisted laser desorption ionization with time-of-flight analysis was performed on a rapifleX MALDI-ToF/ToF from Bruker. Atmospheric pressure chemical ionization (APCI) MS was recorded with atmospheric pressure solids analysis probe (ASAP) using an Advion expression compact mass spectrometer (CMS).

7.5 Spectroscopy

7.5.1 Photoluminescence spectroscopy

Photoluminescence spectra were recorded with a HORIBA Jobin-Yvon Fluorolog 3-22 Tau-3 incorporating a PMT (photomultiplier tube) detector. FluorEssence (version 3.9.0.1) was used as software.

7.5.2 UV-Vis absorption spectroscopy

A Perkin Elmer Lambda 900 UV/Vis/NIR spectrometer was used for measurement of ultraviolet-visible (UV-Vis) absorption spectra. For recording and analysis Perkin Elmer UV Winlab (Version: 6.04.0738) was used.

7.5.3 Photoluminescence quantum yield (PLQY)

Photoluminescence quantum yields were determined using the Fluorolog-3 and an integrating sphere (F-3018) from Horiba. In a first step, the excitation wavelength of each sample was measured by UV-Vis. At this excitation wavelength the scattered excitation light intensity was set to ~1 million counts per second (cps) with a neutral-density filter (0.5 – 1%) which is inserted between light source and integrating sphere. After fixing the scattered excitation light, the background light emission of the empty integration sphere was determined using the same parameters. In a next step, the sample was inserted and arranged in a way that light from the light source passes through the sample at an angle of 22.5°. The scattered excitation light and photoluminescence of the sample were captured and the sample was rotated to 90°. Scattered excitation light and photoluminescence were recorded as well for this configuration.

7.6 Commercial materials

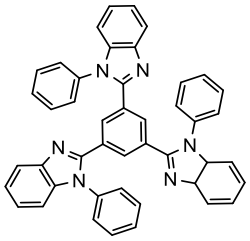

TPBi

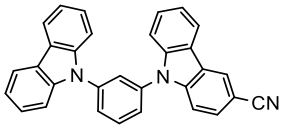

mCP-CN

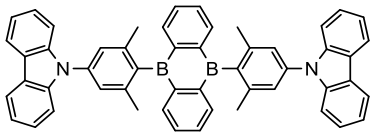

CzDBA

C_{60}

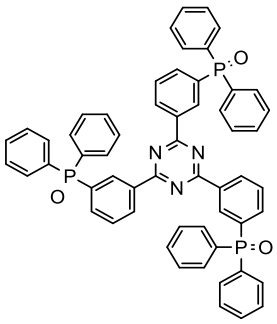

POT2T

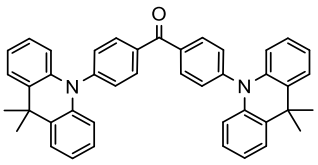

DMAC-BP

Nafion® (PFI) was purchased from Sigma Aldrich as 5 wt.% solution in a mixture of lower aliphatic alcohols and water, containing 45% water. Commercial materials such as **DMAC-BP**, **mCPCN**, **POT2T**, **C_{60}** and **TPBi** were purchased in sublimed grade from Ossila BV (Netherlands) and **CzDBA** was purchased in sublimed grade from LumTec (Taiwan). The full names are as follows: **TPBi**: 2,2'-(5-(1-phenyl-3a,7a-dihydro-1*H*-benzo[d]imidazol-2-yl)-1,3-phenylene)bis(1-phenyl-1*H*-benzo[d]imidazole), **mCPCN**: 9-(3-(9*H*-carbazol-9-yl)phenyl)-9H-carbazole-3-carbonitrile, **DMAC-BP**: bis(4-(9,9-dimethylacridin-10(9*H*)-yl)phenyl)methanone, **CzDBA**: 5,10-bis(4-(9*H*-carbazol-9-yl)-2,6-dimethylphenyl)-5,10-dihydroboranthrene, **C_{60}**: Fullerene-C_{60}, **POT2T**: ((1,3,5-triazine-2,4,6-triyl)tris(benzene-3,1-diyl))tris(diphenylphosphine oxide)

7.7 Synthesis

Chemicals and solvents for synthetic operations were purchased from common suppliers (Sigma-Aldrich, Fisher Scientific, VWR etc.) and were used as received. All reactions were performed under an argon atmosphere and in dry solvents if not specifically depicted. Glassware was heated and evacuated before use for three times. Details for reactions are given in the following instructions.

7.7.1 Introduction of carbazole in fluorobenzenes

A mixture of carbazole (3 Cz: 3 eq., 2 Cz: 2 eq., 1 Cz: 1 eq.) and Cs_2CO_3 (3 Cz: 4 eq., 2 Cz: 2.5 eq., 1 Cz: 5.0 eq.) was placed in a two necked flame-dried flask under an argon atmosphere, suspended in DMF and stirred at room temperature for 30 min, followed by addition of corresponding fluorobenzene (3 Cz: 1 eq., 2 Cz: 1 eq., 1 Cz: 2 eq.) and heating to 175 °C for 24 h (1 Cz: 72h). After cooling to room temperature, the reaction mixture was poured on water and the water phase was extracted three times with dichloromethane (DCM). The combined organic phases were washed with brine solution and dried over $MgSO_4$. The solvent was evaporated under reduced pressure and the crude product was purified by column chromatography (stationary phase: silica, eluent: hexane/DCM 4:1).

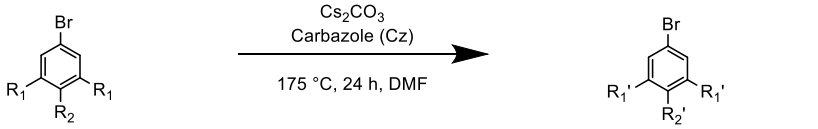

1CzTrz(-F): R_1 = Me, R_2 = F
2CzTrz(-F): R_1 = F, R_2 = H
3CzTrz(-F): $R_{1,2}$ = F

1CzTrz(-F): R_1' = Me, R_2' = Cz
2CzTrz(-F): R_1' = Cz, R_2' = H
3CzTrz(-F): $R_{1,2}$' = Cz

9-(4-bromo-2,6-dimethylphenyl)-9*H*-carbazole

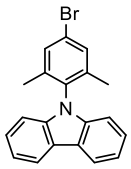

According to the general procedure 5-bromo-2-fluoro-1, 3-dimethylbenzene (2.43 g, 12.0 mmol), carbazole (1.01 g, 6.0 mmol) and Cs_2CO_3 (10.50 g, 30.0 mmol) were suspended in DMF (30 mL). The purified product was obtained as a white solid (1.69 g, 81%). ^{1}H NMR [ppm] (700 MHz, $C_2D_2Cl_4$): 8.16 (H^3, d, $J^3_{H\text{-}H}$= 7.7 Hz, 2H), 7.44 (H^2, s, 2H), 7.39 (H^1 ,t, $J^3_{H\text{-}H}$ = 7.7 Hz, 2H), 7.28 (H^2 ,t , $J^3_{H\text{-}H}$ = 7.7 Hz, 2H), 6.93 (H^6 ,d , $J^3_{H\text{-}H}$ = 8 Hz, 2H), 1.82 (H^{11} , s, 6H). ^{13}C NMR [ppm] (176 MHz, $C_2D_2Cl_4$): 140.4, 140.1, 133.8, 131.7, 126.3, 123.0, 122.5, 120.6, 119.8, 109.5, 17.5. APCI calc. for $C_{20}H_{16}BrN$ 349.05, found 350.20.

9,9'-(5-bromo-1,3-phenylene)bis(9*H*-carbazole)

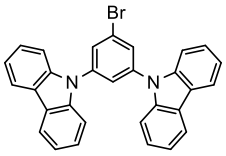

According to the general procedure 1-bromo-3,5-difluorobenzene (0.50 g, 2.6 mmol), carbazole (0.87 g, 5.2 mmol) and Cs_2CO_3 (2.53 g, 7,8 mmol) were suspended in DMF (20 mL). The purified product was obtained as a white solid (0.85 g, 67%). ^{1}H NMR [ppm] (700 MHz, $C_2D_2Cl_4$): 8.17 (d, J^3 = 7.4 Hz, 4H), 7.89 (d. J^4 = 1.5 Hz, 2H), 7.81 (t, J^4 = 1.5 Hz, 1H), 7.59 (d, J^3 = 7.9 Hz, 4H), 7.49 (t, J^3 = 6.7 Hz, 4H), 7.36 (t, J^3 = 6.7 Hz, 4H). ^{13}C NMR [ppm] (176 MHz, $C_2D_2Cl_4$): 140.4, 140.2, 128.6, 126.6, 124.4, 123.7, 121.0, 120.7, 109.8. APCI calc. for $C_{30}H_{19}BrN_2$ 486.07, found 486.90.

9,9',9''-(5-bromobenzene-1,2,3-triyl)tris(9*H*-carbazole)

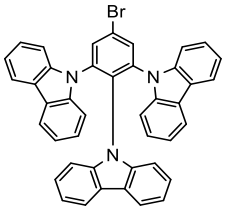

According to the general procedure 5-bromo-1,2,3-trifluorobenzene (1.40 g, 6.6 mmol), carbazole (3.33 g, 19.9 mmol) and Cs_2CO_3 (8.64 g, 26.6 mmol) were suspended in DMF (35 mL). The purified product was obtained as a white solid (2.77 g, 64%). ^{1}H NMR [ppm] (700 MHz, $C_2D_2Cl_4$): 8.1 (d, J^3 = 5.2 Hz, 2H), 7.8 (s, 2H), 7.4 (d, J^3 = 6.8 Hz, 4H), 7.2 (d, J^3 = 7.3 Hz, 4H), 7.1-7.0 (m, 8H), 6.9 (t, J^3 = 7.6 Hz, 2H), 6.8 (t, J^3 = 6.8 Hz, 2H), 6.7 (t, J^3 = 7.0 Hz, 2H). ^{13}C NMR [ppm] (700 MHz, $C_2D_2Cl_4$): 139.7, 138.5, 138.3, 132.8, 131.5, 125.7, 124.9, 123.9, 122.2, 120.5, 120.1, 119.4, 110.0, 109.9. APCI calc. for $C_{42}H_{26}BrN_3$ 651.13, found 651.80.

7.8.2 Formation of boronic acid pinacol esters by Suzuki-coupling

Under an argon atmosphere the bromine substituted aryl compound (1.0 eq) was dissolved together with KOAc (3.2 eq), bis(pinacolato)diboron (1.3 eq) and Pd(dppf)Cl_2 (3.4 mol%) in 1,4-dioxane. The reaction mixture was stirred over night at 110 °C. After cooling to room temperature, the reaction mixture was washed with water. The water phase was extracted three times with DCM. The combined organic phases were dried over $MgSO_4$ and purified by column chromatography (stationary phase: silica, eluent: hexane/ethyl acetate 95:5).

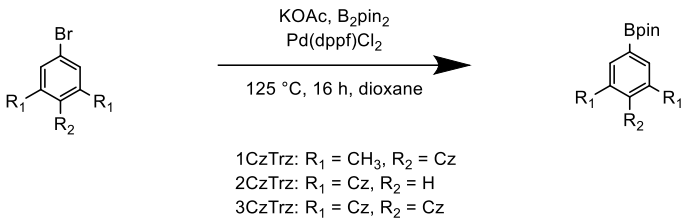

9,9'-(5-(4,4,5,5-tetramethyl-1,3,2-dioxaborolan-2-yl)-1,3-phenylene)bis(9*H*-carbazole)

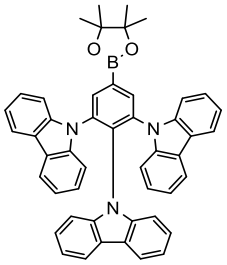

According to the general procedure 9,9',9''-(5-bromobenzene-1,2,3-triyl)tris(9*H*-carbazole) (2.60 g, 3.96 mmol), KOAc (1.24 g, 12.67 mmol), bis(pinacolato)diboron (1.31 g, 5.15 mmol) and Pd(dppf)Cl_2 (95 mg 0.17 mmol) were dissolved in 1,4-dioxane (40 mL). The purified product was obtained as a beige solid (1.40 g, 51%). ^{1}H NMR [ppm] (700 MHz, $C_2D_2Cl_4$): 8.29 (s, 2H), 7.81-7.76 (m, 4H), 7.36 (d, J^3 = 8.8 Hz, 2H), 7.25-7.20 (m, 4H), 7.11-7.00 (m, 10H) 6.76 (t, J^3 = 7.0 Hz, 2H), 6.68 (t, J^3 = 7.0 Hz, 2H), 1.37 (s, 12H). ^{13}C NMR [ppm] (176 MHz, $C_2D_2Cl_4$): 140.2, 138.7, 136.8, 136.1, 134.5, 125.5, 124.7, 123.5, 120.0, 119.9, 119.8, 119.3, 110.3, 110.1, 84.7, 25.1 APCI calc. for $C_{48}H_{38}BN_3O_2$ 699.31, found 699.80.

9,9'-(5-(4,4,5,5-tetramethyl-1,3,2-dioxaborolan-2-yl)-1,3-phenylene)bis(9*H*-carbazole)

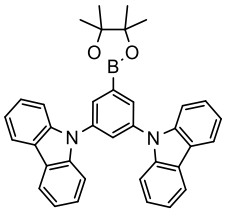

According to the general procedure 9,9'-(5-bromo-1,3-phenylene)bis(9*H*-carbazole) (6.00 g, 12.31 mmol), KOAc (3.87 g, 39.39 mmol), bis(pinacolato)diboron (4.06 g, 16.00 mmol) and Pd(dppf)Cl_2 (310 mg 0.42 mmol) were dissolved in 1,4 dioxane (80 mL). The purified product was obtained as a beige solid (5.11 g, 78%). ^{1}H NMR [ppm] (700 MHz, $C_2D_2Cl_4$): 8.16 (d, J^3 = 7.8 Hz, 4H), 8.10 (d, J^4 = 1.8 Hz, 2H), 7.87 (t, J^4 = 1.8 Hz, 1H), 7.54 (d, J^3 = 7.7 Hz, 4H), 7.46 (t, J^3 = 7.0 Hz, 4H), 7.32 (t. J^3 = 7.0 Hz, 4H), 1.36 (s, 12H). ^{13}C NMR [ppm] (176 MHz, $C_2D_2Cl_4$): 140.7, 138.8, 132.0, 127.7, 126.4, 123.5, 120.6, 120.4, 109.9, 84.6, 25.0. APCI calc. for $C_{36}H_{31}BN_2O_2$ 534.25, found 535.0.

9-(2,6-dimethyl-4-(4,4,5,5-tetramethyl-1,3,2-dioxaborolan-2-yl)phenyl)-9*H*-carbazole

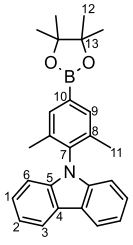

According to the general procedure 9-(4-bromo-2,6-dimethylphenyl)-9*H*-carbazole (1.00 g, 2.86 mmol), KOAc (0.90 g, 9.13 mmol), bis(pinacolato)diboron (0.94 g, 3.17 mmol) and Pd(dppf)Cl_2 (71 mg, 0.10 mmol) were dissolved in 1,4-dioxane (10 mL). The purified product was obtained as a beige solid (0.75 g, 66%). ^{1}H NMR [ppm] (700 MHz, $C_2D_2Cl_4$): 8.14 (H^3, d, $J^3_{H\text{-}H}$=7.7 Hz, 2H), 7.69 (H^2, s, 2H), 7.36 (H^1 ,t, $J^3_{H\text{-}H}$ = 7.7 Hz, 2H), 7.25 (H^2 ,t , $J^3_{H\text{-}H}$ =7.7 Hz, 2H), 6.89 (H^6 ,d , $J^3_{H\text{-}H}$= 8 Hz, 2H), 1.85 (H^{11} , s, 6H), 1.36 (H^{12}, s, 12H). ^{13}C NMR [ppm] (176 MHz, $C_2D_2Cl_4$): 141.5, 138.6, 138.5, 136.5, 127.5, 124.2, 121.9, 120.9, 111.0, 85.5, 26.5, 18.7. APCI calc. for $C_{26}H_{26}BNO_2$ 397.22, found: 398.3.

7.8.3 Formation of triazine-carbazole based compounds by Suzuki-coupling

Under an argon atmosphere the boronic acid pinacol ester (1.0 eq) was placed together with the corresponding triazine (1.1 eq.), K_2CO_3 (3.0 eq.) and $Pd(PPh_3)_4$ (5 mol%) in a flame-dried flask and dissolved in a THF/water (2:1) mixture. The solution was heated to 85 °C over night. After cooling down to room temperature the water phase was extracted with DCM for three times (for 2CzTRZ based materials see detailed description, due to limited solubility). The combined organic phases were washed with brine solution and dried over $MgSO_4$. The product was purified by column chromatography (stationary phase: silica, eluent: hexane/DCM 4:1) in a first step. The product was further purified by sublimation for device fabrication and solid state measurements.

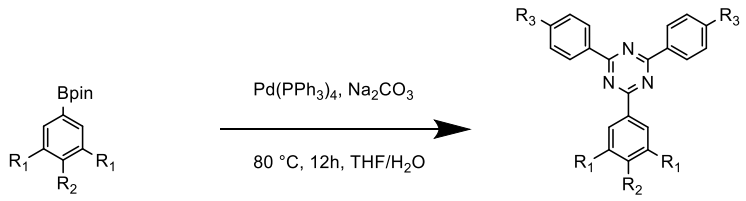

1CzTrz: $R_1 = CH_3$, R_2 = Cz, R_3 = H
2CzTrz: R_1 = Cz, R_2 = H, R_3 = H
3CzTrz: R_1 = Cz, R_2 = Cz, R_3 = H

1CzTrz-F: $R_1 = CH_3$, R_2 = Cz, R_3 = F
2CzTrz-F: R_1 = Cz, R_2 = H, R_3 = F
3CzTrz-F: R_1 = Cz, R_2 = Cz, R_3 = F

9,9',9''-(5-(4,6-diphenyl-1,3,5-triazin-2-yl)benzene-1,2,3-triyl)tris(9*H*-carbazole) (3CzTRZ**)**

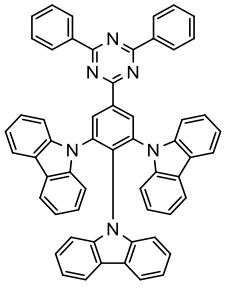

9,9'-(5-(4,4,5,5-tetramethyl-1,3,2-dioxaborolan-2-yl)-1,3-phenylene)bis(9*H*-carbazole) (0.27 g, 1.02 mmol), 2-chloro-4,6-diphenyl-1,3,5-triazine (0.65 g, 0.93 mmol), K_2CO_3 (0.38 g, 2.78 mmol) and $Pd(PPh_3)_4$ (54 mg, 0.05 mmol) were used and dissolved in THF/water (10:5 mL). The purified product was obtained as a pale yellow solid (0.65 g, 94%). ^{1}H NMR [ppm] (700 MHz, $C_2D_2Cl_4$): 9.29 (s, 2H), 8.74 (d, J^3 = 8.4 Hz, 4H), 7.81 (d, J^3 = 8.4 Hz, 4H), 7.61 (t, J^3 = 7.2 Hz, 2H), 7.54 (t, J^3 = 7.3 Hz, 4H), 7.36 (d, J^3 = 8.2 Hz, 2H), 7.32 (d, J^3 = 8.3 Hz, 4H), 7.12-7.05 (m, 8H), 6.99 (d, J^3 = 8.3 Hz, 2H), 6.78 (t, J^3 = 7.2 Hz, 2H), 6.68 (t, J^3 = 7.3 Hz, 2H). ^{13}C NMR [ppm] (176 MHz, $C_2D_2Cl_4$): 172.2, 169.9, 139.9, 138.4, 138.2, 137.7, 135.7, 135.6, 133.2, 130.2, 129.3, 129.0, 125.7, 124.7, 123.7, 123.4, 120.3, 120.0, 119.9, 119.4, 110.3, 110.0. MALDI calc. for $C_{57}H_{36}N_6$ 804.30, found 804.30.

9,9',9''-(5-(4,6-bis(4-fluorophenyl)-1,3,5-triazine-2-yl)benzene-1,2,3-triyl)tris(9*H*-carbazole) (3CzTRZ**-F)**

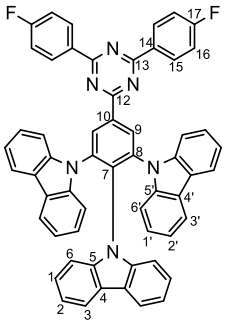

According to the general procedure 9,9'-(5-(4,4,5,5-tetramethyl-1,3,2-dioxaborolan-2-yl)-1,3-phenylene)bis(9*H*-carbazole) (0.65 g, 0.93 mmol), 2-chloro-4,6-bis(4-fluorophenyl)-1,3,5-triazine (0.31 g, 1.02 mmol), K_2CO_3 (0.38 g, 6.39 mmol) and $Pd(PPh_3)_4$ (54 mg, 0.05 mmol) were used and dissolved in THF/water (10:5 mL). The purified product was obtained as a pale yellow solid (0.687 g, 88%). ^{1}H NMR [ppm] (700 MHz, $C_2D_2Cl_4$): 9.23 (H^9, s, 2H), 8.73 (H^{15}, d, J^3 = 8.3 Hz, 4H), 7.81 (H^3, d, J^3 = 8.3 Hz, 4H), 7.35 ($H^{3'}$, d, J^3 = 8.3 Hz, 2H), 7.29 (H^6, d, J^3 = 8.1 Hz, 4H), 7.20 (H^{16}, t, J^3 = 8.2 Hz, 4H), 7.08 (H^2, t, J^3 = 7.2 Hz, 4H), 7.06 (H^1, t, J^3 = 7.3 Hz, 4H), 6.97 ($H^{6'}$, t, J^3 = 8.4 Hz, 2H), 6.77 ($H^{2'}$, 7, J^3 = 7.2 Hz, 2H), 6.66 ($H^{1'}$, t, J^3 = 7.2 Hz, 2H. ^{13}C NMR [ppm] (176 MHz, $C_2D_2Cl_4$): 171.0 (C^{13}), 170.0 (C^{14}), 165.9 (C^{17}), 139.9 (C^5), 138.1 (C^7), 138.0 ($C^{5'}$), 137.7 (C^8), 135.7 (C^{10}), 131.7 (C^{15}), 130.2 (C^9), 125.7 (C^2), 124.9 ($C^{1'}$), 123.7 ($C^{4'}$), 123.4 (C^4), 120.6 ($C^{2'}$), 120.4 (C^1), 119.9 (C^3), 119.3 ($C^{3'}$), 116.0 (C^{16}), 110.2 ($C^{6'}$), 110.0 (C^6). MALDI calc. for $C_{57}H_{34}F_2N_6$ 840.28, found 840.39.

9,9',9''-(5-(4,6-diphenyl-1,3,5-triazin-2-yl)benzene-1,2,3-triyl)tris(9*H*-carbazole) (2CzTRZ**)**

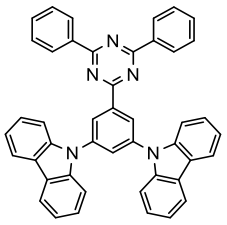

According to the general procedure 9,9'-(5-(4,4,5,5-tetramethyl-1,3,2-dioxaborolan-2-yl)-1,3-phenylene)bis(9*H*-carbazole) (0.70 g, 1.30 mmol), 2-chloro-4,6-diphenyl-1,3,5-triazine (0.39 g, 1.44 mmol), K_2CO_3 (0.54 g, 3.90 mmol) and $Pd(PPh_3)_4$ (75 mg, 0.06 mmol) were used and dissolved in THF/water (10:5 mL). After completion of the reaction and cooling down to room temperature the yellow precipitate was collected by filtration and washed three times with water (20 mL). The product was further washed using methanol (50 mL) and ethylacetate (50 mL) and dried under high vacuum. The purified product was obtained as a yellow solid (0.80 g, 96%). ^{1}H NMR [ppm] (700 MHz,

$C_2D_2Cl_4$): 9.12 (d, J^4 = 1.3 Hz, 2H), 8.75 (d, J^3 = 8.3 Hz, 4H), 8.21 (d, J^3 = 8.2 Hz, 4H), 8.06 (t, J^4 = 1.8 Hz, 1H), 7.66 (t, J^3 = 7.2 Hz, 4H), 7.62 (t, J^3 = 7.3 Hz, 2H), 7.56 (t, J^3 = 7.3 Hz, 4H), 7.51 (t, J^3 = 7.3 Hz, 4H), 7.38 (t, J^3 = 7.2 Hz, 4H). ^{13}C NMR [ppm] (176 MHz, $C_2D_2Cl_4$): 172.4, 170.6, 141.0, 140.6, 140.1, 136.0, 132.9, 129.4, 128.9, 128.8, 126.6, 126.3, 123.9, 120.8, 120.5, 109.9. MALDI calc. for $C_{45}H_{29}N_5$ 649.24, found 649.27.

9,9'-(5-(4,6-bis(4-fluorophenyl)-1,3,5-triazin-2-yl)-1,3-phenylene)bis(9*H*-carbazole) (2CzTRZ**-F)**

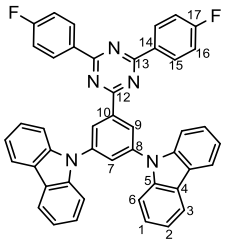

According to the general procedure 9,9'-(5-(4,4,5,5-tetramethyl-1,3,2-dioxaborolan-2-yl)-1,3-phenylene)bis(9*H*-carbazole) (1.51 g, 2.83 mmol), 2-chloro-4,6-bis(4-fluorophenyl)-1,3,5-triazine (0.94 g, 3.11 mmol), K_2CO_3 (1.17 g, 8.49 mmol) and $Pd(PPh_3)_4$ (164 mg, 0.14 mmol) were used and dissolved in THF/water (20:10 mL). After completion of the reaction and cooling down to room temperature the yellow precipitate was collected by filtration and washed three times with water (40 mL). The product was further washed using methanol (100 mL) and ethylacetate (100 mL) and dried under high vacuum. The purified product was obtained as a yellow solid (1.88 g, 98%). ^{1}H NMR [ppm] (700 MHz, $C_2D_2Cl_4$): 9.07 (H^9, d, J^4 = 1.3 Hz, 2H), 8.75 (H^{15}, d, J^3 = 8.3 Hz, 4H), 8.21 (H^3, d, J^3 = 8.3 Hz, 4H), 8.06 (H^7, t, J^4 = 1.8 Hz, 1H), 7.64 (H^6, t, J^3 = 8.2 Hz, 4H), 7.51 (H^1, t, J^3 = 7.3 Hz, 4H), 7.38 (H^2, t, J^3 = 7.3 Hz, 4H), 7.24 (H^{16}, d, J^3 = 8.2 Hz, 4H)**.** ^{13}C NMR [ppm] (176 MHz, $C_2D_2Cl_4$): 171.6 (C^{13}), 170.6 (C^{12}), 165.7 (C^{17}) , 140.9 (C^5), 140.5 (C^8), 140.2 (C^{10}), 132.1 (C^{14}), 131.6 (C^{15}), 129.2 (C^7), 126.7 (C^1), 126.4 (C^9) , 123.8 (C^4), 120.7 (C^2) , 120.4 (C^3) , 115.9 (C^{16}), 109.7 (C^6). MALDI calc. for $C_{45}H_{27}F_2N_5$ 675.22, found 675.42.

9-(4-(4,6-diphenyl-1,3,5-triazin-2-yl)-2,6-dimethylphenyl)-9*H*-carbazole (1CzTRZ**)**

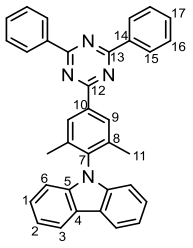

According to the general procedure 9-(2,6-dimethyl-4-(4,4,5,5-tetramethyl-1,3,2-dioxaborolan-2-yl)phenyl)-9*H*-carbazole (0.63 g, 1.59 mmol), 2-chloro-4,6-diphenyl-1,3,5-triazine (0.47 g, 1.75 mmol), K_2CO_3 (0.66 g, 4.78 mmol) and $Pd(PPh_3)_4$ (92 mg, 0.08 mmol) were used and dissolved in THF/water (10:5 mL). The purified product was obtained as a white solid (0.57 g, 71%). ^{1}H NMR [ppm] (700 MHz, $C_2D_2Cl_4$): 8.81 (d, J^3 = 8.5 Hz, 4H), 8.67 (s, 2H), 8.20 (d, J^3 = 8.3 Hz, 2H), 7.67 (t, J^3 = 7.2 Hz, 2H), 7.63 (t, J^3 = 7.4 Hz, 4H), 7.43 (t, J^3 = 7.3 Hz, 2H), 7.31 (t, J^3 = 7.2 Hz, 2H), 7.02 (d, J^3 = 8.2 Hz, 2H) 2.05 (s, 6H). ^{13}C NMR [ppm] (176 MHz, $C_2D_2Cl_4$): 171.8, 171.4, 140.1, 138.8, 138.7, 136.3, 136.1, 133.0, 129.4, 129.2, 128.9, 126.4, 123.1, 120.7, 119.8, 109.7, 18. MALDI calc. for $C_{35}H_{26}N_4$ 502.22, found 502.24.

9-(4-(4,6-bis(4-fluorophenyl)-1,3,5-triazin-2-yl)-2,6-dimethylphenyl)-9*H*-carbazole (1CzTRZ**-F)**

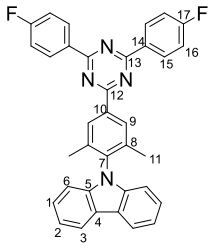

According to the general procedure 9-(2,6-dimethyl-4-(4,4,5,5-tetramethyl-1,3,2-dioxaborolan-2-yl)phenyl)-9*H*-carbazole (0.58 g, 1.46 mmol), 2-chloro-4,6-bis(4-fluorophenyl)-1,3,5-triazine (0.49 g, 1.61 mmol), K_2CO_3 (0.61 g, 4.38 mmol) and $Pd(PPh_3)_4$ (84 mg, 0.07 mmol) were used and dissolved in THF/water (10:5 mL). The purified product was obtained as a white solid (0.55 g, 70%). ^{1}H NMR [ppm] (700 MHz, $C_2D_2Cl_4$): 8.81 (H^{15}, t, $J^3_{H\text{-}H}$=6.8 Hz, 4H), 8.62 (H^9, s, 2H), 8.19 (H^3, d, $J^3_{H\text{-}H}$=7.7 Hz, 2H), 7.42 (H^1 ,t, $J^3_{H\text{-}H}$ = 7.8 Hz, 2H), 7.31 (H^{16} , t, $J^3_{H\text{-}H}$=7.1 Hz, 4H), 7.29 (H^2, t, $J^3_{H\text{-}H}$=8.3 Hz, 2H), 6.99 (H^6 ,d, $J^3_{H\text{-}H}$=8.1 Hz, 2H), 2.03 (H^{11}, s, 6H). ^{13}C NMR [ppm] (176 MHz, $C_2D_2Cl_4$): 171.4 (C^{12}, s, 1C), 170.8 (C^{13}, s, 2C), 165.9 (C^{17}, d, $J^1_{C\text{-}F}$=251.7 Hz, 2C), 140.2 (C^5, s, 2C), 138.9 (C^8, s, 2C), 138.8 (C^7, s, 1C), 136.2 (C^{10}, s, 1C), 132.1 (C^{14}, d, $J^4_{C\text{-}F}$ = 3 Hz, 2C), 131.7 (C^{15}, d, $J^3_{C\text{-}F}$=8.1 Hz, 4C), 129.1 (C^9, s, 2C),

126.4 (C^1, s, 2C), 123.1 (C^4, s, 2C), 120.7 (C^3, s, 2C), 119.8 (C^2, s, 2C), 115.9 (C^{16}, d, J=21.2 Hz, 4C), 109.5 (C^6, s, 2C), 18.1 (C^{11}, s, 2C). MALDI calc. for $C_{35}H_{24}F_2N_4$ 530.20, found 538.20.

7.8.4 Formation of triazine containing fluorobenzenes

Benzamidine hydrochloride (2.0 eq), copper acetate (1.0 eq), sodium carbonate (2.0 eq) and the corresponding fluorobenzaldehyde (1.0 eq.) were placed together in an open flask and suspended in toluene. The suspension was heated at 100 °C over night. The reaction mixture was cautiously treated with 2M-HCl solution until all residues were dissolved. The water phase was extracted with DCM for three times. The combined organic phases were washed with NH_4Cl solution, brine solution and dried over $MgSO_4$. The product was purified by column chromatography (stationary phase: silica, eluent: hexane/DCM).

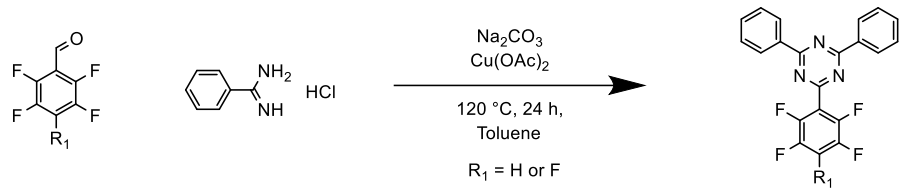

2,4-diphenyl-6-(2,3,5,6-tetrafluorophenyl)-1,3,5-triazine

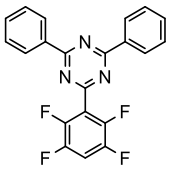

According to the general procedure 2,3,5,6-tetrafluorobenzaldehyde (1.00 g, 5.6 mmol), benzamidine hydrochloride (1.76 g, 11.20 mmol), sodium carbonate (1.19 g, 11.20 mmol) and copper acetate (1.10 g, 5.6 mmol) were suspended in toluene (40 mL). The purified product was obtained as a light grey solid (0.77 g, 36%). ^{1}H NMR (700 MHz, $C_2D_2Cl_4$) [ppm]: 8.68 (d, J^3 = 7.8 Hz, 4H), 7.64 (t, J^3 = 7.1 Hz, 2H), 7.58 (t, J^3 = 7.1 Hz, 4H), 7.30 (tt, $J^3_{H\text{-}F}$ = 6.9, J^4 = 9.1 Hz, 1H). ^{13}C NMR (176 MHz, $C_2D_2Cl_4$) [ppm]: 172.4, 167.1, 146.9, 145.8, 145.5, 144.3, 135.2, 133.5, 129.1, 118.7, 107.9. ^{19}F NMR (658 MHz, $C_2D_2Cl_4$): -137.6, -141.5. APCI calc. for $C_{21}H_{11}F_4N_3$ 381.09, found: 382.20.

2-(perfluorophenyl)-4,6-diphenyl-1,3,5-triazine

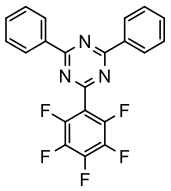

According to the general procedure 2,3,4,5,6-pentafluorobenzaldehyde (1.00 g, 5.07 mmol), benzamidine hydrochloride (1.59 g, 10.15 mmol), sodium carbonate (1.08 g, 10.15 mmol) and copper acetate (1.00 g, 5.07 mmol) were suspended in toluene (40 mL). The purified product was obtained as a light grey solid (0.73 g, 36%). ^{1}H NMR [ppm] (700 MHz, $C_2D_2Cl_4$): 8.67 (d, J^3 = 7.6 Hz, 4H), 7.65 (t, J^3 = 7.3 Hz, 2H), 7.58 (t, J^3 = 7.3 Hz, 4H). ^{13}C NMR [ppm] (176 MHz, $C_2D_2Cl_4$): 171.9, 166.3, 146.5, 145.0, 143.3, 141.7, 138.8, 137.2, 135.1, 133.5, 131.8, 130.0, 113.6. ^{19}F NMR [ppm] (658 MHz, $C_2D_2Cl_4$): -140.5, -150.5, -160.6. APCI calc. for $C_{21}H_{10}F_5N_3$ 399.08, found 400.20.

7.8.5 Introduction of carbazole in triazine containing fluorobenzenes

A similar procedure to the previously mentioned general procedure for introduction of carbazole was performed with higher amount of Cs_2CO_3. A mixture of carbazole (5 Cz: 5 eq., 4 Cz: 4 eq.) and Cs_2CO_3 (5 Cz: 20 eq., 4 Cz: 16 eq.) was placed in a two necked flame-dried flask under an argon atmosphere, suspended in DMF and stirred at room temperature for 30 min, followed by addition of corresponding fluorobenzene (5 Cz: 1 eq., 4 Cz: 1 eq.) and heating to 175 °C for 24 h. After cooling to room temperature, the reaction mixture was poured on water and the water phase was extracted three times with dichloromethane (DCM). The combined organic phases were washed with brine solution and dried over $MgSO_4$. The solvent was evaporated under reduced pressure and the crude product was purified by column chromatography (stationary phase: silica, eluent: hexane/DCM 3:2).

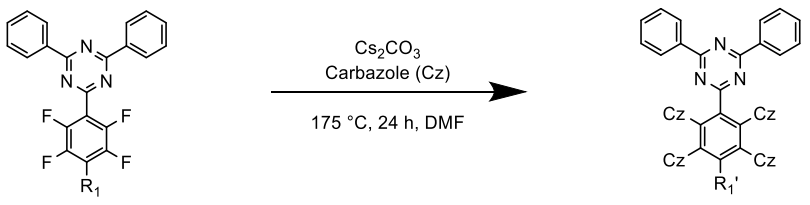

9,9',9'',9'''-(3-(4,6-diphenyl-1,3,5-triazin-2-yl)benzene-1,2,4,5-tetrayl)tetrakis(9*H*-carbazole) (4CzTRZ**)**

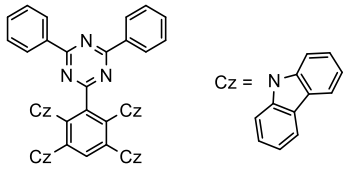

According to the general procedure 2,4-diphenyl-6-(2,3,5,6-tetrafluorophenyl)-1,3,5-triazine (0.20 g, 0.52 mmol), carbazole (0.36 g, 2.1 mmol) and Cs_2CO_3 (2.73 g, 8.4 mmol) were suspended in DMF (10 mL). The purified product was obtained as a yellow solid (0.50 g, 98%). ^{1}H NMR [ppm] (700 MHz, $C_2D_2Cl_4$): 8.38 (s, 1H), 7.85 (d, J^3 = 8.4 Hz, 3H), 7.52-7.44 (m, 6H), 7.35 (d, J^3 = 8.4 Hz, 3H), 7.30 (t, J^3 = 7.3 Hz, 2H), 7.27 (d, J^3 = 8.4 Hz, 3H), 7.17 (t, J^3 = 7.2 Hz, 3H), 7.12 (t, J^3 = 7.3 Hz, 3H), 7.07 (t, J^3 = 7.3 Hz, 3H), 7.02 (t, J^3 = 7.2 Hz, 3H), 6.92 (t, J^3 = 7.2 Hz, 2H). ^{13}C NMR [ppm] (176 MHz, $C_2D_2Cl_4$): 170.7, 170.0, 141.6, 140.7, 140.6, 138.6, 135.8, 134.9, 133.1, 131.8, 128.5, 127.9, 125.9, 125.3, 123.9, 123.8, 120.6, 120.1, 120.0, 119.8, 110.4, 110.1. MALDI calc for $C_{69}H_{43}N_7$ 969.36, found 969.40.

9,9',9'',9''',9''''-(6-(4,6-diphenyl-1,3,5-triazin-2-yl)benzene-1,2,3,4,5-pentayl)pentakis(9*H*-carbazole) (5CzTRZ**)**

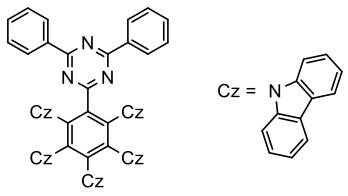

According to the general procedure 2-(perfluorophenyl)-4,6-diphenyl-1,3,5-triazine (0.20 g, 0.52 mmol), carbazole (0.42 g, 2.5 mmol) and Cs_2CO_3 (3.25 g, 10.0 mmol) were suspended in DMF (10 mL). The purified product was obtained as a yellow solid (0.33 g, 55%). ^{1}H NMR [ppm] (700 MHz, $C_2D_2Cl_4$): 7.42 (d, J^3 = 8.0 Hz, 4H), 7.40-7.35 (m, 8H), 7.33-7.10 (m, 12H), 7.05 (t, J^3 = 7.0 Hz, 6H), 6.95 (t, J^3 = 7.0 Hz, 6H), 6.89 (t, J^3 = 7.0 Hz, 6H), 6.84-6.70 (m, 6H), 6.67 (t, J^3 = 7.0 Hz, 2H). ^{13}C NMR [ppm] (176 MHz, $C_2D_2Cl_4$): 170.9, 140.7, 139.3, 138.6, 137.9, 137.7, 134.9, 131.8, 128.4, 127.9, 125.0, 124.5, 124.3, 123.8, 120.1, 120.0, 119.9, 119.7, 119.3, 119.2. MALDI calc for $C_{81}H_{50}N_8$ 1134.42, found 1134.48.

7.8.6 Preperation of SpiroAc-TRZ

10-(4-(4,6-diphenyl-1,3,5-triazin-2-yl)phenyl)-10*H*-spiro[acridine-9,9'-fluorene] (SpiroAc-TRZ)

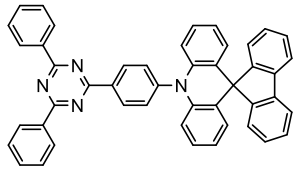

Under a nitrogen atmosphere 2-(4-bromophenyl)-4,6-diphenyl-1,3,5-triazine (388 mg, 1 eq., 1.0 mmol,) was placed together with 10*H*-Spiro[acridine-9,9'-fluorene] (365 mg, 1.1 eq., 1.1 mmol) and palladium acetate (7 mg, 0.03 eq., 0.03 mmol) and dissolved in toluene (40 mL). After addition of tri-*tert*-butylphosphine (14 µL, 0.06 eq., 0.06 mmol) the reaction mixture was refluxed over night at 110 °C. After cooling to room temperature, the reaction mixture was poured on water and the water phase was extracted three times with dichloromethane (3 x 30 mL). The combined organic phases were washed with brine solution and dried over $MgSO_4$. The solvent was evaporated under reduced pressure and the crude product was purified by column chromatography (stationary phase: silica, eluent: hexane/DCM 3:2) to yield a light yellow solid (56%). ^{1}H NMR [ppm] (400 MHz, CD_2Cl_2): 9.06 (d, J = 8.3 Hz, 2H), 8.78 (d, J = 8.8 Hz, 4H), 7.78 (d, J = 7.8 Hz, 2H), 7.68 (d, J = 7.7 Hz, 2H), 7.65 – 7.52 (m, 6H), 7.41 – 7.31 (m, 4H), 7.23 (t, J = 7.4 Hz, 2H), 6.88 (t, J = 7.8 Hz, 2H), 6.51 (t, J = 7.7 Hz, 2H), 6.41 (d, J = 8.3, 2H), 6.32 (d, J = 7.7 Hz, 2H).

Appendix Chapter 2

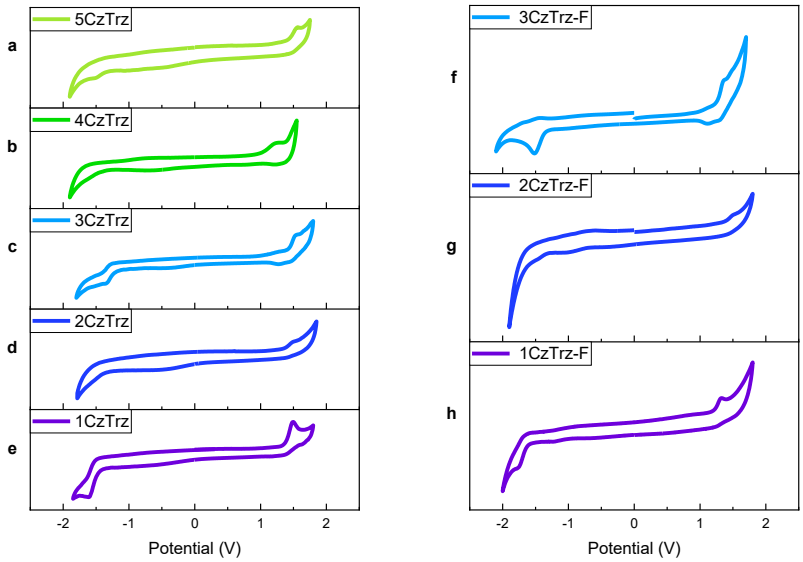

Figure A2.1. Cyclic voltammetry results of 1-5CzTRZ and 1-3CzTRZ-F. The oxidation potential of Fc/Fc^{+} against Ag/AgCl was recorded in acetonitrile-$BuNPF_6$ solution (0.05 M) as 0.34 V. $E = -\left(E_{onset} - E_{\frac{Fc}{Fc^{+}}} + 4.8\right)$ eV.

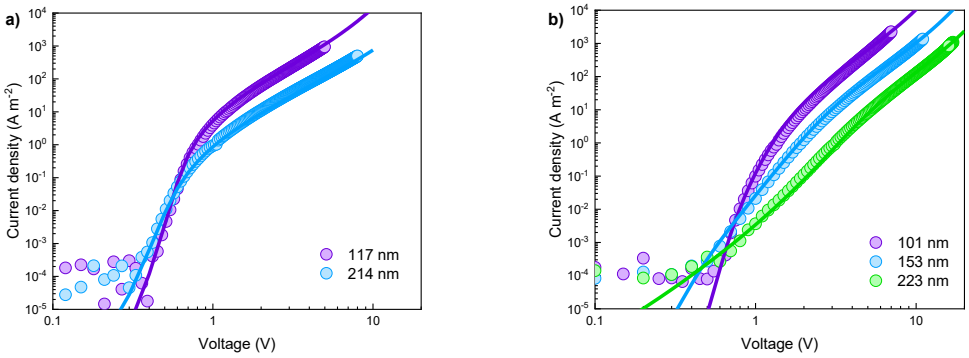

Figure A2.2. Electron transport of 3CzTRZ and 2CzTRZ with varying thickness. Current density-voltage characteristics of 3CzTRZ (a) and 2CzTRZ (b) electron-only devices with varying thickness of the semiconductor layer. Symbols are experimental data and solid lines are fits with a numerical drift-diffusion model. Obtained trap densities N_t, trap depths E_t, width of the Gaussian trap distributions σ_t, lattice constants a, DOS variances σ and mobilities μ for electrons are given in the **Table A2.4**.

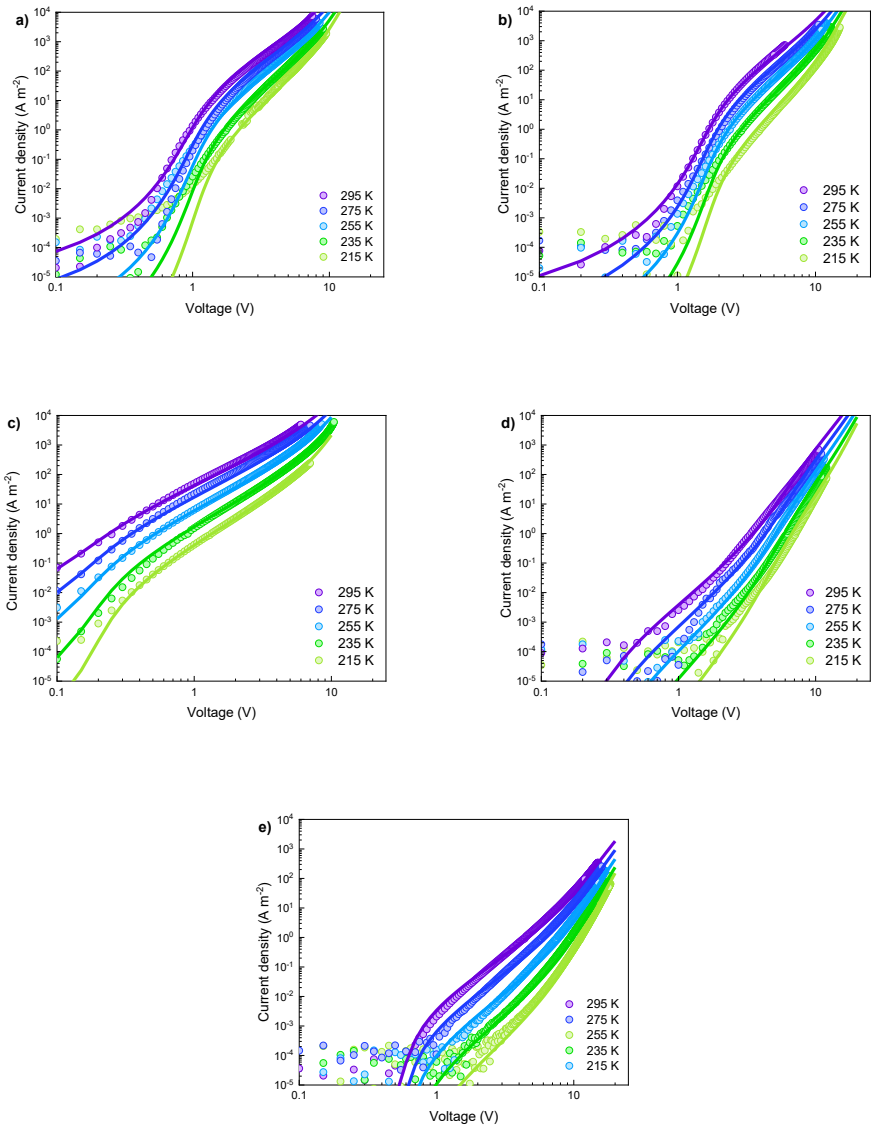

Figure A2.3. Temperature dependent electron transport of 1-5CzTRZ**.** Current density-voltage characteristics of 1CzTRZ (94 nm) (a), 2CzTRZ (100nm) (b), 3CzTRZ (98 nm) (c), 4CzTRZ (79nm) (d) and 5CzTRZ (102 nm) (e) electron-only devices as function of temperature. Symbols are experimental data and solid lines are fits with a numerical drift-diffusion model. The model parameters are given in **Table A2.1**.

Table A2.1. Drift-diffusion modeling parameters for electron-only devices of 1-5CzTRZ.

	1CzTRZ	2CzTRZ	3CzTRZ	4CzTRZ	5CzTRZ
Trap density, N_t gauss ($\times 10^{22}$ m^{-3})	6.0	8.0	0.24	60	280
Trap depth, E_t (eV)	0.78	0.77	0.70	0.56	0.47
Width of Gaussian trap distribution, σ_t (eV)	0.10	0.10	0.10	0.10	0.08
Lattice constant EGDM, a ($\times 10^{-9}$ m)	1.6	1.4	1.5	0.95	1.0
DOS variance EGDM, σ (eV)	0.11	0.12	0.11	0.12	0.11
Mobility at 295 K, μ ($\times 10^{-10}$ m^2/Vs)	5.19	1.16	5.19	1.16	5.19

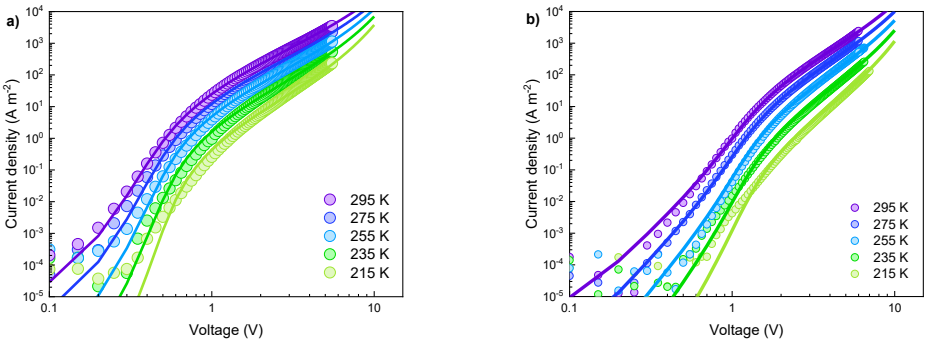

Figure A2.4 | Temperature dependent electron transport of 3CzTRZ-F and 2CzTRZ-F. Current density-voltage characteristics of 3CzTRZ-F (118 nm) (a) and 2CzTRZ-F (91 nm) (b) electron-only devices as function of temperature. Symbols are experimental data and solid lines are fits with a numerical drift-diffusion model. The model parameters are given in **Table A2.2**.

Table A2.2. Drift-diffusion modeling parameters for electron-only devices of 1-3CzTRZ-F.

	1CzTRZ-F	2CzTRZ-F	3CzTRZ-F
Trap density, N_t gauss ($\times 10^{22}$ m^{-3})	100	6.0	0.9
Trap depth, E_t (eV)	0.48	0.63	0.70
Width of Gaussian trap distribution, σ_t (eV)	0.10	0.10	0.10
Lattice constant EGDM, a ($\times 10^{-9}$ m)	1.60	1.40	1.80
DOS variance EGDM, σ (eV)	0.10	0.11	0.09
Mobility at 295 K, μ ($\times 10^{-10}$ m^2/Vs)	8.12	4.15	27.92

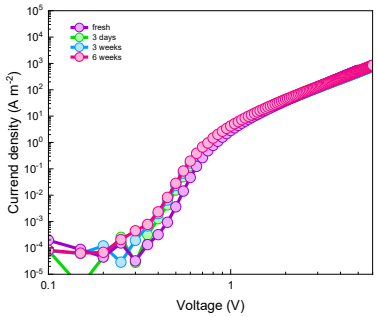

Figure A2.5 | Aging of electron-only devices of 3CzTRZ. Current density-voltage characteristics of 3CzTRZ (155 nm) electron-only devices kept under inert atmosphere and scanned after different aging time (fresh, 3 days, 3 weeks, 6 weeks). No apparent degradation can be observed over aging time.

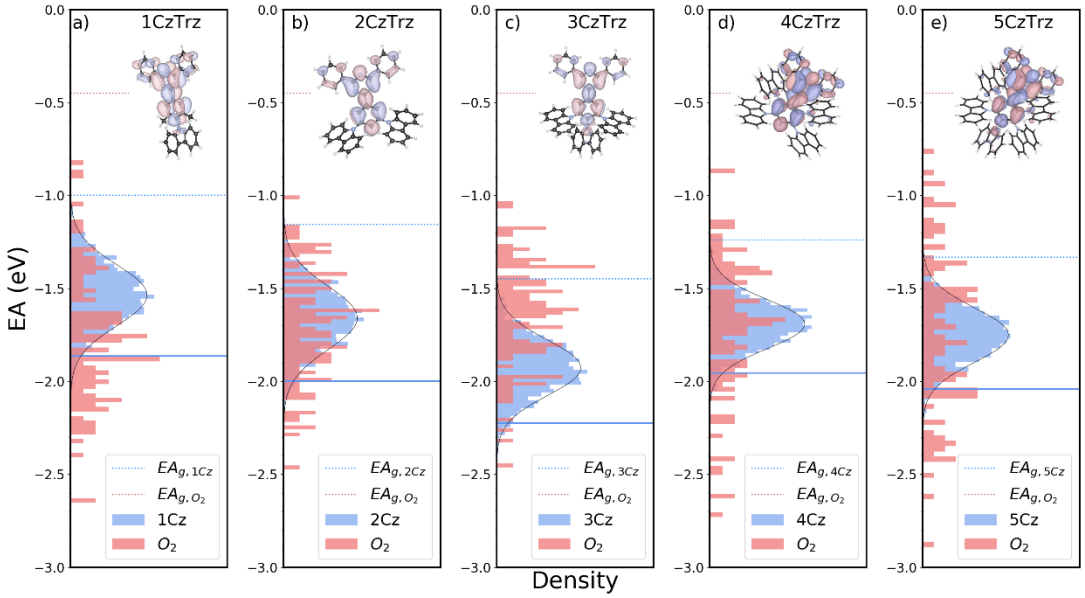

Figure A2.6. Calculated density-of-states distributions for amorphous 1-5CzTRZ. The density of states of electron affinity of molecular oxygen (red) and organic materials (blue; 1CzTRZ, 2CzTRZ, 3CzTRZ, 4CzTRZ, and 5CzTRZ) with amorphous morphology. The dotted lines are the gas-phases electron affinity for molecular oxygen and organic materials. The blue solid line represents the energy μ_e -2σ_e, with μ_e corresponding to the average of the calculated solid-state EA values and σ_e the standard deviation of the Gaussian distribution, respectively (Table A2.3). The energy μ_e -2σ_e is expected to correspond to the onset of the solid-state EA from UPS measurements. It is noted that in the representation of the DOS distributions the conventional sign convention for energy band diagrams is used, meaning negative numbers on the energy axis. In this graphical presentation, higher EAs are represented by more negative numbers, implying that electron traps are located below the molecular

DOS at more negative energies. Apart from the presentation in the figures, EA and IE are positive numbers representing the absolute value of the energy with regard to vacuum (zero energy).

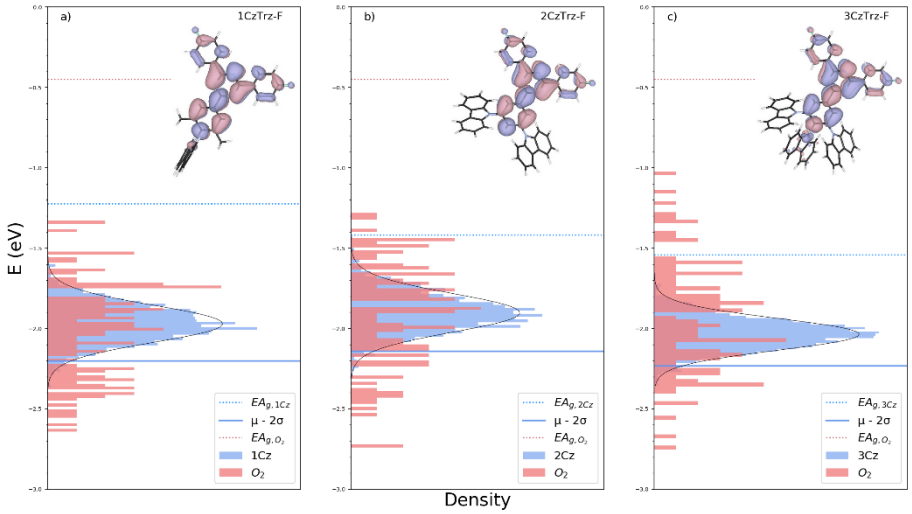

Figure A2.7. Calculated density-of-states distributions for amorphous 1-3CzTrz-F. The density of states of electron affinity of molecular oxygen (red) and organic materials (blue; 1CzTrz-F, 2CzTrz-F and 3CzTrz-F) with amorphous morphology. The dotted lines are the gas-phases electron affinity for molecular oxygen and organic materials. The blue solid line represents the energy μ_e -2σ_e, with μ_e corresponding to the average of the calculated solid-state EA values and σ_e the standard deviation of the Gaussian distribution, respectively (Table A2.5), The energy μ_e -2σ_e is expected to correspond to the onset of the solid-state EA from UPS measurements.

Table A2.3. Material properties in amorphous phase of 1-5CzTrz.

	1CzTRZ-F	**2CzTRZ-F**	**3CzTRZ-F**	**4CzTRZ**	**5CzTRZ**
μ_e (eV)	-1.971	-1.903	-2.036	-1.692	-1.751
σ_e (eV)	0.115	0.119	0.098	0.132	0.146
EA (eV)	-2.201	-2.131	-2.233	-1.955	-2.042
μ_h (eV)	-5.879	-6.085	-5.900	-5.749	-5.735
σ_h (eV)	0.210	0.113	0.139	0.149	0.162
IE (eV)	-5.459	-5.858	-5.622	-5.450	-5.411

Table A2.4. Oxygen trap levels in amorphous 1-5CzTRZ.

	1CzTRZ-F	**2CzTRZ-F**	**3CzTRZ-F**	**4CzTRZ**	**5CzTRZ**
μ_e (eV)	-2.014	-1.916	-1.942	-1.706	-1.745
σ_e (eV)	0.294	0.315	0.340	0.365	0.431
EA (eV)	-2.602	-2.546	-2.622	-2.436	-2.607

Table A2.5. Material properties in amorphous phase of 1-3CzTRZ-F.

	1CzTRZ-F	**2CzTRZ-F**	**3CzTRZ-F**
μ_e (eV)	-1.971	-1.903	-2.036
σ_e (eV)	0.115	0.119	0.098
EA (eV)	-2.201	-2.131	-2.233
μ_h (eV)	-5.879	-6.085	-5.900
σ_h (eV)	0.210	0.113	0.139
IE (eV)	-5.459	-5.858	-5.622

Table A2.6. Oxygen trap levels in amorphous 1-3CzTRZ-F.

	1CzTRZ-F	**2CzTRZ-F**	**3CzTRZ-F**
μ_e (eV)	-2.014	-1.916	-1.942
σ_e (eV)	0.294	0.315	0.340
EA (eV)	-2.602	-2.546	-2.622

Table A2.7. Crystallographic results of single crystal XRD. Crystallographic parameters for the compounds 1CzTRZ, 1CzTRZ-F and 3CzTRZ-F.

	1CzTRZ	**1CzTRZ-F**	**3CzTRZ-F**
Space Group	P $2_1/c$	P $2_1/c$	P $\bar{1}$
Cell Lengths	**a** 24.701(3)	**a** 25.2325(7)	**a** 13.7364(4)
	b 11.8995(8)	**b** 12.3048(3)	**b** 16.4858(6)
	c 8.8160(9)	**c** 8.5631(2)	**c** 21.1482(7)
Cell Angles	**α** 90	**α** 90	**α** 80.448(3)
	β 92.100(8)	**β** 93.375(2)	**β** 78.790(2)
	γ 90	**γ** 90	**γ** 70.435(3)
Cell Volume	2589.55	2654.07	4400.09

Solid-state NMR data

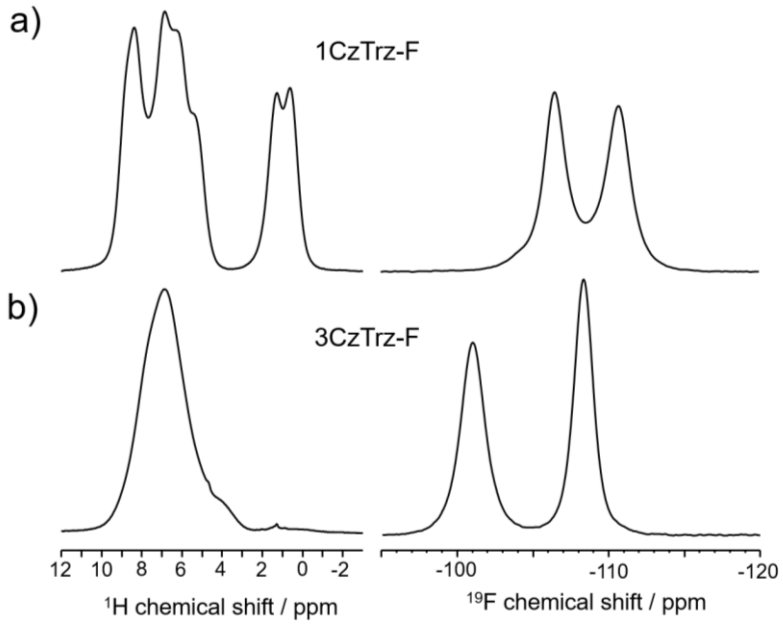

Figure A2.8. NMR spectra of the 1CzTRZ-F and 3CzTRZ-F compounds. a,b, ^{1}H and ^{19}F MAS spectra recorded at 50 kHz spinning speed of vapor deposited material of the compounds **1CzTRZ-F** (a) and **3CzTRZ-F** (b).

Appendix Chapter 3

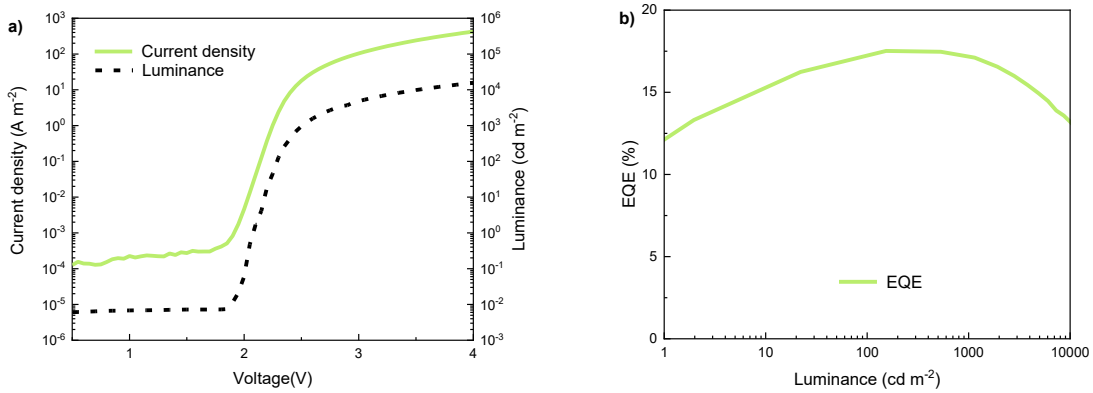

Figure A3.1. Device performance of a single-layer CzDBA OLED. a) Current density-voltage and luminance-voltage characteristics of a single-layer CzDBA OLED using a PEDOT:PSS:PFI anode, with an emissive-layer thickness of 74 nm. b) EQE against luminance.

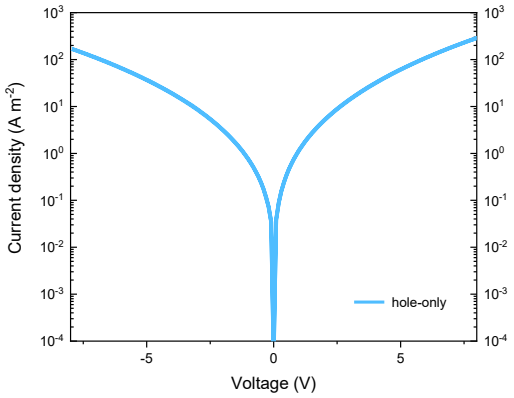

Figure A3.2. Current density-voltage characteristics of a PEDOT:PSS:PFI/SpiroAc-TRZ:mCPCN (1:1; 105 nm)/C_{60}/MoO_3/Al hole only device. Negative bias corresponds to ohmic hole injection from the top contact comprising C_{60}/MoO_3 as the injection structure. Positive bias corresponds to hole injection from the bottom PEDOT:PSS:PFI layer. The symmetric characteristics demonstrate that PEDOT:PSS:PFI is an ohmic hole contact in this system.

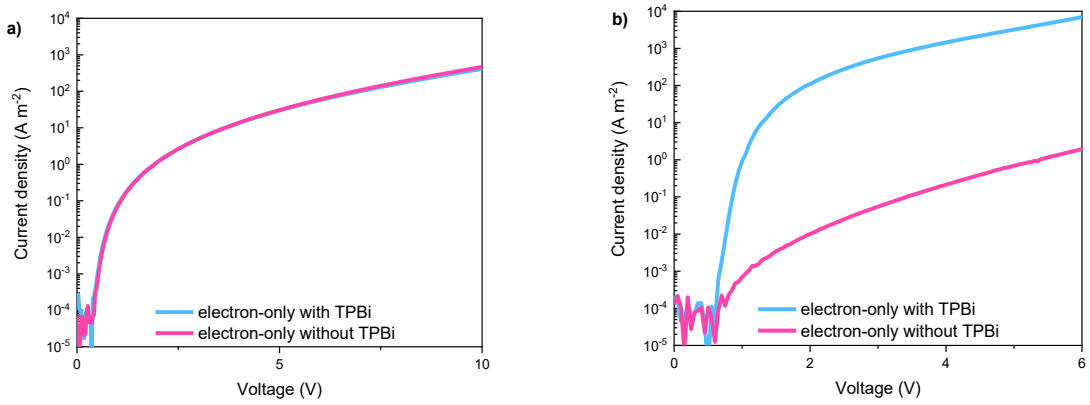

Figure A3.3. a) Current density-voltage characteristics of an Al/SpiroAc-TRZ:mCPCN (1:1; 106 nm)/[TPBi (4 nm)]/Ba (5 nm)/Al electron-only device with and without TPBi (4 nm) interlayer between the active layer and the Ba/Al electrode, showing identical electron currents. b) Current density-voltage characteristics of an Al/SpiroAc-TRZ (95 nm)/[TPBi (4 nm)]/Ba (5 nm)/Al electron-only device with and without TPBi (4 nm) interlayer. Without a host matrix, electron injection without tunneling TPBi interlayer is heavily compromised.

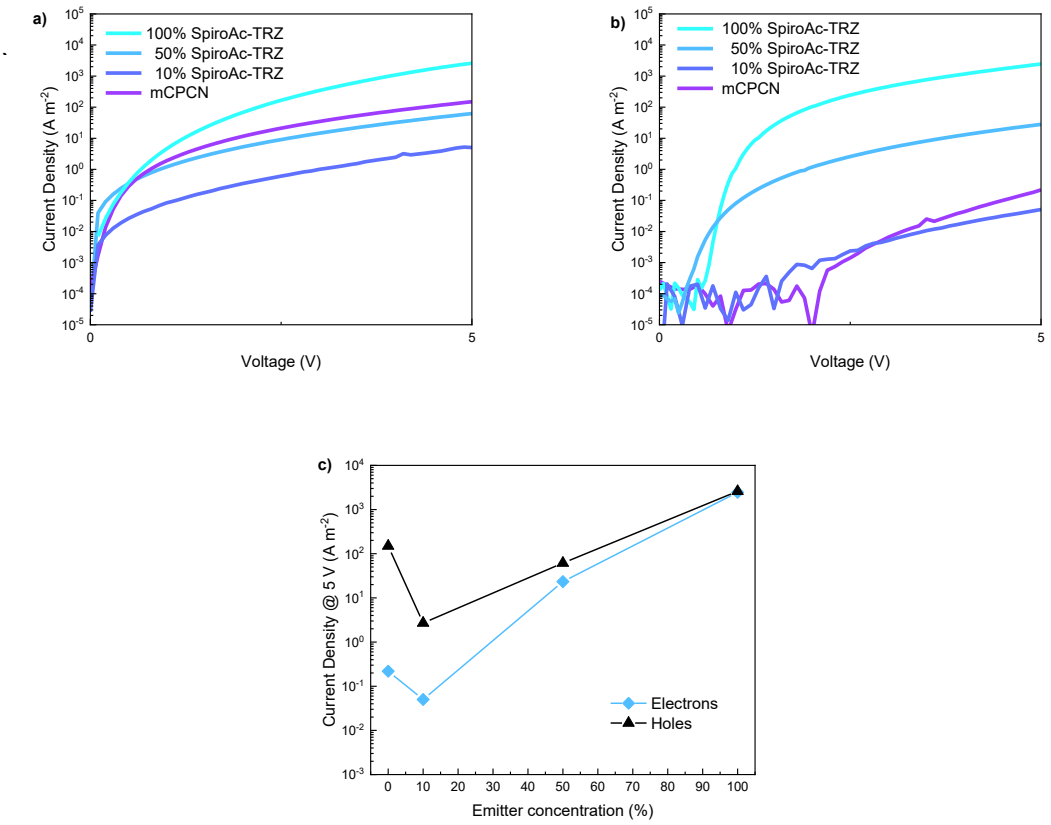

Figure A3.4. a) Current density-voltage characteristics of hole-only devices and electron-only devices (b) with different emitter concentrations. c) Current density at 5 V vs emitter concentration. Electron and hole transport is balanced in the neat emitter. Because the HOMO and LUMO of the emitter are within the gap of the mCPCN host, charge transport occurs via the guest at emitter concentrations above the percolation threshold and is therefore balanced. At 10% emitter concentration, guest-guest transport is less efficient, leading to (partial) transport via the host with additional guest trapping. In the neat host, guest trapping is absent, leading to higher hole and electron currents, which are imbalanced in mCPCN.

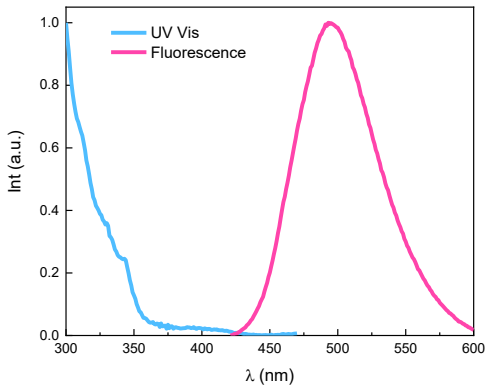

Figure A3.5. UV-Vis absorption and photoluminescence spectra of a co-evaporated SpiroAc-TRZ:mCPCN (1:1) film.

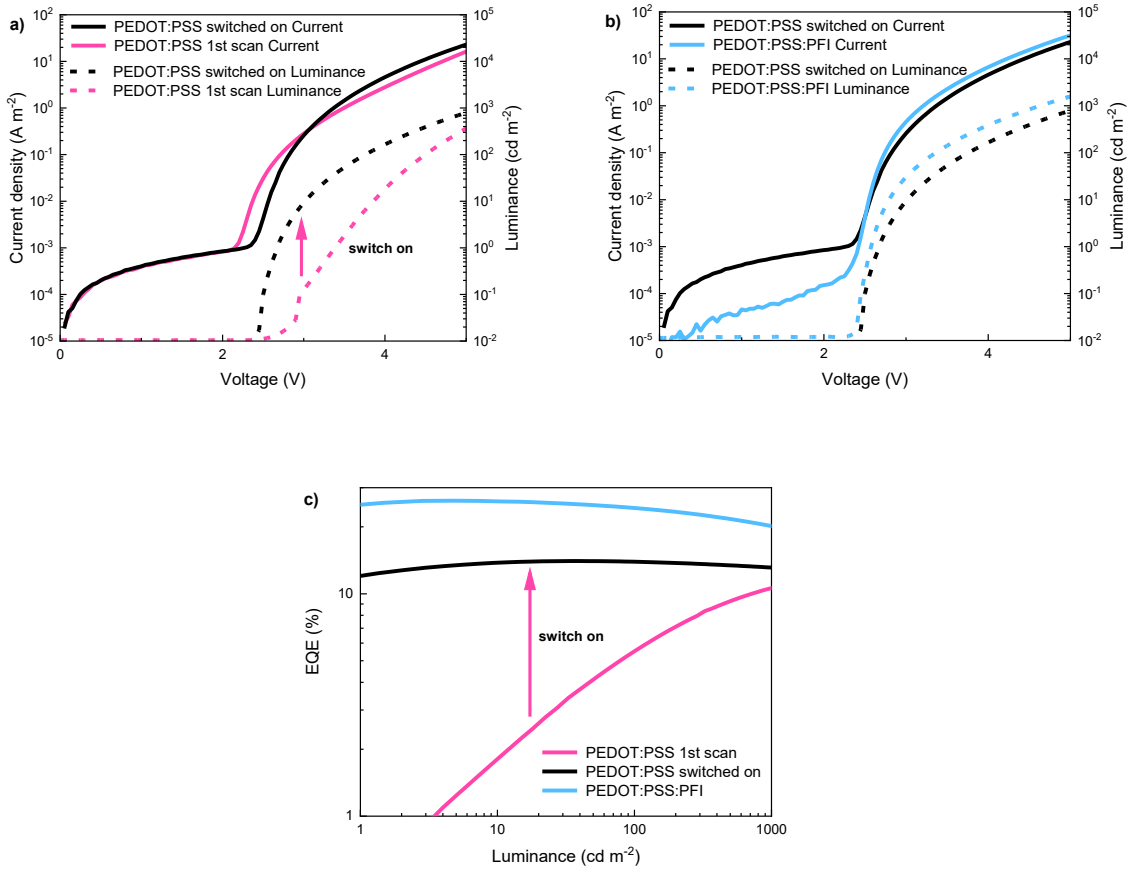

Figure A3.6. a) *J-V-L* characteristics of a SpiroAc-TRZ:mCPCN OLED with a PEDOT:PSS anode without PFI. On the first voltage scan the luminance is low due to the high hole-injection barrier, which can also be seen from the lower built-in voltage in the *J-V* characteristics. Multiple scanning results in a switch-on effect, presumably as a result of electrons at the PEDOT:PSS interface, decreasing the injection barrier. Both the luminance and the built-in voltage increase. However, the current density and luminance are both lower compared to a device with A PEDOT:PSS:PFI anode (b), arising from the hole-injection barrier. This is also reflected in the EQE (c), which is reaches a maximum of about 14% for the PEDOT:PSS-based device.

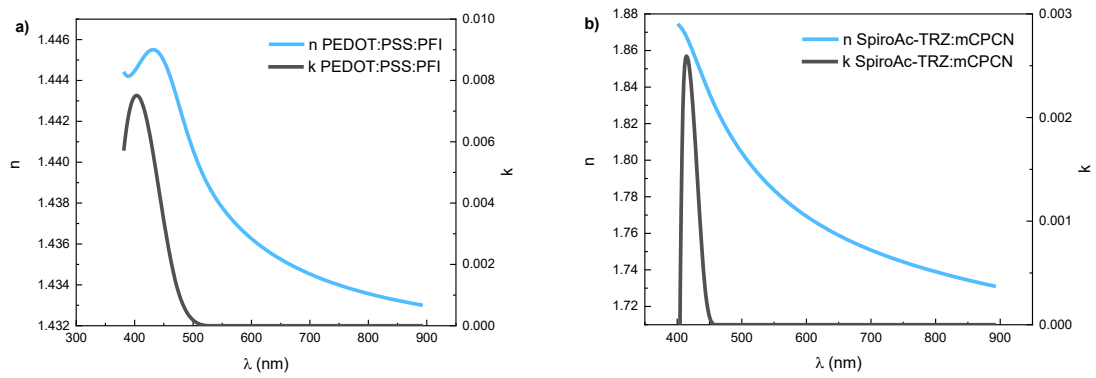

Figure A3.7. a) Refractive index *n* and extinction coefficient *k* of a PEDOT:PSS:PFI film (22 nm) determined by ellipsometry. b) Refractive index *n* and extinction coefficient *k* of a co-evaporated SpiroAc-TRZ:mCPCN (1:1) film (38 nm).

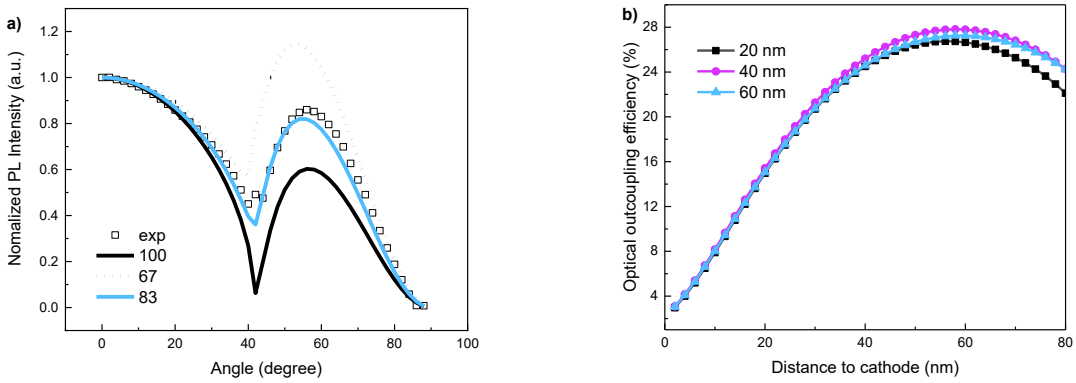

Figure A3.8. a) Angular PL measurements on a co-evaporated SpiroAc-TRZ:mCPCN (1:1) film, including fits to determine the horizontal emitting dipole ratio of 83%. b) Simulated optical outcoupling efficiency as function of the emission position of SpiroAc-TRZ:mCPCN to air with 80 nm thickness and varied PEDOT:PSS:PFI thickness. The maximum achievable outcoupling efficiency remains below 28%, even for an optimal position of the emitting plane.

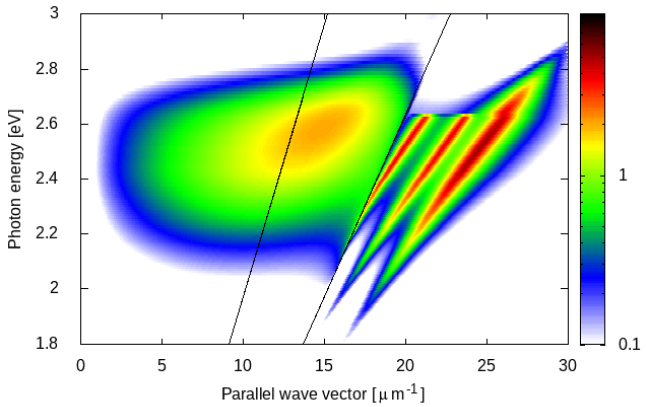

Figure A3.9. Power dissipation of emitting dipoles simulated for an 80 nm SpiroAc-TRZ OLED. The fraction of photons coupled into air equals 26.8%, while 52.8% is coupled into air+substrate modes. The remaining fraction is lost in waveguide and surface-plasmon-polariton modes.

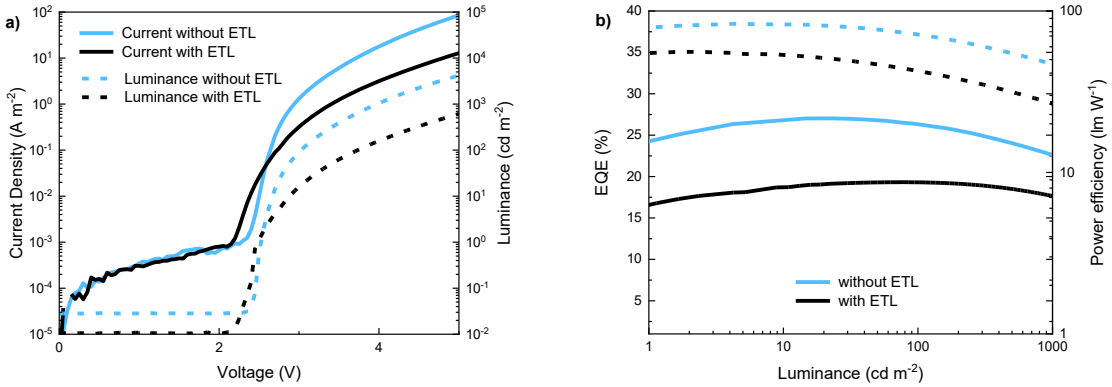

Figure A3.10. a) *J-V-L* characteristics of SpiroAc-TRZ:mCPCN OLEDs with and without a 20 nm 2,4,6-tris[3-(diphenylphosphinyl)phenyl]-1,3,5-triazine (PO-T2T) hole- and exciton-blocking layer between the emissive layer and the cathode, and the corresponding EQE and power efficiency (b). The fact that the EQE does not improve with an added blocking layer shows that the single-layer OLED (without HBL) does not suffer from nonradiatiave losses due to charges or excitons near the metallic cathode. Conversely, the blocking layer distorts the charge balance, which actually reduces the EQE due to more recombination near the EML/HBL interface. The lower current density in the presence of an HBL is also a result of the disrupted charge balance.

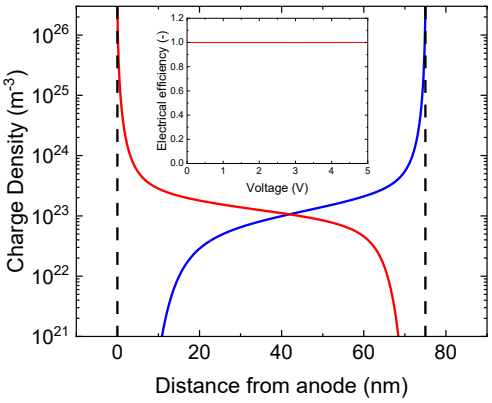

Figure A3.11. Charge density across the emitting layer of a SpiroAc-TRZ:mCPCN single-layer OLED as simulated by the drift-diffusion model using the experimental charge-transport parameters. The hole (electron) density is high near the ohmic anode (cathode). Therefore, electrons and holes cannot traverse the layer without recombining, considering that the bimolecular recombination rate is determined by the product of the electron and hole density. As a result, the electrical efficiency, defined by the recombination events per injected charge carrier, equals unity over the complete voltage range (inset).

Table A3.1. (Summarized drift-diffusion modeling parameters for electron- and hole-only devices)

	electrons	*holes*
Trap density, N_t gauss (m^{-3})	2.0×10^{22}	-
Trap depth, E_t (eV)	0.850	-
Width of Gaussian trap distribution, σ_t (eV)	0.100	-
Lattice constant EGDM, a (m)	1.3×10^{-9}	1.4×10^{-9}
DOS variance EGDM, σ (eV)	0.15	0.15
Mobility at 295 K, μ (m^2/Vs)	5.6×10^{-13}	5.6×10^{-13}

Table A3.2. (Summarized OLED characteristics)

		EQE (%) / PE (lm W^{-1}) / CE (cd A^{-1})			
EL maximum (nm)	V_{on} (V)	Maximum	at 100 cd m^{-2}	at 1000 cd m^{-2}	CIE (x,y)
490	2.53	27.7 / 84 / 72	26.9 / 73 / 70	23.0 / 49 / 60	0.20, 0.48

Table A3.3. (Summarized photoluminescence quantum yields)

	SpiroAc-TRZ	SpiroAc-TRZ:mCPCN
PLQY (%)	84	97

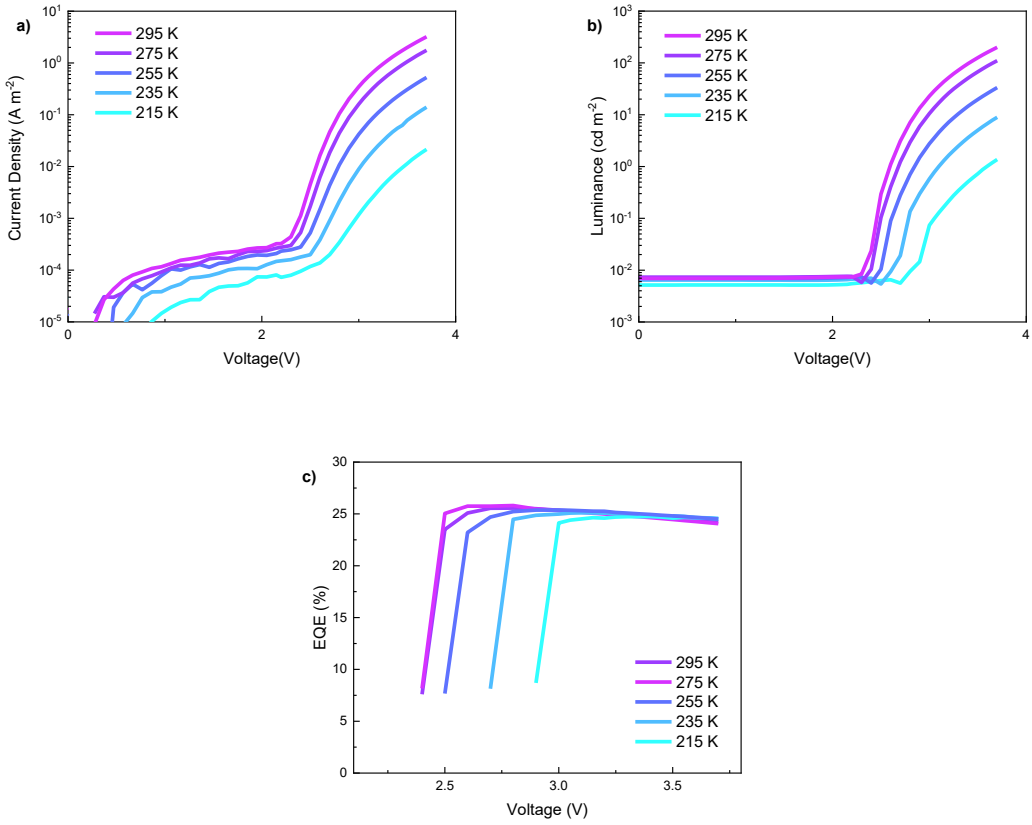

Figure A3.12. a) Temperature dependent *J-V* characteristics of a SpiroAc-TRZ:mCPCN OLED with the single-layer device structure PEDOT:PSS:PFI/SpiroAc-TRZ:mCPCN (1:1; 100 nm)/Ba/Al showing a shift in the switch-on voltage. b) The corresponding temperature dependent *L-V* characteristics exhibiting a reduction in generated light. (c), The temperature dependent *EQE-V* characteristics reveal no further increase of the EQE upon cooling down the sample, thus exciton-polaron quenching as a non-radiative loss process can be ruled out.

Appendix Chapter 4

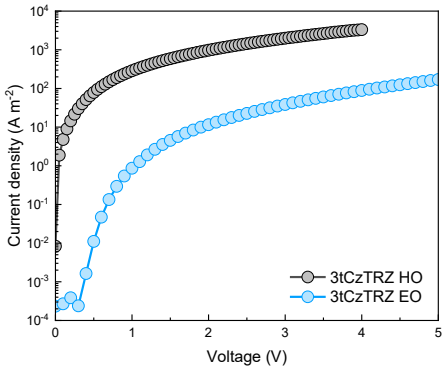

Figure A4.1 | Current density (*J*)- Voltage (*V*) characteristics of a hole-only and electron-only device of neat 3tCzTRZ (130 nm thickness).

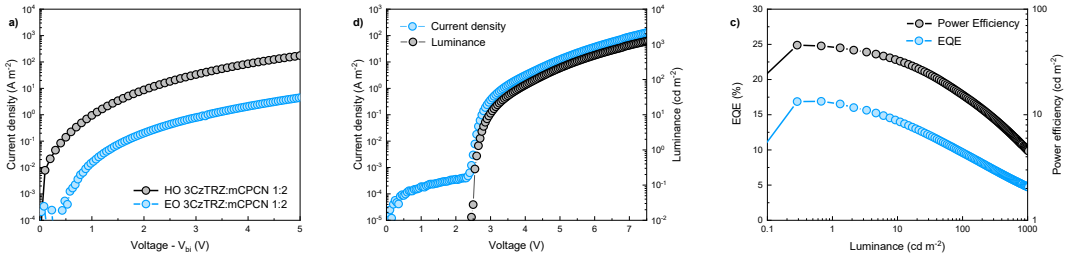

Figure A4.2 a) Current density (*J*)- Voltage (*V*) characteristics of an electron (V_{bi} = 0.52 V) and hole-only device of 3CzTRZ:mCPCN (1:2) with a layer thickness of 101 nm, b) corresponding *J-V-L* OLED characteristics and c) corresponding EQE and power efficiency.

Table A4.1. Summarized drift-diffusion modeling parameters for hole-onlys electron-onlys and OLEDs.

	neat 3CzTRZ		*3CzTRZ:mCPCN 1:1*	
	electrons	*holes*	*electrons*	*holes*
Trap density, N_t gauss (m^{-3})	1.4×10^{22}	8×10^{22}	1.4×10^{22}	8×10^{22}
Trap depth, E_t (eV)	0.650	0.540	0.650	0.540
Width of Gaussian trap distribution, σ_t (eV)	0.100	0.100	0.100	0.100
Lattice constant EGDM, a (m)	1.5×10^{-9}	1.6×10^{-9}	1.9×10^{-9}	1.6×10^{-9}
DOS variance EGDM, σ (eV)	0.110	0.115	0.110	0.115
Mobility at 295 K, μ (m^2/Vs)	5.0×10^{-10}	5.0×10^{-10}	2.2×10^{-11}	2.2×10^{-11}
k_{TPQ} ($m^3\ s^{-1}$)	-		0.7×10^{-19}	
k_{TTA} ($m^3\ s^{-1}$)	6.0×10^{-19}		6.0×10^{-20}	
τ_t (s)	1.5×10^{-5}		3.0×10^{-3}	
τ_S (s)	8.0×10^{-8}		1.5×10^{-7}	

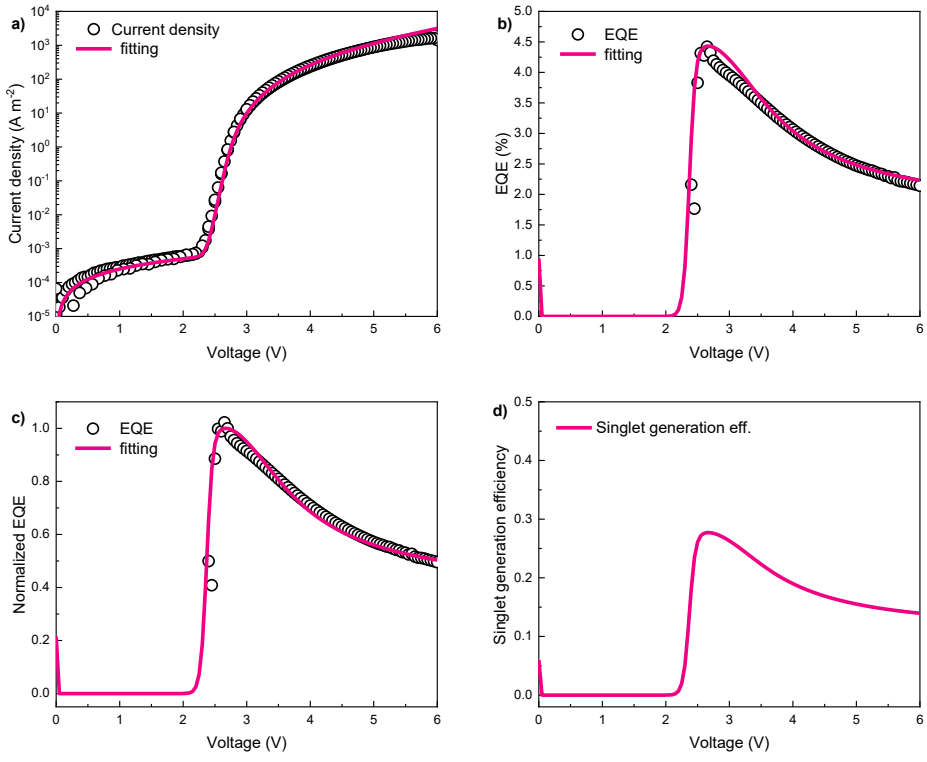

Figure A4.3 | Simulated device characteristics for the neat 3CzTRZ OLED with 82 nm thickness. a) Current density and fitting. b) experimental EQE vs voltage and fitting. c) normalized EQE vs voltage and fitting. d) simulated singlet generation efficiency.

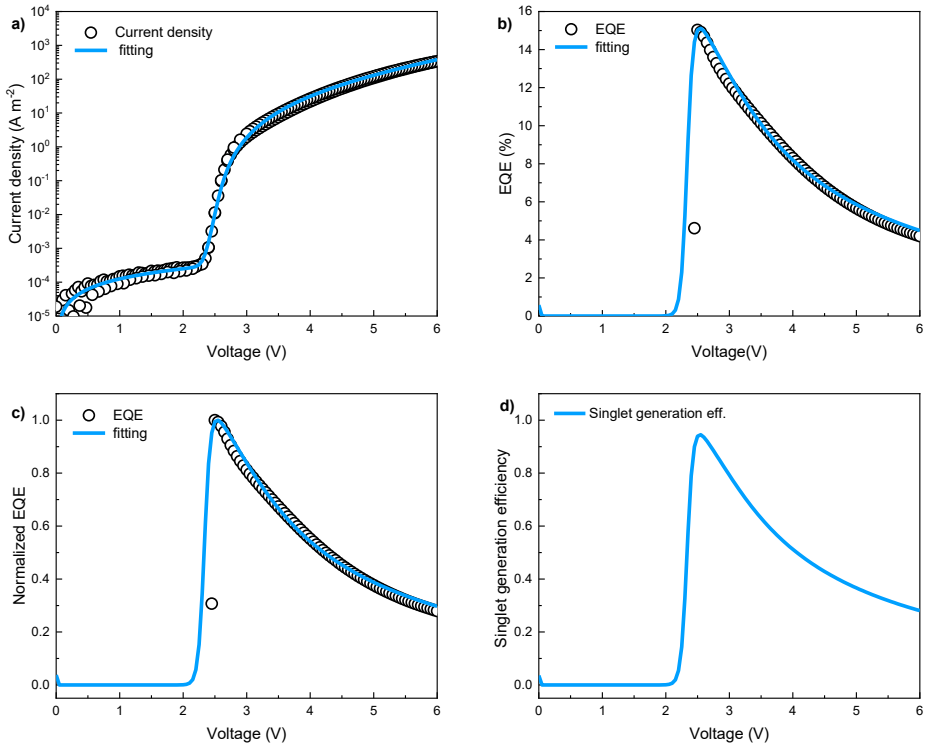

Figure A4.4. Simulated device characteristics for the neat 3CzTRZ:mCPCN (1:1) OLED with 72 nm thickness. a) Current density and fitting. b) experimental EQE vs voltage and fitting. c) normalized EQE vs voltage and fitting. d) simulated singlet generation efficiency.

Appendix Chapter 5

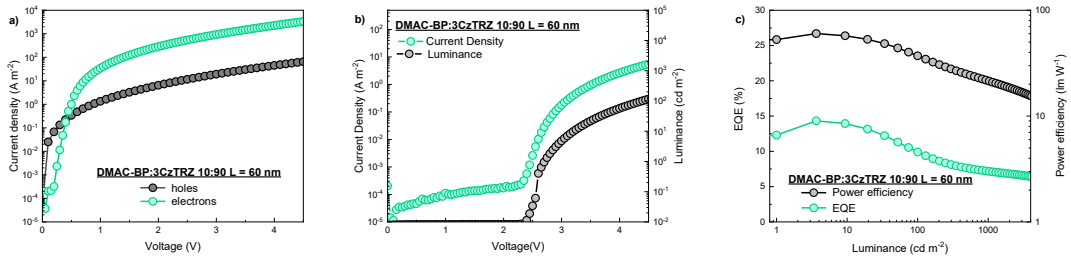

Figure A5.1. (a) Current-density vs. voltage (*J-V*) characteristics for electrons (green symbols) and holes (black symbols) for a film consisting of a DMAC-BP:3CzTRZ 10:90 blend of 60 nm thickness. (b) *J-V* characteristics for a single-layer DMAC-BP:3CzTRZ 10:90 OLED c) External quantum efficiency (EQE) (green symbols) and power efficiency (black symbols) for a single-layer DMAC-BP:3CzTRZ 10:90 OLED.

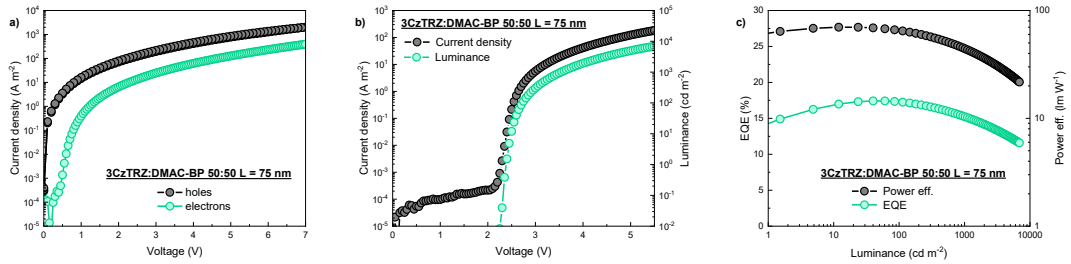

Figure A5.2. (a) Current-density vs. voltage (*J-V*) characteristics for electrons (green symbols) and holes (black symbols) for a film consisting of a DMAC-BP:3CzTRZ 50:50 blend of 75 nm thickness. (b) *J-V* characteristics for a single-layer DMAC-BP:3CzTRZ 50:50 OLED c) External quantum efficiency (EQE) (green symbols) and power efficiency (black symbols) for a single-layer DMAC-BP:3CzTRZ 50:50 OLED.

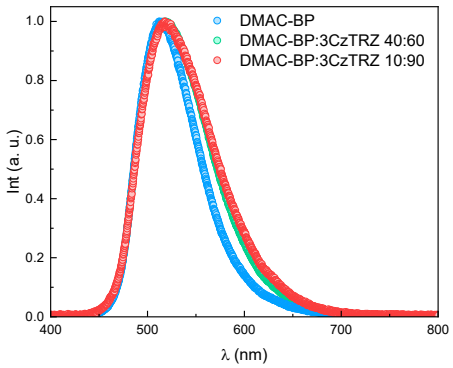

Figure A5.3. Electroluminescence spectra obtained for different dilutions of DMAC-BP in 3CzTRZ (100%, 40%, 10%) in a single-layer OLED.

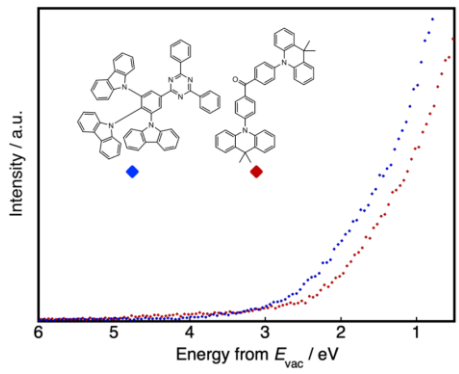

Figure A5.4. IPES spectra for 3CzTRZ and DMAC-BP.

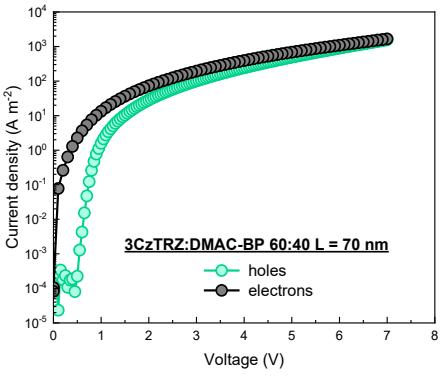

Figure A5.5. *J-V* characteristics for electrons (green symbols) and holes (black symbols) for a film consisting of a 40:60 DMAC-BP:3CzTRZ blend of 70 nm thickness without built-in voltage correction.

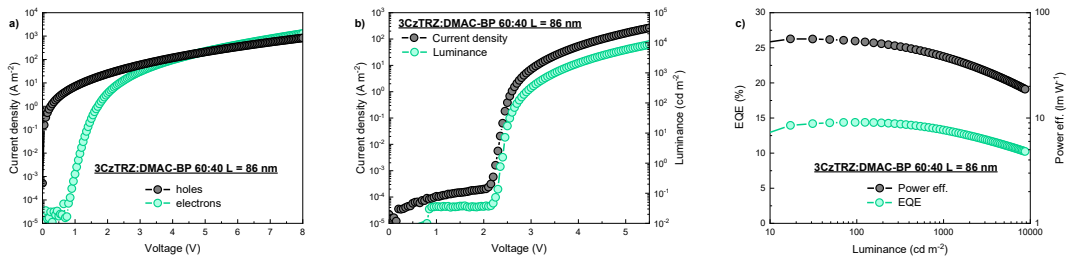

Figure A5.6. (a) Current-density vs. voltage (*J-V*) characteristics for electrons (green symbols) and holes (black symbols) for a film consisting of a DMAC-BP:3CzTRZ 40:60 blend of 86 nm thickness. (b) *J-V* characteristics for a single-layer DMAC-BP:3CzTRZ 40:60 OLED c) External quantum efficiency (EQE) (green symbols) and power efficiency (black symbols) for a single-layer DMAC-BP:3CzTRZ 40:60 OLED.

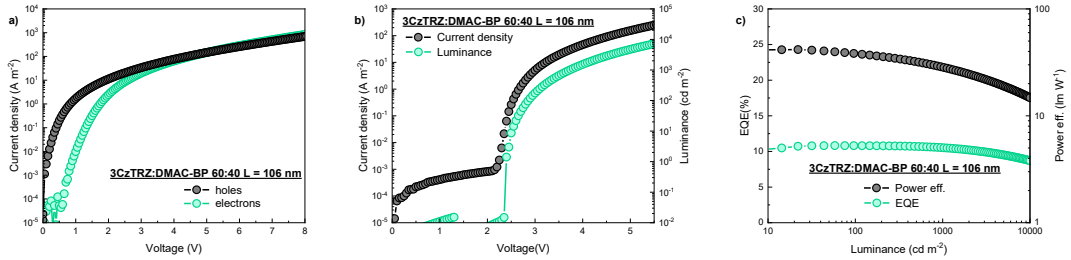

Figure A5.7. (a) Current-density vs. voltage (*J-V*) characteristics for electrons (green symbols) and holes (black symbols) for a film consisting of a DMAC-BP:3CzTRZ 40:60 blend of 106 nm thickness. (b) *J-V* characteristics for a single-layer DMAC-BP:3CzTRZ 40:60 OLED c) External quantum efficiency (EQE) (green symbols) and power efficiency (black symbols) for a single-layer DMAC-BP:3CzTRZ 40:60 OLED.

List of Publications

Included in this thesis

[1] O. Sachnik, X. Zhou, J. Nikan, B. van der Zee, Y. Li, P. W. M. Blom, G. J. A. H. Wetzelaer, *Adv. Opt. Mater.* **2024**, *12*, 2302000.

[2] O. Sachnik, Y. Ie, N. Ando, X. Tan, P. W. M. Blom, G. J. A. H. Wetzelaer, *Adv. Mater.* **2024**, *36*, 2311892.

[3] O. Sachnik, Y. Li, X. Tan, J. J. Michels, P. W. M. Blom, G. A. H. Wetzelaer, *Adv. Mater.* **2023**, 2300574.

[4] O. Sachnik, X. Tan, D. Dou, C. Haese, N. Kinaret, K.-H. Lin, D. Andrienko, M. Baumgarten, R. Graf, G.-J. A. H. Wetzelaer, J. J. Michels, P. W. M. Blom, *Nat. Mater.* **2023**.

Not included in this thesis:

[5] K. Thakur, B. van der Zee, O. Sachnik, C. Haese, R. Graf, J. J. Michiels, C. R. Gert-Jan A.H. Wetzelaer, P. W. M. Blom, *Adv. Photonics Res.* **2024**, *2400022*, 1.

[6] Y. Li, O. Sachnik, B. van der Zee, K. Thakur, C. Ramanan, G. J. A. H. Wetzelaer, P. W. M. Blom, *Adv. Opt. Mater.* **2021**, *9*.

[7] A. Pipertzis, G. Papamokos, O. Sachnik, S. Allard, U. Scherf, G. Floudas, *Macromolecules* **2021**, *54*, 4257.

[8] F. Trilling, O. Sachnik, U. Scherf, *Polym. Chem.* **2019**, *10*, 627.

Acknowledgements

In the following section, I want to show my gratitude, because a lot of the work presented in this thesis would not be possible without the help and input of others. First of all, I would like to thank my promoter Prof. Paul Blom for giving me the opportunity to start my doctoral research in his group. I am very grateful for the discussions, advises, explanations and all the supervision I received in the past four years. Working in your group not only gave me the chance to work with a lot of fancy equipment and facilities, but gave me the chance to truly explore science. This was only possible due to the encouraging environment and all the talented people in your group. Here, I want to give *special thanks* to my group leader Jasper Michels. You were always approachable and giving me the right advices and feedback, especially when something in the lab went wrong. I am amazed by your kindness, understanding and all your knowledge in chemistry – and beyond. I do also want to give a large *thank you* to Gert-Jan Wetzelaer for working with you together. You were always approachable and kind and it was great to discuss on-going experiments and results. Your knowledge is astounding and getting a glimpse already taught me a lot.

For being part of my final defense committee, I want to show my appreciation to Prof. Pol Besenius, Prof. Katja Heinze and Prof. Christoph Kerzig.

As mentioned, a lot of the work presented wouldn't have been possible without the input from great colleagues, therefore I want to show my gratitude to everyone in the OLED team. I want to convey my gratitude to Kai for showing me the AK-Blom-basics, which helped me a lot in the beginning. Thank you Ricardo and Anie for your caring welcoming in the office. To Xin, Naz, Dehai, Bas, Kalyani, Xiao, Jawid, Naomi, David T., Timon and Constantin: Thank you all so much for all the discussions and important contributions, it was a great experience to collaborate with all of you. I want to give credit to you both, Mahni and Marvin, it was a pleasure to supervise you during your theses and see everything that you achieved. To all the past and present AK Blom members, thank you so much for creating such a nice atmosphere in our group: David M., Franziska W., Sten, Katha, Okan, Aristea, Carla, Renan, Shuanglong, Zhitian, Morteza, Franziska H., Chongyao, Parham, Judith, Yungui, Imke and Felix. Without our skilled technicans, not a single molecule would move on its supposed position: To Frank Keller, Sirma Koynova, Michelle Beuchel, Christian Bauer and Verona Maus a big *thank you* for keeping intact all the labs and facilities and for all the talks in between. Thank you Petra for being the good soul of our group and helping with everything that is important.

I want to thank my former colleagues from Ullrich Scherf's lab at the University of Wuppertal, which shared valuable knowledge and taught me everything I know: Florian, Markus, Christin, Dario, Patrick, Tina and Jannis, I keep you in good memories and am grateful for the great atmosphere you provided

during my Bachelor and Master thesis. Thank you Prof. Scherf for giving me the opportunity to be part of your group and the possibility to perform research on conductive polymers. Thank you Nils, Nicole, Moritz, Julia, Chris and Laura for sharing the time during our studies. I still remember our early months and the struggle we all felt in the beginning and how we managed to help each other throughout our studies.

Last of all, my largest gratitude goes to my family, parents and to you Julia for supporting me throughout my studies and doctoral research. Thank you for all your advices and help in the past years. Julia, thank you for being a part of my life. Without your constant encouragement, support and caring, I would not have been able to complete this lengthy road.